COMPRESSIBLE SHEAR FLOW TRANSITION AND TURBULENCE: ENHANCEMENT OF GKM NUMERICAL SCHEME AND SIMULATION/ANALYSIS OF PRESSURE EFFECTS ON FLOW STABILIZATION

A Dissertation

by

GAURAV KUMAR

Submitted to the Office of Graduate Studies of
Texas A&M University
in partial fulfillment of the requirements for the degree of

DOCTOR OF PHILOSOPHY

Approved by:

Chair of Committee,	Sharath S. Girimaji
Committee Members,	Rodney Bowersox
	Hamn-Ching Chen
	Andrew Duggleby
Head of Department,	Rodney Bowersox

December 2012

Major Subject: Aerospace Engineering

ABSTRACT

Despite significant advancements in the understanding of fluid flows, combustion and material technologies, hypersonic flight still presents numerous technological challenges. In hypersonic vehicles turbulence is critical in controlling heat generation in the boundary layer, mixing inside the combustor, generation of acoustic noise, and mass flow in the intake. The study of turbulence in highly compressible flows is challenging compared to incompressible due to a drastic change in the behavior of pressure and a relaxation of the incompressibility constraint. In addition fluid flow inside a flight vehicle is complicated by wall-effects, heat generation and complex boundary conditions. Homogeneous shear flow contains most of the relevant physics of boundary and mixing layers without the aforementioned complicating effects. In this work we aim to understand and characterize the role of pressure, velocity-pressure interaction, velocity-thermodynamics interaction in the late-stage transition-to-turbulence regime in a high speed shear dominated flow by studying the evolution of perturbations in in a high Mach number homogeneous shear flow. We use a modal-analysis based approach towards understanding the statistical behavior of turbulence. Individual Fourier waves constituting the initial flow field are studied in isolation and in combination to understand collective statistical behavior. We demonstrate proof of concept of novel acoustic based strategies for controlling the onset of turbulence. Towards this goal we perform direct numerical simulations (DNS) in three studies: (a) development and evaluation of gas kinetic based numerical tool for DNS of compressible turbulence, and perform detailed evaluation of the efficacy of different interpolation schemes in capturing solenoidal and dilatational quantities, (b) modal investigation in the behavior of pressure and isolation of linear, non-linear, inertial and pressure actions, and (c) modal investigation in the possible acoustic based control strategies in homogeneously sheared compressible flows.

The findings help to understand the manifestation of the effects of compressibility on transition and turbulence via the velocity-pressure interactions and the action of individual waves. The present study helps towards the design of control mechanisms for compressible turbulence and the development of physically consistent pressure strain correlation models.

DEDICATION

To my father,

ACKNOWLEDGMENTS

I would like to thank my advisor, Dr. Sharath S. Girimaji, for his guidance, support and patience. He has been a role model, teacher and supervisor. He has inspired and guided me throughout my stay as a graduate student at Texas A&M University. I would also like thank my committee members, Dr. Rodney Bowersox, Dr. Hamn-Ching Chen, and Dr. Andrew Duggleby. Their comments, advice and support have been essential for this dissertation.

I would like to thank my colleagues, Dr. Sawan Suman, Dr. J. Kerimo, Dr. K. Lee, Ashraf Ibrahim, Jacob Cooper, Dasia Reyes, Zhimin Xie, Carlos Gomez, Rebecca Bertsch, Mona Karimi, Sunny Jain, Daniel Araya, Frans Eberson and others who have been part of the 'turbulence research group'. They made my journey intellectually enriching and helped broaden my understanding of Aerospace engineering through their work, discussions and critique. A special thanks to my office-mates, Zhimin and Carlos, who were ever so helpful and accomodating. I would like to thank Dr. Diego Donzis for the time he took out of his busy schedule for answering my questions in numerical aspects of fluid flows. The experience as a graduate student at Aerospace engineering was made even more enjoyable due to much help from staff and faculty, including Ms. Karen Knabe, Ms. Colleen Leatherman and graduate advisor Dr. Rodney Bowersox.

My stay at College Station was made ever so enjoyable beacuse of my friends Roshmik, Nikhil, Abhinav, Rajesh, Sourav, Amit, Shahina and Sreeni. Their presence transformed and shaped my graduate life and made it full of enthusiasm and fun. And to my friends, Sandip and Vinita, thank you for making this journey 'memorable'. And, at last but I guess the most important, I take this opportunity to thank my family, who always supported me with their love, patience and guidance throughout my academic journey.

TABLE OF CONTENTS

Page

Page

LIST OF TABLES

LIST OF FIGURES

FIGURE Page

FIGURE Page

FIGURE Page

FIGURE Page

FIGURE Page

FIGURE Page

FIGURE Page

1. INTRODUCTION AND MOTIVATION

In the quest for designing hypersonic flight vehicles, understanding the behavior of compressible turbulence and flow-control mechanisms plays a prominent role. In hypersonic vehicles, turbulence is critical in controlling heat generation in the boundary layer, mixing inside the combustor, generation of acoustic noise, and mass flow in the engine intake. The nature of compressible turbulence is drastically different from incompressible primarily due to the change in behavior of pressure. Investigating the effect of compressibility is important in designing physically consistent pressure-strain correlation models and control mechanisms for delaying the onset of turbulence or for enhancement of mixing.

In recent years, direct numerical simulation (DNS) has become an important tool in studying turbulence. A tremendous increase in computational power over the last few decades has facilitated a widespread use of DNS. Direct numerical simulation of compressible turbulence presents many challenges in the development of computational methods. The numerical difficulties are compounded due to high cascade rates which give rise to large spatio-temporal gradients, presence of shocklets and variable transport coefficients. Numerical methods and interpolation schemes used in simulations of compressible turbulence must have high order of accuracy in smooth flow regions. On the other hand, numerical schemes must be robust enough to capture discontinuities arising due to shocklets without leading to spurious numerical oscillations. The challenges in the flow-physics are also very vital.

Computations of turbulence are based mostly on the Navier-Stokes equations. Most of the theoretical understanding of turbulence is primarily in terms of the continuum flow framework. In recent years, there has been a renewed interest in hypersonic flows, re-entry problems, rarefied flow, astrophysical gas dynamics and flows in micro-scale devices. The applicability of Navier-Stokes is restricted in these areas due to breakdown of the continuity assumption. Also, the standard constitutive

relations for the stress tensor fails in these flow regimes. These problems can be averted with a kinetic-theory based flow description.

With the above in mind, kinetic-theory based Boltzmann Bhatnagar-Gross-Krook (B-BGK) approach [1] is gaining popularity in a variety of simulations [2,3] spanning incompressible to highly compressible regimes. The kinetic Boltzmann equation is an evolution equation for the velocity distribution function of a single particle. With kinetic theory as the underlying physics, Boltzmann equation is valid over a large range of transport phenomenon compared to the continuum based Navier-Stokes equations. The Boltzmann equation, in its most general form, is a Fokker-Planck equation [4] which is an integro-differential equation. The numerical amenability of the equations are restricted due to the complicated collision operator. Apart from highly simplified problems, computing the Boltzmann equation is tremendously expensive. The simplified linear collision operator proposed by Bhatnagar-Gross-Krook (BGK) changes the Boltzmann equation making it amenable for computations. In the last decade GKM has been applied in a variety of fluid flow simulations. Liao *et al.* [5] applied GKM for decaying isotropic turbulence of moderately compressible flows. To date, DNS of high turbulent Mach numbers ($1.0 - 2.0$) using GKM has not been studied. Applying GKM in a high turbulent Mach number flow ($M_t > 1.0$) poses greater difficulties due to stronger random shocklets, higher spatio-temporal gradients and variable transport coefficients. Flow and thermodynamic variable interpolation is a critical part of the compressible gas kinetic methods. Variables at cell-centers need to be interpolated to cell interfaces for calculation of fluxes. The accuracy in the interpolation controls the accuracy in flux calculations. Reconstruction schemes should have high order of accuracy in smooth flow regions. It should also capture regions of very steep gradients like shocks/shocklets without adding too much numerical dissipation. We use shock-capturing instead of shock-resolving schemes because an extremely fine grid is needed for resolving shock like steep gradients. In this work we enhance GKM with high-order interpolation schemes for DNS

of highly compressible turbulent flows – decaying compressible turbulence and high speed homogeneous shear.

The complexity of turbulence increases as we transition from incompressible to compressible flows. The extent of compressibility effects in shear flows can be characterized in terms of a non-dimensional gradient Mach number $M_g = \frac{Sl}{\sqrt{\gamma RT}}$ where S is the mean shear and l is lengthscale related to largest inertial lengthscale in the flow. Relaxation of the incompressibility constraint, $\nabla \cdot \mathbf{u} = 0$, adds additional degrees of freedom to compressible flows in terms of permissible Fourier modes constituting the flow. Also, compressibility introduces new flow-physics through additional terms (like pressure-dilatation in kinetic energy evolution equation) which arise due to a non-zero divergence field. It would be reasonable to expect additional families of non-solenoidal (dilatational) Fourier modes influencing compressible shear flows. The behavior of pressure in compressible homogeneous shear flows is far more complicated than the incompressible counterpart. The increased complexity in compressible shear flows poses additional challenges for physically consistent turbulence modeling.

In transition-to-turbulence studies, investigation of individual modes in order to understand the collective behavior is a widely used methodology. In fully grown turbulence a similar methodology is not feasible because of the inherent non-linearity, which makes identification and isolation of the contribution of individual modes difficult. However, in the linear limit of Navier-Stokes which is governed by the rapid distortion theory (RDT) and is the driving limit of many flows, we can isolate and examine the behavior of individual modes. Such studies are also valuable at the late stages in the transition regime. RDT has proven to be an excellent tool for such studies in the linear limit. But, the inferences from RDT are restricted to flows with very high non-dimensional strain rates $SK/\epsilon \gg 1$. Since, late stage transition involves moderate to high values of SK/ϵ, direct numerical simulations (DNS) are deemed an appropriate tool for studying the behavior individual modes. It would

be very insightful to analyze DNS for highly compressible homogeneous shear flows in-order to understand the roles and contributions of individual Fourier modes and their contribution to collective behavior.

The nature and role of pressure changes from incompressible to compressible shear flows. Depending on the gradient Mach number, shear flows vary between two extreme limits: (i) incompressible limit ($M_g \approx 0$), where pressure maintains the incompressibility condition ($\nabla \cdot \mathbf{u} = 0$) and is governed by the Possion equation, (ii) Burgers limit ($M_g \to \infty$), where pressure plays no significant role. In between these limits, at high enough M_g, there is a complex interplay between pressure and inertia which involves interesting physical features displayed by individual modes. played by individual modes. The role played by pressure varies with increasing compressibility. In this regime pressure exhibits an acoustic nature and evolves according to the wave equation. This changing nature of pressure has a key impact on evolution of different Fourier modes in compressible shear flows. Also, with increasing compressibility, pressure and inertia effects start competing. In flows where the fluid time scale is small compared to acoustic time scale, inertia dominates. While pressure takes time to react to inertia incompressibility is violated, leading to a build-up of dilatation in the flow. When the acoustic time scale becomes comparable to the fluid time scale, role of pressure becomes significant. Since the pressure-strain correlation is a manifestation of compressibility effects on the Reynolds stresses, it is important to understand the complex coupling between pressure and velocity-field/inertia. A comprehensive understanding in the behavior of pressure would be vital in investigating the three-staged growth and in development of better pressure-strain correlation models.

Compressibility has an stabilizing effect on the normalized growth rate of turbulence. The stabilizing effect of compressibility has been observed in experiments of mixing layers, where rate of production was observed to be 'inhibited' [6–8]. Sarkar [9] performed series of DNS of homogeneous shear with varying initial M_g and M_t.

The growth rate of turbulent kinetic energy was observed to decrease significantly in the DNS series with increasing initial M_g. They find that the resulting '*stabilizing*' effect of compressibility is a function of gradient Mach number. Simone *et. al* [10] investigate stabilizing and destabilizing effect of compressibility and demonstrate the key role played by the 'distortion Mach number' ($M_d = Sl/a$) (which is similar to the gradient Mach number). For pure shear flows they show that for $St < 4$ growth rate of kinetic energy increases with increasing distortion Mach number; for $St > 4$ compressibility shows tendency to stabilize turbulence by decreasing the growth rate of normalized kinetic energy. The growth of kinetic energy is markedly more slow at late times. Simone *et. al* also identify two stages of evolution which is further supported through rapid distortion theory (RDT) simulations [11–13].

Any statistically homogeneous flow field can be viewed as a collection of Fourier modes. DNS of an initially isotropic field (a collection of Fourier modes) in homogeneous shear yields a statistical picture but masks the role played by individual modes. Over the last few decades, the direct statistical effect of pressure in terms of pressure-strain correlation, pressure dilatation and other indirect effects like growth rate of kinetic energy and dissipation for compressible shear flows has been studied but not fully understood. An important question is how pressure affects individual Fourier modes to bring about the observed statistical three-stage behavior. The study of the role of pressure would also be key in understanding how compressibility effects manifest via the action of individual modes.

The ultimate goal in understanding transition and turbulence in engineering flows is two fold: (i) design of better and physically consistent models and, (ii) formulation and design of control methods. A modal based understanding of flow physics can help in the formulation of new flow control strategies and provide a more physical basis for the development of pressure-strain correlation models. To date, most of the turbulence control methods, active or passive, are designed for incompressible flows. The compressible turbulence exhibits new flow physics (compared to incompressible)

that can be used in formulation of novel flow control strategies. A physics based understanding would help improve such strategies either in reducing the growth-rate of turbulence (for prolonged laminar boundary layers) or in enhancing turbulence (for mixing inside combustor).

1.1 Scope of Dissertation

In this dissertation we perform DNS to gain a better understanding on the effects of compressibility on transition and turbulence via the velocity-pressure interactions. We aim to provide a modal based insight into (a) characterization of the behavior of pressure and (b) formulation of acoustic-based control strategies in homogeneous shear flows. Keeping the above goals in perspective three studies are performed with the following aims:

Study 1: The objective of this study is to enhance GKM to enable direct simulation of high Mach number transition and turbulence. This would provide a suitable numerical tool for carrying out the physics-investigation. We perform the following investigations:

1. Examine advanced reconstruction schemes developed in the context of Navier-Stokes approaches for compatibility of use with GKM.

2. Propose a detailed validation protocol and complete studies to determine the optimal reconstruction scheme in terms of accuracy and robustness. The validation protocol includes:

   (a) Examine solenoidal (vortical) and dilatational (acoustic) portions of the velocity field individually and collectively.

   (b) Validate linear aspects of the GKM code by comparison with RDT in high Mach number homogeneous shear turbulence. This examination is critical for both transition and turbulence applications. We evaluate the model

performance by comparison with RDT and analytical 'pressure-released' Burgers solution as appropriate.

(c) Validate non-linear aspects of the GKM code by comparison against a 'gold-standard' super-resolved direct simulation. This evaluation is performed in decaying isotropic turbulence with the pertinent dimensionless parameter being the turbulent Mach number.

3. Evaluate the merits of temperature *vs.* internal energy as the preferred candidate for interpolation in the calculation of energy flux. While temperature and energy interpolation are equally permitted by governing physics, numerical considerations show that one is better suited than the other from the point of view of computational robustness.

Study 2: The objective of this study is to perform DNS and linear analysis of individual and collective behavior of various perturbation/fluctuation modes in homogeneous shear turbulence. Specifically, we seek the following:

1. Characterize the modal behavior of pressure.

2. Study the effect of pressure on evolution of kinetic energy of different individual modes.

3. Determine the effect of Mach number and wave-orientation.

4. Provide a more complete explanation of the collective compressibility effect on transition/turbulence behavior and explain the modal mechanism underlying the three-staged growth of kinetic energy.

Study 3: The objective of this study is to demonstrate acoustic based novel flow control strategies in highly compressible shear flows and provide a modal-analysis based insight in the flow physics. Towards this end we perform direct numerical simulations with the following aims:

1. Study the effect of change in Prandtl number on the growth of kinetic energy especially in acoustic dominated second-stage.

2. Examine the effect of change in Prandtl number on growth of straight and oblique modes. We also aim to investigate the behavior of equipartition function for different modes/modes.

3. Provide a modal-understanding based explanation of control strategy to bringing about a delay in the on-set of turbulence.

1.2 Dissertation Overview

Chapter II describes the gas kinetic equations and advantages of kinetic based methods over Navier Stokes approach. Chapter III details the enhancement of the GKM based numerical tool for highly compressible decaying turbulence and homogeneous shear flows. Studies aimed for characterizing the behavior of pressure, isolation of linear and non-linear effects and modal explanation of three-staged growth of kinetic energy in homogeneous shear flow is presented in Chapter IV. In Chapter V we discuss modal and collective studies of acoustic based possible flow-control strategies which use the equipartition of dilatational kinetic energy and potential energy of turbulence in homogeneous shear flows. We present the conclusions in Chapter VI.

2. COMPUTATIONAL METHOD

2.1 The Gas Kinetic Method

In this work we use gas kinetic method (GKM) for solving the conservation equations of mass, momentum and energy. Over the last two decades GKM has gained popularity in computational fluids community due to its simplicity and yet richer physics. In this section we discuss the advantages of using GKM and present brief formulation of the multidimensional gas kinetic method. Details involved in solving the equations arising in GKM are provided in many places in the literature, see for example [2,14–16]. The GKM is a finite volume-based method developed to solve the Boltzmann equations for compressible flows with the collision operator based on the Bhatnagar-Gross-Krook (BGK) relaxation model. Due to its roots in kinetic theory, GKM is expected to retain more non-continuum flow physics than the Navier-Stoke equations. Consequently, GKM can be more readily extended to near non-continuum regime to match with Direct Simulation Monte Carlo method [17].

2.1.1 Background

The GKM offers a computational scheme for exploiting the advantages of continuum and kinetic-Boltzmann descriptions of the flow physics. We will briefly review the various potential and proven advantages of GKM over NS methods of comparable computational efforts. The GKM uses the B-BGK equation which is the Boltzmann equation subject to the BGK simplification.

1. One of the fundamental advantages of GKM is that the fluxes of mass, momentum and energy can be calculated in a self-consistent manner from a single particle distribution function [18–20]. In continuum NS based methods, inconsistencies between the fluxes in mass conservation and momentum/energy balance equations can possibly arise.

2. For the construction of numerical schemes, it more appropriate to apply the discretization to the more fundamental quantity, the distribution function, rather than the derived continuum (primitive or conservative) variables [21]. Also in GKM, terms giving rise to the rate-of-strain tensor and heat flux vector are computed as natural parts of the probability distribution. Since the stencil used is same as convective fluxes, an additional viscous discretization is not required [21]. It is also shown in other studies that direct computation of stress from the distribution function rather than discretization yields important numerical advantages in the implementation of Large Eddy Simulations (LES) turbulence models [22]. In NS-LES subgrid stress is assumed to be in equilibrium with the instantaneous local strain, effect of eddy-viscosity is instantaneous and non-hydrodynamic variables are completely ignored. Whereas in kinetic theory based LES, an instant equilibrium with filtered strain is not assumed. Therefore, kinetic theory based LES formulation may lead to more spatio-temporal memory effects [22].

3. GKM considerably facilitates mesh-transparent (mesh-topology independent) formulations of numerical schemes because an additional viscous discretization is not required. This makes the gas-kinetic approach particularly attractive for general unstructured meshes. While in NS, viscous discretization depends on the mesh topology and the choice of control volume in finite-volume schemes (cell-centered vs. cell-vertex schemes) [21].

4. The advection physics manifests through a non-linear term in the Navier-Stokes equation. Gas-kinetic equation is a first-order integro-partial-differential equation with a linear advection term [14]. Non-linear physics resides in the collision operator which is local and hence more easily amenable to efficient computation [23].

5. In NS simulations of high-speed flows with shocks, the need for accuracy and robustness leads to conflicting demands on the numerical scheme. The problems arising in the Reimann solvers and upwinding has been discussed at length in [24,25]. Contemporary efforts aim to resolve this by combining the accuracy of Godunov-type schemes and the robustness of flux-vector splitting schemes. Gas-kinetic BGK scheme has accuracy superior to flux vector splitting schemes and also avoids the anomalies arising from Godunov type schemes [26, 27].

6. The H-theorem bridges between equilibrium thermodynamics and non-equilibrium statistical mechanics [28]. The Boltzmann and B-BGK equations satisfy the H-theorem and the GKM approach preserves this crucial property. In the continuum description of flow physics, H-Theorem can be interpreted as the statement of the second law of thermodynamics. The BGK collision term results in positive entropy production, which ensures that the solution obtained is physical [2, 19]. An example of an unphysical solution is the presence of expansion shocks. These are typically seen in continuum calculations of high Mach number flows which occur.

7. When the dissipation provided in the projection stage of gas evolution is not enough, Godunov-type methods suffer from the carbuncle phenomenon [18,19, 29–33]. The spurious solution generated can be removed through 'entropy-fixes' [33–35] in NS schemes. The BGK based GKM scheme satisfies the H-theorm and always leads to a positive entropy generation [14, 19, 28]. The inherent physics underlying positive entropy generation (residing in the collision term) prevents the carbuncle problem in GKM.

8. Odd-even decoupling [18,19,31] is a numerical artifact observed in incompressible flows and when derivatives are computed on a finite difference grid where pressure and velocities are calculated at grid nodes. In NS odd-even decou-

pling is alleviated using staggard grids while the problem is not encountered in GKM.

9. As the GKM is based on kinetic theory and the Boltzmann equation, it has the potential to include extended hydrodynamics beyond the validity of the Navier-Stokes equation [5, 14, 36]. It is possible to include second and third order taylor expansion of the equilibrium and current distribution functions due to the simple transport and collision mechanism on the microscopic level [36–41]. Xu *et. al* [39] have developed a high-order gas-kinetic flow solver recently which incorporates the Burnett effects.

10. One of the important requirements in numerical solutions of the Euler equations is that the density and internal energy remain positive under Courant-Friedrichs-Lewys (CFL)-like condition–the so-called 'positivity-preserving' property. It is well-known that the classical approximate Riemann solvers do not satisfy this criterion [42–44]. On the other hand, GKM which are based on Boltzmann equations are found to preserve the positivity of density and internal energy [3, 45, 46]. The positivity in the gas kinetic schemes is closely related to the non-linear coupling in the flow variables in the construction of positive gas distribution functions. This coupling is difficult to satisfy in the continuum schemes where the flow equations are updated separately, such as the Lax-Friedrichs's method.

11. Due to the added capabilities, GKM has also been used for non-continuum [36, 47] and micro-flows [40]. Some special algorithms for the computation of rarefied transition to continuum flows have also been presented in the literature.

12. Although GKM is primarily intended for compressible flows, it can be used for computing nearly incompressible isothermal flows with greater ease than in continuum Navier-Stokes solvers [48]. Extension of NS based compressible

solvers in the incompressible regime is problematic due to large disparity between convective and acoustic wave speeds. Also, NS solvers need to handle intermediate boundary conditions [48,49] and solution of poission equation [48].

2.1.2 Governing equations and formulation of GKM

The kinetic Boltzmann equation describes the evolution of a single particle distribution function. The Boltzmann equation, in its most general form, is a Fokker-Planck equation [4] which is an integro-differential equation. The computational feasibility of the equation is restricted due to the complicated collision operator. Apart from some very simple flows, computations with the Boltzmann equation is extremely expensive. A simplified linear collision operator proposed by Bhatnagar, Gross and Krook [1] makes Boltzmann equation amenable for computations but restricts applicability to near-continuum flows. The equation governing the GKM is a partial differential equation with a linear advection term and first order in the derivatives.

The distribution function f is defined such that its integral in phase-space yields mass density (ρ):

$$mn_i = f(x_i, t, u_i, \xi_i), \quad \rho = \sum_i mn_i = \iiint f du dv dw d\xi. \tag{2.1}$$

Here m is the molecular mass, n_i is the number density of molecules at a given velocity, $\mathbf{u} = (u, v, w)$ is the particle velocity in Cartesian coordinates $\mathbf{x} = (x, y, z)$ and ξ_i are the internal degrees of freedom, such as rotation and vibration. The GKM equation [50, 51] is given as

$$f_t + u_i f_{x_i} = (g - f)/\tau \tag{2.2}$$

where f and u_i have already been introduced above, t is time; g is the equilibrium state approached by f and τ is collision time. The equilibrium state is assumed to have a Maxwellian distribution which in three-dimensions is given by

$$g = \rho \left(\frac{\lambda}{\pi}\right)^{(N+3)/2} \exp\left(-\lambda\left((u-U)^2 + (v-V)^2 + (w-W)^2 + \xi^2\right)\right) \tag{2.3}$$

were ρ is the above mentioned mass density, $\mathbf{U} = (U, V, W)$ is the macroscopic velocity vector, $\lambda \equiv m/(2kT) = 1/(2RT)$ with m being the molecular mass, k is the Boltzmann constant, R is the universal gas constant and T is temperature. The number of internal degrees of freedom of a particle represented by $\xi_i = (\xi_1, \xi_2, \ldots, \xi_N)$ is given by $N = (5-3\gamma)/(\gamma-1)$, where $\gamma = \frac{C_p}{C_v}$ is the ratio of specific heats. In equilibrium state, the internal variable ξ^2 is equal to $\xi^2 = \xi_1^2 + \xi_2^2 + \ldots + \xi_N^2$. The macroscopic quantities are related to the distribution function f through the first and second moments:

$$\mathbf{Q} \equiv \begin{pmatrix} \rho \\ \rho U \\ \rho V \\ \rho W \\ E \end{pmatrix} = \int \psi_\alpha f d\Xi, \quad \alpha = 1, 2, \ldots, 5, \tag{2.4}$$

where ψ_α is the vector of moments

$$\psi = (\psi_1, \psi_2, \psi_3, \psi_4, \psi_5)^T = \left(1, u, v, w, \frac{1}{2}\left(u^2 + v^2 + w^2 + \xi^2\right)\right)^T \tag{2.5}$$

and $d\Xi = dudvdwd\xi_1 d\xi_2 \ldots d\xi_N$ is an elemental volume in an expanded non-equilibrium phase space. For a fluid in thermodynamic and chemical equilibrium, the energy density is given by $E \equiv \rho\epsilon = \frac{1}{2}\rho\left(U^2 + V^2 + W^2 + \frac{N+3}{2\lambda}\right)$.

Since collision between particles is assumed to be perfectly elastic, it follows that mass, momentum and energy are conserved. Thus f and g satisfy the conservation constraint

$$\int (g - f)\psi_\alpha d\Xi = 0, \quad \alpha = 1, 2, \ldots, 5. \tag{2.6}$$

We see that eq. (2.2) together with the equilibrium state g and eqs. (2.4) and (2.6) form a non-linear integro-differential equation for the distribution function f.

As GKM uses the finite volume method, we need an expression for the fluxes. The fluxes are calculated from the distribution function as

$$\mathbf{F}_i = (\mathbf{F}, \mathbf{G}, \mathbf{H}) = \int u_i \, \psi f d\,\Xi\,. \tag{2.7}$$

In GKM, the fluxes are evaluated at cell interfaces. As a first step in the construction of GKM, we write a formal solution to the GKM equation (2.2) along a particle trajectory. The general solution at a cell interface $\mathbf{x}_{i+1/2,j,k}$ (were $\mathbf{x}_{i,j,k} = (x_i, y_j, z_k)$) and at time t is obtained by performing integration along a particle trajectory $\mathbf{x}' = \mathbf{x}_{i+1/2,j,k} - (t - t')\mathbf{u}$:

$$f(\mathbf{x}_{i+1/2,j,k}, t, \mathbf{u}, \xi) = \frac{1}{\tau}\int_{t_0}^{t} g(\mathbf{x}', t', \mathbf{u}, \xi) e^{-(t-t')/\tau} dt' + e^{-(t-t_0)/\tau} f_0 \left(\mathbf{x}_{i+1/2,j,k} - \mathbf{u}(t - t_0), t_0, \mathbf{u}, \xi\right), \tag{2.8}$$

were f_0 is distribution function f at t_0 and $\mathbf{x}_{i,j,k}$ is the cell center of the $(i, j, k)^{th}$ cell. The collision time τ has been treated as a local constant in obtaining the integral solution. The formal solution for f has two unknowns, namely, g and f_0 which need to be determined. An expression for τ needs also to be provided. In the discussion that follows, we set $\mathbf{x}_{i+1/2,j,k} = 0$ and $t_0 = 0$ for notational simplicity. We focus on computing the GKM equation (2.2) only to the Navier-Stokes (NS) order. To first-order, the Chapman-Enskog expansion can be written as

$$f = g - \tau(ug_x + vg_y + wg_z + g_t). \tag{2.9}$$

The distribution function around a cell interface is approximated to second-order and is given by

$$f = g+ug_x+vg_y+wg_z-\tau(ug_x+vg_y+wg_z+g_t) \equiv g(a+ax+by+cx)-\tau(au+bv+cw+A) \tag{2.10}$$

were $a \equiv g_x$, $b \equiv g_y$, $c \equiv g_z$ and $A \equiv g_t$. One can show that the coefficients a, b, c and A all have dependence on the particle velocities as follow:

$$a = a_1 + a_2u + a_3v + a_4w + \frac{1}{2}a_5(u^2 + v^2 + w^2 + \xi^2) = a_\alpha\psi_\alpha \tag{2.11}$$

were a_α in turn depends on the macroscopic flow variables. The initial gas distribution f_0 at the left and right sides of a cell interface is therefore written as

$$f_0(x, y, z, 0) = \begin{cases} g^l[1 + a^lx + b^ly + c^lz - \tau(a^lu + b^lv + c^lw - A^l)], & x \le 0, \\ g^r[1 + a^rx + b^ry + c^rz - \tau(a^ru + b^rv + c^rw - A^r)], & x \ge 0. \end{cases} \tag{2.12}$$

The equilibrium state g around a cell interface is approximates as

$$g(x, y, z, t) = g_0\left(1 + (1 - H[x])\bar{a}^lx + H[x]\bar{a}^rx + \bar{b}y + \bar{c}z + \bar{A}t\right), \tag{2.13}$$

were $H[x]$ is the Heaviside function defined as having the value 1 for $x \ge 0$ and zero for $x < 0$.

Using eqs. (2.12) and (2.13) in eq. (2.8) and performing the integration, the gas distribution function f at a cell interface is

$$\begin{aligned} f\left(\mathbf{x}_{i+1/2,j,k}, \mathbf{u}, \xi\right) &= \left((1 - \bar{A}\tau)(1 - e^{-t/\tau}) + \bar{A}t\right) g_0 \\ &+ \left((t + \tau)e^{-t/\tau} - \tau\right)\left(\bar{a}^luH[u] + \bar{a}^ru(1 - H[u]) + \bar{b}v + \bar{c}w\right) g_0 \\ &+ e^{-t/\tau}\Big(1 - (t + \tau)(a^lu + b^lv + c^lw) - \tau A^l\Big)H[u]g^l \\ &+ e^{-t/\tau}\Big(1 - (t + \tau)(a^ru + b^rv + c^rw) - \tau A^r\Big)(1 - H[u])g^r \end{aligned} \tag{2.14}$$

Details involved regarding the distribution functions g_0, g^l and g^r and their spatial and temporal derivatives ($\bar{a}^l, \bar{a}^r, \bar{b}, \bar{c}, \bar{A}$ etc.) can be found in [2, 14–16]. Finally, the time-dependent numerical flux in the x-direction at cell interface $(i+1/2, j, k)$ can be found by taking the $u-$moment of $f\left(\mathbf{x}_{i+1/2,j,k}, \mathbf{u}, \xi\right)$ in eq. (2.7)

$$\begin{pmatrix} F_\rho \\ F_{\rho u} \\ F_{\rho v} \\ F_{\rho w} \\ F_{\rho e} \end{pmatrix}_{i+1/2,j,k} = \int u \begin{pmatrix} 1 \\ u \\ v \\ w \\ 1/2(u^2+v^2+w^2+\xi^2) \end{pmatrix} f(x_{i+1/2,j,k}, t, \mathbf{u}, \xi) d\Xi. \quad (2.15)$$

Similarly, the y flux $\mathbf{G}$ and the z flux $\mathbf{H}$ can be calculated. The flow variables at the cell centre (i, j, k) can be updated using time-dependent fluxes (assuming a uniform grid) according to:

$$\begin{aligned} \mathbf{Q}^{n+1}_{i,j,k} - \mathbf{Q}^{n}_{i,j,k} &= \frac{1}{\Delta x}\int_{t^n}^{t^{n+1}} \left(\mathbf{F}_{i-1/2,j,k}(t) - \mathbf{F}_{i+1/2,j,k}(t)\right) dt \\ &+ \frac{1}{\Delta y}\int_{t^n}^{t^{n+1}} \left(\mathbf{G}_{i,j-1/2,k}(t) - \mathbf{G}_{i,j+1/2,k}(t)\right) dt \\ &+ \frac{1}{\Delta z}\int_{t^n}^{t^{n+1}} \left(\mathbf{H}_{i,j,k-1/2}(t) - \mathbf{H}_{i,j,k+1/2}(t)\right) dt. \end{aligned} \quad (2.16)$$

Recently, we have extended this to non-uniform grids as well. In the discussions thus far we have not discussed the collision time τ and the fact that the Prandtl number (Pr) which is implicit in GKM is unity. An expression for τ is obtained by requiring consistency with the NS equations at the first order of Chapman-Enskog expansion. This leads to $\tau = \mu/p$, were μ is dynamical viscosity and p is thermodynamic pressure. The actual expression for τ we use in this paper is [14]

$$\tau = \frac{\mu}{p} + \frac{|\rho_l/\lambda_l - \rho_r/\lambda_r|}{|\rho_l/\lambda_l + \rho_r/\lambda_r|}\Delta t, \quad (2.17)$$

were the second term on the RHS represents a numerical viscosity and Δt is the time step. We calculate time step using the Courant-Friedrichs-Lewy (CFL) condition [14] given by

$$\Delta t \leq \frac{C\Delta x}{(|\mathbf{u}| + c)\left(1 + \frac{2}{Re_{\Delta x}}\right)}, \tag{2.18}$$

where $C \in [0, 1]$ is the CFL number, $c = \sqrt{\gamma RT}$ is the local speed of sound and $Re_{\Delta x} = |\mathbf{u}|\Delta x/\nu$ is the cell/grid Reynolds number.

A variable Prandtl number can be rigorously introduced by subtracting the time-dependent heat flux and adding another term [14] with variable Prandtl number

$$F_{\rho e}^{\text{new}} = F_{\rho e} + \left(\frac{1}{\text{Pr}} - 1\right) q, \tag{2.19}$$

where the time-dependent heat flux is given by

$$q = \frac{1}{2}\int (u - U)\left((u - U)^2 + (v - V)^2 + (w - W)^2 + \xi^2\right) f d\Xi. \tag{2.20}$$

The flux $F_{\rho e}$ in eq. (2.16) is now replaced by $\mathbf{F}_{\rho e}^{\text{new}}$.

With a gas kinetic based computational method in place, we proceed with an evaluation study of the developed computational tool in highly compressible decaying turbulence and homogeneous shear flows.

3. WENO-ENHANCED GAS-KINETIC SCHEME FOR DIRECT SIMULATIONS OF COMPRESSIBLE TRANSITION AND TURBULENCE

3.1 Introduction

Fluid flow can be described at different scales – microscopic or molecular, mesoscopic or kinetic, macroscopic or continuum – depending on the Knudsen number [50] of the problem of interest. Knudsen number is the ratio of mean free path to the characteristic length scale of the flow of interest. For rarefied gas applications [50], the Knudsen number is large and the computational approach of choice is Direct Simulation Monte Carlo (DSMC) [52, 53] which is based on the microscopic description. At the other extreme, at very small Knudsen numbers, traditional computational fluid dynamics (CFD) methods have been based on continuum Navier-Stokes (NS) equation. Until recently, the mesoscopic kinetic description has been used mostly for theoretical analysis and formal derivation of the Navier-Stokes equation from the single particle distribution function via the Chapman-Enskog expansion.

Over the last few years, computational schemes based on mesoscopic kinetic theory have gained popularity even in the low Knudsen number continuum regime of flow. Of the various kinetic theory-based approaches, the Lattice-Boltzmann method (LBM) [22, 23, 54–58] has been widely validated in low Mach number flows for a variety of applications beyond the scope of Navier-Stokes description. The LBM represents a major paradigm shift from the traditional CFD methods and has its foundations in lattice gas automata. However, LBM has many inherent limitations in high speed flows when the Mach number approaches unity. For compressible flows, the Gas Kinetic Method (GKM) is the preferred kinetic-theory based scheme [2, 3, 5, 14–16, 26, 48, 56]. Unlike LBM which is based entirely based on mesoscopic description, the GKM scheme combines the positive attributes of both continuum and kinetic descriptions. In GKM, macroscopic conservation equations for mass, momentum and energy are updated at cell centers while their fluxes are calculated

using kinetic theory at cell interfaces. The interchange between continuum variables and mesoscopic single-particle probability distribution function is the central novelty of this approach [2,3,14,59]. In principle, fluxes calculated from the distribution function at the mesoscopic level offer several advantages over continuum constitutive relations. For example, some rarefication and higher-order effects (including Burnett equation physics) which are outside the scope of NS physics can be adequately accounted for in GKM [60–62]. Critical features of one-dimensional Mach 10 shock beyond the scope of Navier-Stokes physics have been well captured by GKM [14]. A more detailed discussion of the features of GKM is presented in Section 2.1. Overall, GKM offers important potential physical and computational advantages in high-speed non-equilibrium thermo-chemical flow regime at which closed-form analytical constitutive relations for fluxes are not possible.

Direct simulation of transition and turbulence flows is one of the important challenges to any CFD scheme. During the early stages of their development, it was unclear if the kinetic theory approaches would be viable for computations of turbulent flows in the continuum regime. Such doubts have largely been laid to rest over the last few years. Now LBM is being routinely used to simulate low Mach number turbulent flows [22, 23, 54–58, 63]. The utilization of GKM for DNS of compressible turbulent flows is still in its incipient stages [5,56]. In these works the feasibility of the GKM paradigm for turbulent flows has been well established. However, these studies have been restricted to low to moderate Mach number turbulent flows. GKM has been applied for weakly compressible turbulence in [56]. The authors [56] compare kinetic energy, dissipation rate and energy spectra in decaying isotropic turbulence computed using the multidimensional GKM, NS and LBM [57]. They establish GKM to be of comparable accuracy to NS and LBM for low turbulent Mach numbers. Liao *et al.* [5] applied GKM for decaying isotropic turbulence of moderately compressible flows. The maximum turbulent Mach number (M_t) and Taylor microscale Reynolds number (Re_λ) was 0.6 and 72.0, respectively. Based on accuracy and stability studies

of low and high order statistical quantities, Liao *et al.* showed that GKM is adequate for DNS of moderately compressible homogeneous turbulence. Applying GKM in a high turbulent Mach number flow ($M_t > 1.0$) poses greater difficulties due to stronger random shocklets, higher spatio-temporal gradients and variable transport coefficients. Extension of GKM to higher Mach number turbulent flows would therefore entail advanced reconstruction schemes to accurately interpolate cell-interface macroscopic variable values from cell-center values in the presence of shock-like steep gradients.

Flow and thermodynamic state variable interpolation capability is critical for wider use of compressible gas kinetic methods. Variables at cell-centers need to be interpolated to cell interfaces for the mesoscopic computation of numerical fluxes. The accuracy of the interpolation controls the precision in flux calculation. Reconstruction schemes should be accurate to high order in regions of smooth flow. On the other hand, it should also capture regions of very steep gradients like shocks/shocklets without adding excessive numerical dissipation. Various interpolation schemes derived from Weighted Essentially Non-Oscillatory method by Jiang and Shu [64](WENO-JS) are well suited for this purpose. One of the modifications of WENO is proposed by Martin *et. al* [65, 66] where a symmetric stencil is used. These modified schemes are referred to as: WENO-SYMOO (order-optimized), WENO-SYMBO (bandwidth optimized) and WENO-SYM-RL (with relative limiter) (see section on WENO for further details). Besides Total Variational Diminishing (TVD) nature, a typical WENO scheme is ideal for shock capturing without the use of any ad-hoc shock-detection criterion. We investigate and compare five different reconstruction schemes – van Leer (VL), Weighted Essentially Non-Oscillatory scheme by Jiang and Shu [64](WENO-JS), WENO-SYMOO [65], WENO-SYMBO [65] and WENO-SYMOO-RL [66] for their effect on numerical accuracy, efficiency and stability/robustness on gas kinetic methods. For each WENO-based method, we also examine different orders of accuracy (represented by flags r=3,4).

The objective of this study is to enhance GKM to enable direct simulation of high Mach number transition and turbulence. Toward this end we perform the following studies:

1. Examine advanced reconstruction schemes developed in the context of Navier-Stokes approaches for compatibility of use with GKM. We investigate several WENO (Weighted Essentially Non-Oscillatory) schemes [64, 65, 65, 66] of different degrees of accuracy and sophistication along with the well-known van Leer scheme [67–70].

2. Propose a detailed validation protocol and complete studies to determine the optimal reconstruction scheme in terms of accuracy and robustness. The validation protocol includes:

   (a) Examine solenoidal (vortical) and dilatational (acoustic) portions of the velocity field individually and collectively.

   (b) Validate linear physical processes by comparison with rapid distortion theory (RDT) in high Mach number homogeneous shear turbulence. This examination is critical for both transition and turbulence applications. The relevant dimensionless parameter for this study is the modal/gradient Mach number. We evaluate the model performance by comparison with RDT and analytical 'pressure-released' Burgers solution as appropriate. This represents an unique aspect of the current study as RDT and Burgers analytical solution have been seldom used in the code verification process.

   (c) Validate non-linear physical processes by comparison against a 'gold-standard' super-resolved direct simulation. This evaluation is performed in decaying isotropic turbulence with the pertinent dimensionless parameter being the turbulent Mach number.

3. Evaluate the merits of temperature *vs.* internal energy as the preferred candidate for interpolation in the calculation of energy flux. While temperature

and energy interpolation are equally permitted by governing physics, numerical considerations show that one is better suited than the other from the point of view of computational robustness.

3.2 Limiters and Interpolation

In order to calculate fluxes at the cell interface, flow variables must be interpolated from cell centers to cell interfaces. Interpolation can be applied to conservative, characteristic or primitive variables. A variety of choices of interpolation schemes are available for constructing sub-cell structures. A simple polynomial interpolation creates oscillations in the presence of steep gradients, such as shocks or boundary layers. These oscillations are termed as Gibbs phenomenon. As we increase the order of interpolation, the Gibbs phenomenon becomes prominent especially in the presence of shock/shocklets. Reconstruction schemes must switch to low order in the vicinity of shocks in order to avoid the Gibbs phenomenon. The schemes must switch back to high order elsewhere for accuracy. In the vicinity of shocks, kinematic dissipation is added implicitly to the reconstructed data by converting kinetic energy to internal energy. With most interpolation schemes, also called flux limiters, switching comes at a cost of added dissipation in smooth flow regions. In direct simulations of compressible transition and turbulence flows, added dissipation from the limiter may lead to excessive damping in regions of smooth flow. We test different interpolation schemes for their accuracy in capturing solnoidal and dilatational modes/statistics and ability to capture unsteady shocklets.

3.2.1 van Leer limiter

The van Leer (VL) [67–70] limiter is one of the most commonly used non-linear limiters due to its computational simplicity. It yields a linear distribution of variables inside a cell as shown in Fig. 3.1. The slope inside each cell is calculated using a

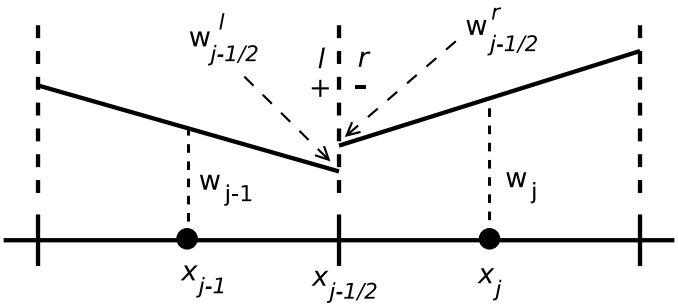

Fig. 3.1. Reconstruction of data using VL limiter.

non-linear function $L(s_+, s_-)$. With w_j as the cell averaged conservative variable and Δx as the cell width, the non-linear slope for the j^{th} cell is calculated as:

$$s_+ = (w_{j+1} - w_j)/\Delta x, \quad s_- = (w_j - w_{j-1})/\Delta x$$

$$L^j(s_+, s_-) = S(s_+, s_-)\frac{|s_+||s_-|}{|s_+| + |s_-|} \tag{3.1}$$

The variables are interpolated at cell interface $x_{j-\frac{1}{2}}$ using linear distribution inside each cell. The interpolated variable w has two different values at the interface $j-1/2$. $w^l_{j-\frac{1}{2}}$ is obtained through interpolation from the left cell and $w^r_{j-\frac{1}{2}}$ from the cell on right.

$$w^l_{j-\frac{1}{2}} = w_{j-1} + L^{j-1}(s_+, s_-)(x_{j-\frac{1}{2}} - x_{j-1})$$

$$w^r_{j-\frac{1}{2}} = w_j - L^j(s_+, s_-)(x_j - x_{j-\frac{1}{2}})$$

The difference between left and right interpolated values is small when the flow is smooth. The difference is large in the presence of steep gradients and helps in shock capturing. For resolving shocks an extremely fine grid is required.

3.2.2 Weighted Essentially Non Oscillatory scheme (WENO)

The WENO scheme, first proposed by Liu, Osher and Chan [71], and further developed by Jiang and Shu [64] is an improvement over Essentially Non-Oscillatory (ENO) scheme developed by Harten, Osher *et. al.* [72–74,]. The ENO scheme chooses the best interpolating stencil in which the solution is smoothest. Thus, a cell near a discontinuity uses a stencil from the smooth part of the neighborhood solution for interpolation. WENO employs a convex combination of interpolating polynomials on all neighboring stencils with non-linear weights assigned to each stencil. The non-linear weight $\omega^{\pm}_j$ for a stencil depends on the local smoothness of the data in that stencil. Stencils spanning nodes having a large local gradient are assigned smaller relative weight; stencils containing shocks are assigned a nearly zero

weight. In smooth flow regions, WENO interpolation with stencils spanning r cells ($r = 3$ in Figs. 3.2 and 3.3), provide a $(2r-1)^{th}$ order accuracy. We will refer the WENO proposed by Jiang-Shu [64] as WENO-JS. A typical stencil for WENO-JS scheme is shown in Fig. 3.2. The reconstruction of $w^+_{i+1/2}$ and $w^-_{i+1/2}$ at cell interface $x_{i+1/2}$ from cell centre values w_j summarized below:

$$w^+_{i+\frac{1}{2}} = \sum_{j=0}^{r-1} \omega_j^+ p_j^+(x_{i+\frac{1}{2}}), \quad w^-_{i+\frac{1}{2}} = \sum_{j=0}^{r-1} \omega_j^- p_j^-(x_{i+\frac{1}{2}})$$

$$p_0^+(x_{i+\frac{1}{2}}) = \frac{1}{3}w_{i-2} - \frac{7}{6}w_{i-1} + \frac{11}{6}w_i, \quad p_0^-(x_{i+\frac{1}{2}}) = \frac{11}{6}w_{i+1} - \frac{7}{6}w_{i+2} + \frac{2}{6}w_{i+3},$$

$$p_1^+(x_{i+\frac{1}{2}}) = -\frac{1}{6}w_{i-1} + \frac{5}{6}w_i + \frac{1}{3}w_{i+1}, \quad p_1^-(x_{i+\frac{1}{2}}) = \frac{1}{3}w_i + \frac{5}{6}w_{i+1} - \frac{1}{6}w_{i+2},$$

$$p_2^+(x_{i+\frac{1}{2}}) = \frac{1}{3}w_i + \frac{5}{6}w_{i+1} - \frac{1}{6}w_{i+2}, \qquad p_2^-(x_{i+\frac{1}{2}}) = -\frac{1}{6}w_{i-1} + \frac{5}{6}w_i + \frac{1}{3}w_{i+1},$$

$$\omega_j^\pm = \frac{\alpha_j^\pm}{\sum_{j=0}^{r-1}\alpha_j^\pm}, \quad \alpha_j^\pm = \gamma_j \left(\frac{1}{\epsilon + IS_j^\pm}\right)^2, \quad \gamma_0 = \frac{1}{10}, \gamma_1 = \frac{6}{10}, \gamma_2 = \frac{3}{10},$$

$$IS_0^+ = \frac{13}{12}\left(w_{j-2} - 2w_{j-1} + w_j\right)^2 + \frac{1}{4}\left(w_{j-2} - 4w_{j-1} + 3w_j\right)^2,$$

$$IS_1^+ = \frac{13}{12}\left(w_{j-1} - 2w_j + w_{j+1}\right)^2 + \frac{1}{4}\left(w_{j-1} - w_{j+1}\right)^2,$$

$$IS_2^+ = \frac{13}{12}\left(w_j - 2w_{j+1} + w_{j+2}\right)^2 + \frac{1}{4}\left(3w_j - 4w_{j+1} + w_{j+2}\right)^2,$$

$$IS_0^- = \frac{13}{12}\left(w_{j+1} - 2w_{j+2} + w_{j+3}\right)^2 + \frac{1}{4}\left(w_{3j+1} - 4w_{j+2} + w_{j+3}\right)^2,$$

$$IS_1^- = \frac{13}{12}\left(w_j - 2w_{j+1} + w_{j+2}\right)^2 + \frac{1}{4}\left(w_j - w_{j+2}\right)^2,$$

$$IS_2^- = \frac{13}{12}\left(w_{j-1} - 2w_j + w_{j+1}\right)^2 + \frac{1}{4}\left(w_{j-1} - 4w_j + 3w_{j+1}\right)^2.$$

where $\epsilon \sim 10^{-10}$ is a small number to avoid division by zero, $\omega_j^{\pm}$ are the non-linear weights and γ_j are the linear weights. The smoothness indicator $IS_j^{\pm}$, for each stencil S_j, measures smoothness of the data in the target cell I_i and is given by

$$IS_j = \sum_{l=1}^{r} \int_{I_i} \Delta_i^{2l-1} \left(\frac{\partial^l}{\partial x^l} p_j(x) \right)^2 dx. \tag{3.2}$$

The bandwidth optimized WENO scheme (WENO-SYMBO) [65], order optimized WENO scheme (WENO-SYMOO) [65] and WENO with a 'relative-smoothness limiter' (WENO-RL) [66] are all improvements over WENO-JS. All three schemes (WENO-SYM) are less dissipative compared to WENO-JS and are optimized to maximize the order of accuracy and bandwidth while minimizing dissipation. For a stencil containing r cells, WENO-SYM provides $2r^{th}$ order accuracy in smooth regions. Stencils for WENO-SYM ($r = 3$) are shown in Fig. 3.3. In contrast to WENO-JS, stencils for WENO-SYM are symmetric about $(i + 1/2)$. A generalized formulation of WENO-SYM is summarized below

$$w_{i+\frac{1}{2}}^{+} = \sum_{k=0}^{r} \omega_k^{+} (p_k^{+})^r,$$

$$(p_k^{+})^r (x_{i+\frac{1}{2}}) = \sum_{l=0}^{r-1} a_{kl}^r w_{i-r+k+l+1},$$

where a_{kl}^r are the stencil coefficients (see the appendix of [65]). The non-linear weights ω_k are defined by

$$\alpha_k^{+} = \frac{C_k^r}{(\epsilon + IS_k^{+})^p}, \quad p \in [1, 2]; \qquad \omega_k^{+} = \frac{\alpha_k^{+}}{\sum_{k=0}^{r-1} \alpha_k^{+}},$$

$$IS_k^{+} = \sum_{m=1}^{r-1} \left(\sum_{l=0}^{r-1} d_{kml}^{r+} w_{i-r+k+l+1} \right); \quad IS_r = \max_{0 \le k \le r} (IS_k).$$

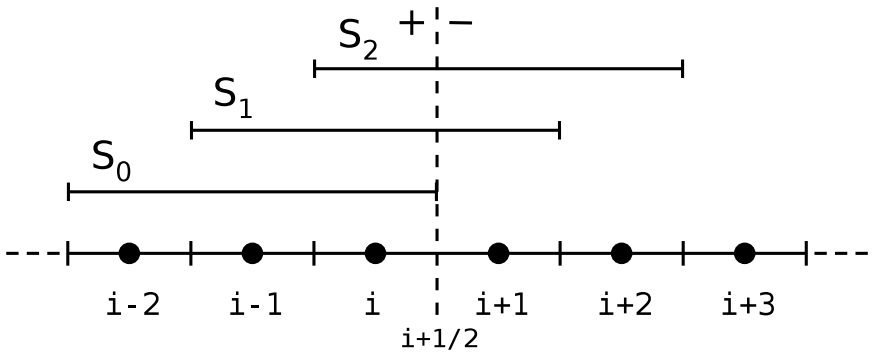

Fig. 3.2. Candidate stencils S_k for reconstruction of $w^+_{i+\frac{1}{2}}$ using WENO-JS ($r = 3$). For reconstruction of $w^-_{i+\frac{1}{2}}$ the stencils are mirror image about $(i + 1/2)$.

The order-optimized and bandwidth-optimized linear weights C^r_k can be found in the appendix of ref. [65]. WENO-RL [66] prevents unnecessary use of WENO adaptation in smooth regions thereby improving WENO dissipation characteristics in compressible turbulence. The smoothness indicator in WENO-RL is given by

$$IS_k = \begin{cases} 0 & , R(IS) < \alpha_{RL} \approx 10, \\ IS_k & \text{otherwise} \end{cases}$$

$$R(IS) = \frac{\max_{0\le k\le r} IS_k}{\epsilon + \min_{0\le k\le r} IS_k}.$$

The relative smoothness limiter α_{RL} is chosen to be 10 based on past experience.

3.2.3 Interpolation of energy or temperature?

Negative temperatures arising due to the Gibbs phenomenon at high turbulent Mach numbers is a common problem [75] in DNS of compressible turbulence. We interpolate temperature (primitive variable) rather than energy (conservative vari-

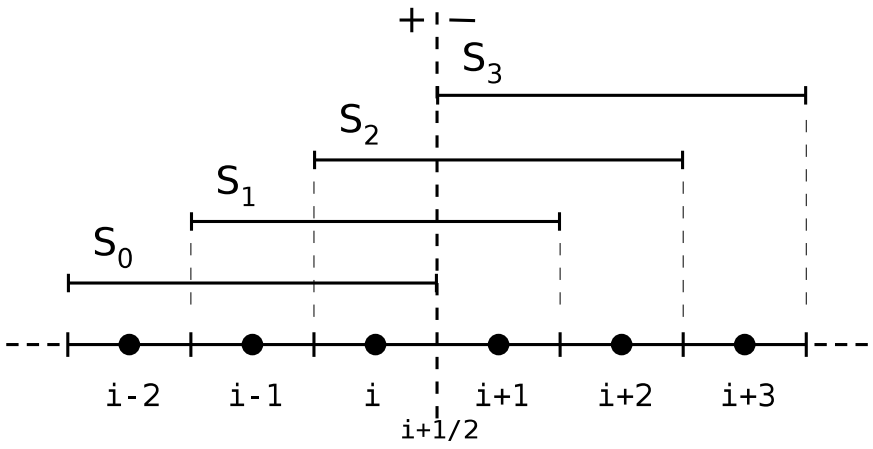

Fig. 3.3. Candidate stencils S_k for reconstruction of $w^+_{i+\frac{1}{2}}$ using WENO-SYM ($r = 3$). For reconstruction of $w^-_{i+\frac{1}{2}}$ the stencils are mirror image about $(i + 1/2)$.

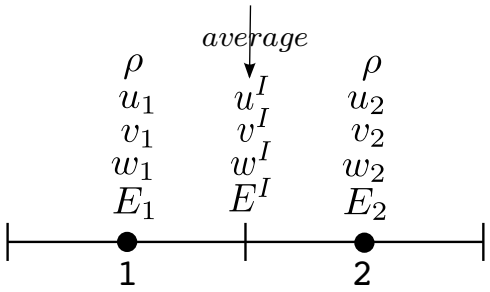

Fig. 3.4. Interpolation of energy E or temperature T at cell interface $i + \frac{1}{2}$.

able) to calculate fluxes at the cell interface in order to avoid negative temperatures. The other interpolated variables are conserved quantities $(\rho, \rho u, \rho v, \rho w)$. The difference between temperature and energy interpolation is negligible when high order interpolation scheme like WENO is used. Energy, temperature and velocity field are related through the expression

$$E = \frac{1}{2}\rho\left(u^2 + v^2 + w^2\right) + \rho C_v T. \tag{3.3}$$

Eq. (3.3) is non-linear in both conservative and primitive variables. Non-linearity is the obstacle in keeping the interpolated value of variables and eq. (3.3) consistent. Let us consider a simple case as shown in Fig. (3.4) where ρ is spatially uniform i.e. $\rho_1 = \rho_2 = \rho$ and we take averages for interpolation i.e. at interface $u^I = (u_1 + u_2)/2$ and same for v, w, E. Using $E^I = (E_1 + E_2)/2$ we can find the temperature T^I at the cell interface

$$T^I = \frac{T_1 + T_2}{2} + \frac{1}{8C_v}\left[(u_1 - u_2)^2 + (v_1 - v_2)^2 + (w_1 - w_2)^2\right]. \tag{3.4}$$

The correct interpolation of the temperature at the interface is $T^I = (T_1 + T_2)/2$. Thus, by interpolating energy we get incorrect temperature at cell interface. The

error is larger when gradients are steeper–*i.e.* $(u_1 - u_2)^2, \ldots, (w_1 - w_2)^2$ is large. In the presence of strong shocks the error is maximum. Since the temperature is used explicitly in GKM, especially in the Maxwellian distribution, inconsistent temperature at a cell interface can lead to instability in the numerical method. For low Mach numbers, the energy equation does not play a major role and therefore minor inconsistencies in temperature can be tolerated. At high turbulent/gradient Mach numbers, changes in temperature is large near steep gradients (shocks and shocklets), and inconsistent temperature interpolation may eventually lead to negative temperature. We therefore choose to interpolate temperature and tolerate inaccuracies in eq. (3.3) at the cell-interface.

3.3 Modal Validation in Homogeneous Shear Flow

In this section, we study the evolution of different Fourier perturbation waves in a homogeneous shear flow setup. This validation isolates many of the linear physics effects and hence is relevant for transition as well as turbulence applications. We compare results against inviscid Burgers 'pressure-release' limit which is essentially Navier-Stokes equation without pressure and viscous terms. The results are also compared against Rapid Distortion Theory [76–78], a linear theory valid for initial times in turbulence when the effect of non-linearity is negligible. The two families of Fourier perturbation modes considered are: solenoidal and dilatational. The solenoidal perturbation isolates the vortical portion of the flow field. The dilatational fluctuations correspond to expansion waves, compression waves, shocks and rarefactions. We test the accuracy of VL and WENO interpolation, in capturing the evolution of the two mode families.

The parameter characterizing analysis of Fourier modes in a homogeneous shear flow, is the gradient Mach number, M_g, defined as

$$M_g = \frac{Sl}{\sqrt{\gamma RT}}, \tag{3.5}$$

where S is the mean shear and l is the relevant lengthscale for the problem. We choose l to be the wavelength of the perturbation wave.

3.3.1 Governing equation

The Navier-Stokes equations governing the flow are

$$\frac{\partial \rho}{\partial t} + \frac{\partial \rho u_i}{\partial x_i} = 0, \tag{3.6}$$

$$\frac{\partial \rho u_i}{\partial t} + \frac{\partial (\rho u_i u_j + p\delta_{ij})}{\partial x_j} = \frac{\partial \sigma_{ij}}{\partial x_j}, \tag{3.7}$$

$$\frac{\partial E}{\partial t} + \frac{\partial [(E+p)u_i]}{\partial x_i} = \frac{\partial (\sigma_{ij} u_j)}{\partial x_i} - \frac{\partial}{\partial x_i}\left(\kappa \frac{\partial T}{\partial x_i}\right). \tag{3.8}$$

The viscous stress tensor σ_{ij} is given by a constitutive relation

$$\sigma_{ij} = \mu \left[\frac{\partial u_i}{\partial x_j} + \frac{\partial u_j}{\partial x_i} - \frac{2}{3}\delta_{ij} \frac{\partial u_k}{\partial x_k} + \eta \delta_{ij} \frac{\partial u_k}{\partial x_k} \right] \tag{3.9}$$

where μ is the dynamic viscosity coefficient, κ is the thermal conductivity and $\eta = \frac{2N}{3(K+3)}$ is the bulk viscosity. N is the number of internal degrees of freedom given by $N = \frac{5-3\gamma}{\gamma-1}$, where γ is the ratio of specific heats. The GKM implementation here can be considered as a straight-forward numerical method to solve for the NS equations. The fact that kinetic-theory arguments are used to calculate various fluxes is not relevant to the discussions in the remainder of the paper.

The evolution equation of turbulent kinetic energy in homogeneous shear $S\left(=\frac{\partial u}{\partial x_3}\right)$ derived by Favre averaging [79, 80] the momentum equation (5.2.1) is given as:

$$\frac{dK}{dt} = P - \epsilon_s - \epsilon_c + \frac{\overline{p'd'}}{\bar{\rho}}, \tag{3.10}$$

where $K = \frac{1}{2}\widetilde{u_i u_i} = \frac{1}{2}\overline{\rho u_i' u_i'}/\bar{\rho}$ is the Favre averaged turbulent kinetic energy (TKE), $P = -S\widetilde{u_1' u_3'}$ is the production of TKE, $\epsilon_s = \bar{\nu}\overline{\omega_i'\omega_i'}$ is the solenoidal dissipation rate, $\epsilon_c = \frac{4}{3}\bar{\nu}\overline{d'^2}$ is the compressible/dilatational dissipation rate and $\overline{p'd'}$ is the pressure dilatation. Here $d' = \frac{\partial u_i'}{\partial x_i}$ is the fluctuation in dilatation ($\nabla \cdot \mathbf{u}$), ω' is the fluctuation in vorticity ($\nabla \times \mathbf{u}$) and $p' = \left(\rho'\overline{T} + \rho' T' + \overline{\rho} T' - \overline{\rho' T'}\right) R$ is the fluctuation in pressure. We study the kinetic energy budget of eq. (5.2.1) in all homogeneous shear simulations.

We compare results from DNS against Burgers 'pressure-release' limit and Rapid Distortion theory. The pressure-release limit is the solution to the inviscid Burgers equation

$$\frac{\partial u_i}{\partial t} + u_j \frac{\partial u_i}{\partial x_j} = 0. \tag{3.11}$$

The equations for flow and thermodynamic fluctuations in a homogeneous shear flow are:

$$\frac{du_i'}{dt} = -u_j' \frac{\partial \overline{U_i}}{\partial x_j}; \quad \frac{d\rho'}{dt} = \frac{dp'}{dt} = 0. \tag{3.12}$$

The corresponding linear equations in spectral space [81] are:

$$\frac{d\widehat{\rho'}}{dt} = -i\bar{\rho}\widehat{u_j'} k_j, \tag{3.13}$$

$$\frac{d\widehat{u_i'}}{dt} = -\frac{i}{\bar{\rho}}\widehat{p'} k_i - \widehat{u_j'} S_{ij}, \tag{3.14}$$

$$\frac{d\widehat{p'}}{dt} = -i\gamma\bar{p}\widehat{u_j'} k_j, \tag{3.15}$$

where $\bar{(.)}$ and $\hat{(.)}$ represent the mean flow variables and Fourier amplitudes, respectively. The evolution equation for wave-vector k_i is given by

$$\frac{\partial k_i}{\partial t} + \bar{u}_j \frac{\partial k_i}{\partial x_j} = -k_i \frac{\partial \bar{u}_j}{\partial x_j}. \tag{3.16}$$

3.3.2 Numerical setup and boundary conditions

The computational domain is a cubical box of dimension $l = 2\pi$. The box is discretized into $N_x \times N_y \times N_z$ cells with $N_x = 256, N_y = 256$ and $N_z = 512$ cells along x, y, z directions, respectively. We apply uniform shear in u_1 along the x_3 direction such that $S = \frac{\partial u_1}{\partial x_3}$ gives mean shear. Periodic boundary condition is applied for boundaries normal to the x_1 and x_2 directions. For boundaries normal to x_3 (the shear direction), we apply shear-periodic boundary condition [82–85]

$$\phi(t, x + m_1 L_x, y + m_2 L_y, z + m_3 L_z) = \phi(t, x - S m_3 L_z t, y, z) \tag{3.17}$$

L_x, L_y, L_z denote the dimensions of the box in the three spatial directions and m_1, m_2, m_3 are arbitrary integers. Along the direction of shear, only fluctuating component of velocity is periodic while the mean velocity is specified to maintain the prescribed shear S.

3.3.3 Mode selection

The modes are selected on the basis of fastest growth of vorticity and dilatation. Precursive RDT calculations demonstrate that $\bar{u}(t = 0) = (0, 0, \sin(ny))$ leads to most rapid growth of vorticity and more importantly does not develop any dilatation. Here 'n' is any integer ($\neq 0$). Similarly, $\bar{u}(t = 0) = (0, 0, \sin(nx))$ yields the most rapid growth of dilatational velocity component. The behavior of any other velocity perturbation mode can be explained based on these two modes. Interest-

ingly, dilatational mode does not grow in incompressible homogeneous turbulence. The schematics of solenoidal and dilatational mode are given in Figs. 3.5 and 3.9, respectively. In the investigation we use $n = 1$, unless otherwise specified. Larger the value of n, sooner will be the onset of viscous effects.

The evolution of kinetic energy for Burgers flow (4.10) is given by:

$$\frac{\partial\left(\frac{1}{2}\overline{u_i u_i}\right)}{\partial t} \equiv \frac{\partial K}{\partial t} = -\overline{u_i u_k}\frac{\partial\left\langle U_i\right\rangle}{\partial x_k}, \tag{3.18}$$

The kinetic energy growth for solenoidal or dilatational modes can be analytically evaluated:

$$\frac{K(t)}{K_0} = 1 - \frac{\overline{u_1 u_3(t=0)}}{K_0} nSt + \frac{\overline{u_3 u_3(t=0)}}{K_0} n^2 S^2 t^2 = 1 + n^2 S^2 t^2. \tag{3.19}$$

3.3.4 Solenoidal mode

The initial perturbation wave given by $\mathbf{u} = (0, 0, \sin(ny))$ constitutes the solenoidal mode. The schematic diagram for the solenoidal/incompressible mode is shown in Fig. (3.5) (not to scale). For the solenoidal mode, we examine the budget of turbulent kinetic energy equation (5.2.1) for initial gradient Mach number $M_g = 5$, wavenumber $n = 1$ and $\overline{u_i u_i}(t = 0) = 2.0$ in Fig. (3.6). Interpolation used for Fig. 3.6(a) is WENO-SYMOO (r=3) and for Fig. 3.6(b) is VL. The equality of left hand side $\left(\frac{dK}{dt}\right)$ and right hand side of Eq. (5.2.1) shows that the overall budget is self consistent.

We compare the evolution of turbulent kinetic energy from DNS simulations against results from Rapid Distortion Theory and the exact Burgers solution in Figs. (3.7) and (3.8). DNSs in Figs. 3.7(a) and 3.8(a) use WENO-SYMOO (r=3) interpolation while VL is used in Figs. 3.7(b) and 3.8(b). Comparing Figs. 3.7(a) and 3.7(b) we find VL is of comparable accuracy to WENO schemes for the solenoidal modes. Similar conclusion can be drawn from Figs. 3.8(a) and 3.8(b) where we

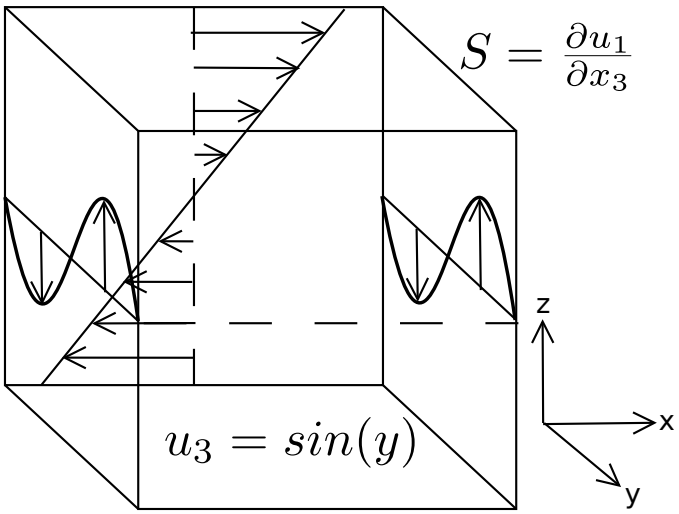

Fig. 3.5. Solenoidal mode: schematic of the computational domain showing mean shear and initial fluctuation (not to scale).

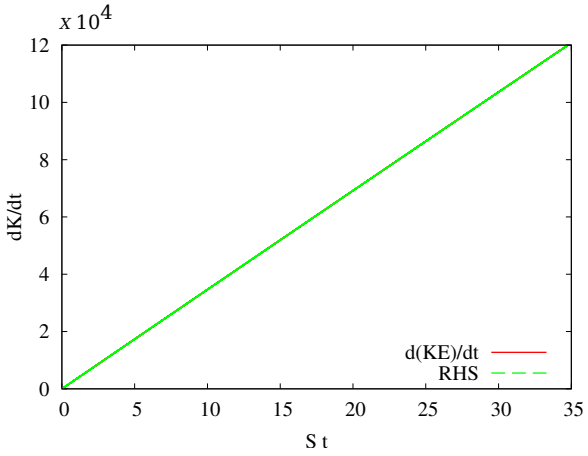

(a)

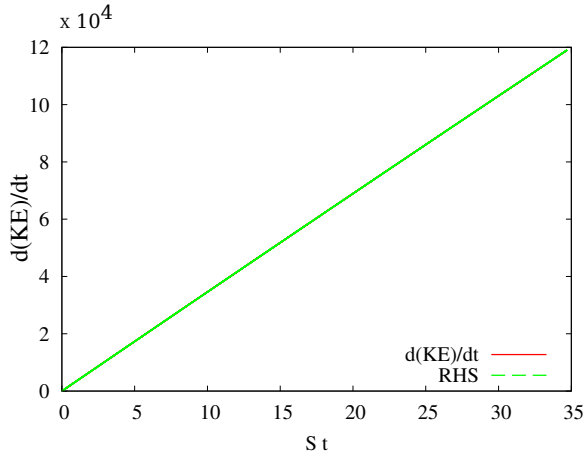

(b)

Fig. 3.6. Solenoidal mode ($M_g = 5, n = 1$, $\overline{u_i u_i}(t = 0) = 2.0$): energy budget in DNS of eq. (5.2.1) using (a) WENO-SYMOO (r=3) (b) VL interploation.

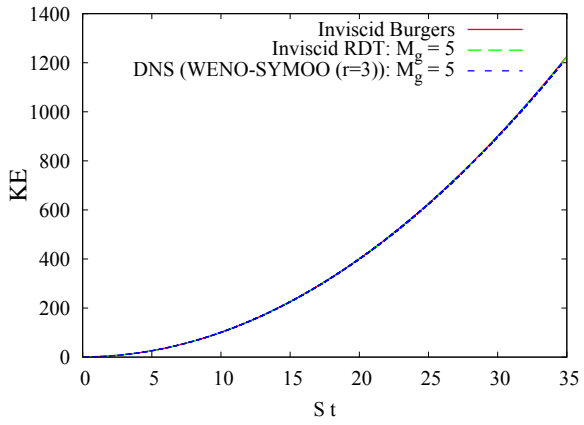

(a)

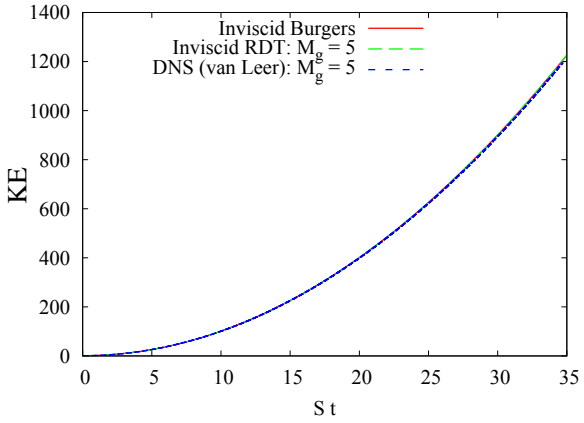

(b)

Fig. 3.7. Solenoidal mode ($M_g = 5, n = 1$, $\overline{u_i u_i}(t = 0) = 2.0$): evolution of TKE in DNS using (a) WENO-SYMOO (r=3) (b) VL interploation.

have larger initial gradients by starting the simulations with $n = 5$. The DNS kinetic energy simulation in Fig. (3.8) is lower than Burgers and RDT results due to presence of viscosity and initially steeper gradients.

We conclude that since solenoidal mode does not have very steep gradients or shocks, dissipative nature of VL is not very prominent and hence VL performs equally well as WENO schemes.

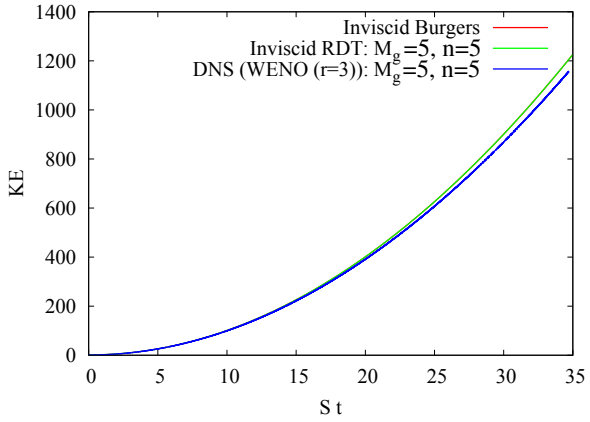

(a)

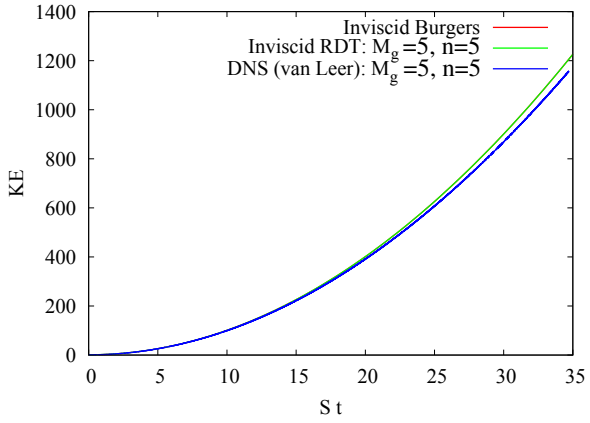

(b)

Fig. 3.8. Solenoidal mode ($M_g = 5, n = 5$, $\overline{u_i u_i}(t = 0) = 2.0$): evolution of TKE in DNS using (a) WENO-SYMOO (r=3) (b) VL interploation.

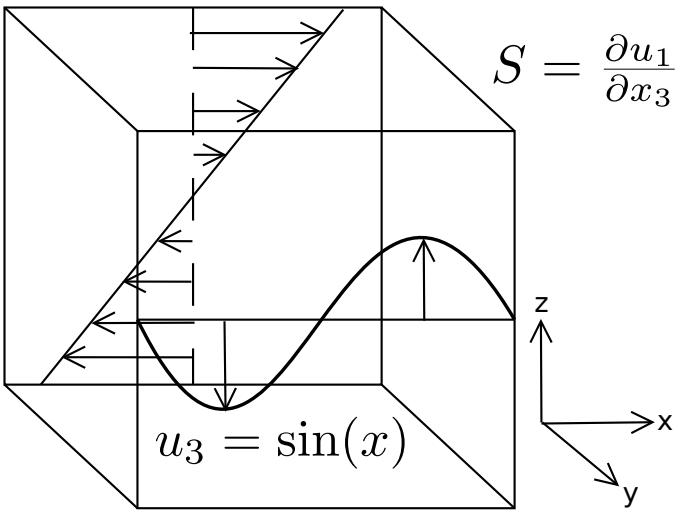

Fig. 3.9. Dilatational mode: schematic of the computational domain showing mean shear and initial fluctuation (not to scale).

3.3.5 Dilatational mode

We next investigate the performance of the interpolation schemes for the simulations of dilatational mode where very steep gradients arise in the flow. An initial perturbation wave given as $\mathbf{u} = (0, 0, \sin(nx))$ constitutes the dilatational mode. The schematic diagram for the dilatational/compressible mode in a homogeneous shear flow setup is shown in Fig. (3.9). the kinetic energy budget (5.2.1) for an initial gradient Mach number $M_g = 5$, wavenumber $n = 1$ and $\overline{u_i u_i}(t = 0) = 2.0$ is shown in Fig. (3.10). Figs. 3.10(a) and 3.10(b) use WENO-SYMOO (r=3) and VL interpolation schemes, respectively. Both, VL and WENO-SYMOO show precise energy budget match and hence each computation can be considered internally self-consistent. Although simulations using VL and WENO-SYMOO start with identical initial conditions, the evolution of dK/dt is very different in the two cases. The overly dissipative VL leads to faster decay of kinetic energy, which is evident from comparison of evolution of DNS TKE from figs. 3.11(a) and 3.11(b).

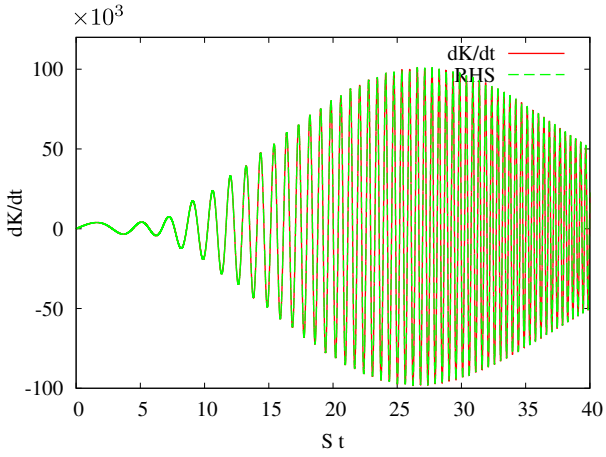

(a)

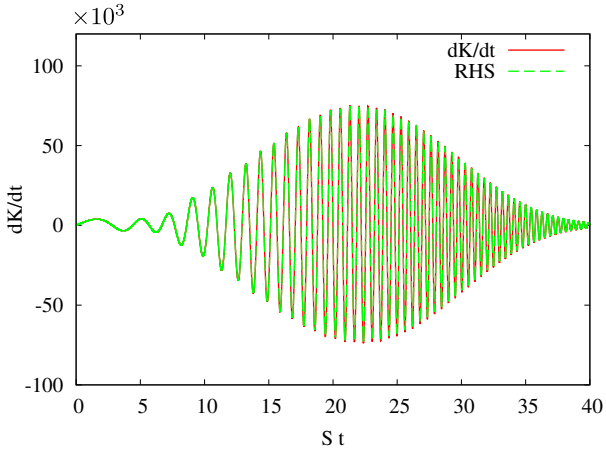

(b)

Fig. 3.10. Dilatational mode ($M_g = 5, n = 1, \overline{u_i u_i}(t = 0) = 2.0$): energy budget in DNS of eq. (5.2.1) using (a) WENO-SYMOO (r=3) (b) VL interpolation.

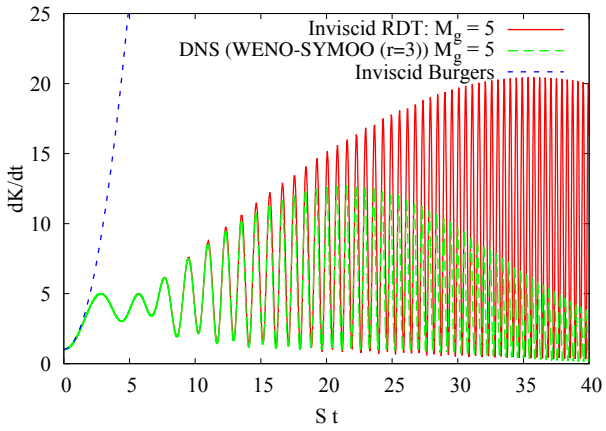

(a)

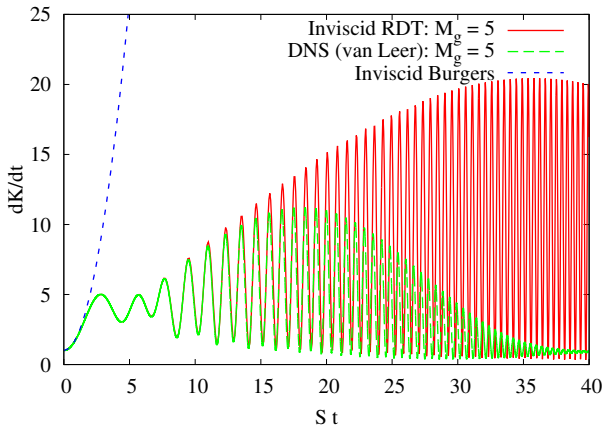

(b)

Fig. 3.11. Dilatational mode ($M_g = 5, n = 1$, $\overline{u_i u_i}(t = 0) = 2.0$): evolution of TKE in DNS using (a) WENO-SYMOO (r=3) (b) VL interpolation.

We also compare the evolution of kinetic energy from DNS simulations against results from Rapid Distortion Theory (RDT) and Burgers limit (3.19) in Figs. 3.11(a) and 3.11(b). Both VL and WENO-SYMOO simulations follow the Burgers limit up to shear time $St \approx 2$ as does the result from linear theory–RDT. For $St > 2$ DNS and RDT TKE deviates from the Burgers evolution, which is the limiting case of $M_g \to \infty$, due to the action of pressure. Results from DNS and Linear theory match closely till $St \approx 10$. For $St > 10$, non-linear effects and viscosity start playing a significant role, thus making solutions increasingly different. The initial match with Burgers limit and RDT supports the validity and accuracy of DNS simulations.

Thus the results of section (3.3) indicate that both VL and WENO-based limiters are equally effective for solenoidal perturbations. This is to be expected as the vortical field is typically devoid of sharp gradients. However, for the dilatation perturbations, WENO-based interpolation is clearly superior to VL. The WENO schemes are significantly less dissipative. The agreement with RDT clearly shows that the WENO-based numerical schemes captures the linear physics of transition and turbulence quite accurately. Since linear physics is dominant only in the large scales, we do no show results with larger n, which correspond to small scales.

3.4 Compressible Decaying Isotropic Turbulence

Non-linear effects dominate small-scale turbulence behavior. Therefore it stands to reason that the fidelity of the numerical method at high wave numbers be assessed in the benchmark decaying isotropic turbulence (DIT) flow. The flow domain is a cube of dimension l, $l^3 = (2\pi)^3$ with periodic boundaries. The box is discretized into N^3 cells with $N \in (96, 128, 192, 256, 512)$ cells along each direction. Most simulations are for $N \in (128, 192)$ while $N \in (64, 96, 256, 512)$ are used in the grid convergence study. Due to a very high spatial and temporal resolution, 512^3 simulation is nominated as the 'gold-standard'. The parameters characterizing the flow are

the turbulent Mach number M_t and Taylor microscale Reynolds number Re_λ defined as:

$$M_t = \frac{\sqrt{\langle u_i u_i \rangle}}{\sqrt{\gamma R \langle T \rangle}}, \quad Re_\lambda = \frac{\langle \rho \rangle u' \lambda}{\langle \mu \rangle} = \frac{\langle u_i u_i \rangle}{\mu \sqrt{\Omega}}, \tag{3.20}$$

where $\Omega = \langle \omega_i' \omega_i' \rangle$ is enstrophy and $\omega' = \nabla \times \mathbf{u}$ is fluctuating vorticity. In some literature [56, 86] an alternate definition of Taylor microscale Reynolds number is used which is defined as

$$Re_{\lambda_1} = \frac{\langle u_i u_i \rangle}{\sqrt{3\nu\epsilon/5}}, \tag{3.21}$$

where ϵ is the 'pseudo dissipation' [86] given by $\epsilon = \langle \nu u_{i,j} u_{i,j} \rangle$.

3.4.1 Governing equations

The Navier-Stokes equations governing the flow are given in eqs. (5.2.1)–(5.2.1). The Prandtl number for the simulations is assumed to be constant at $\mathrm{Pr} = 0.7$. The viscosity is assumed to follow the Sutherland's law given as

$$\mu = \mu_r \left(\frac{T}{T_r} \right)^{\frac{3}{2}} \frac{T_{ref} + T_0}{T + T_0} \tag{3.22}$$

where μ_r, T_r and T_0 are reference dynamic viscosity, reference temperature and Sutherland temperature, respectively. T_0 is taken to be $110.4K$.

The evolution of turbulent kinetic energy in DIT is given by:

$$\frac{d}{dt}\left(\overline{\rho} K\right) = -\overline{\rho}\epsilon + \overline{p' d'} = \overline{\rho}\left(\overline{\nu} \overline{\frac{\partial u_i}{\partial x_j} \frac{\partial u_i}{\partial x_j}} \right) + \overline{p' \left(\frac{\partial u_i}{\partial x_i} \right)}, \tag{3.23}$$

where $\overline{\rho}\epsilon$ is the turbulent dissipation rate and $\overline{p'd'}$ is the pressure dilatation. Pressure fluctuation p' is given by: $p' = \left(\rho' \overline{T} + \rho' T' + \overline{\rho} T' - \overline{\rho' T'} \right) R$. To study the effect of compressibility, total turbulent dissipation rate can be further decomposed as [87]

$$\epsilon = \epsilon_s + \epsilon_c \tag{3.24}$$

where $\epsilon_s = \overline{\nu\omega_i'\omega_i'}$ is the solenoidal dissipation rate and $\epsilon_c = \frac{4}{3}\overline{\nu d'^2}$ is the compressible dissipation rate. Here $\omega' = \nabla \times \mathbf{u}$ is the fluctuating vorticity and $d' = \nabla \cdot \mathbf{u}$ is the fluctuating divergence of velocity. We will use eq. (3.23) to examine the energy budget of DIT simulations.

3.4.2 Initial and boundary conditions

We start our simulations from a 3-D random, isotropic ($\langle uu \rangle = \langle vv \rangle = \langle ww \rangle$) and solenoidal ($\nabla \cdot \mathbf{V} = 0$) velocity field. Symbol $\langle . \rangle$ represents volume average. The temperature and density are initially uniform in the box. We energize only large scales in the flow by restricting energy containing wavenumbers in the range $k \in [1, 8]$. The velocity field is periodic and initial satisfies a specified one-dimensional energy spectra [22, 56, 88]

$$E(k,0) = \frac{\hat{u}_i \hat{u}_i^*}{4\pi k^2} = A k^4 e^{-Bk^2}, \quad k \left(= \sqrt{k_x^2 + k_y^2 + k_z^2}\right) \in [1, 8] \tag{3.25}$$

where $B = 0.54$, $\hat{u}_i$ is the Fourier amplitude and $\hat{u}_i^*$ is its complex conjugate. The coefficient A magnifies the velocity field uniformly throughout the domain and is chosen to achieve the required turbulent Mach number. The steps involved in the generation of an initial velocity field are

1. Generate an initial velocity field (u_1, u_2, u_3) in the physical space ($N_x \times N_y \times N_z$ points) using a 'uniform random number generator' with individual velocity components in the range $(-1, 1)$.

2. Transform the velocity field to Fourier space using forward Discrete Fourier Transform (DFT).

3. Impose the incompressibility condition ($\vec{\hat{u}} \cdot \vec{k} = 0$) by projecting $\vec{\hat{u}}$ on the plane normal to $\vec{k}$. $\vec{\hat{u}}^I = \vec{\hat{u}} - \vec{k}(\vec{k}.\vec{\hat{u}})/k^2$. Replace $\vec{\hat{u}}$ with $\vec{\hat{u}}^I : \ \vec{\hat{u}} \rightarrow \vec{\hat{u}}^I$.

4. Impose the desired energy spectra $E(k,0) = Ak^4 e^{-Bk^2}$ and wavenumber restriction

$$\vec{\hat{u}} \rightarrow \frac{\vec{\hat{u}}}{|\vec{\hat{u}}|}\sqrt{\frac{E(k,0)}{4\pi k^2}} \quad \text{if} \quad k \in [1,8], \quad \text{else} \quad \vec{\hat{u}} = 0. \tag{3.26}$$

5. Transform back to physical space using inverse DFT.

This procedure yields a velocity field which is random, isotropic, incompressible and satisfies a desired energy spectra. We generate initial velocity fields with $N = 96, 128, 192, 256, 512$ with identical energy spectra and physical space velocity fields for grid convergence simulations. We also choose a kinematic viscosity ν to get a desired Taylor Reynolds number $Re_\lambda = \frac{\langle u_i u_i \rangle}{\mu\sqrt{\Omega}}$.

3.4.3 Quantities studied

In sections to follow, we present the time evolution for the volume averaged statistics: $K(t), \epsilon(t), \epsilon_s, \epsilon_c$ and $\overline{p'd'}$. These terms appear explicitly in the evolution equation of turbulent kinetic energy (3.23). We also study higher order moments of the velocity gradient: skewness S_u and flatness (kurtosis) F_u which are given as

$$S_u(t) = \frac{1}{3}\sum_{i=1,3} S_{u_i}, \quad S_{u_i} = \frac{\overline{\left(\frac{\partial u_i}{\partial x_i}\right)^3}}{\left(\overline{\left(\frac{\partial u_i}{\partial x_i}\right)^2}\right)^{\frac{3}{2}}}, \tag{3.27}$$

$$F_u(t) = \frac{1}{3}\sum_{i=1,3} F_{u_i}, \quad F_{u_i} = \frac{\overline{\left(\frac{\partial u_i}{\partial x_i}\right)^4}}{\left(\overline{\left(\frac{\partial u_i}{\partial x_i}\right)^2}\right)^2}. \tag{3.28}$$

3.4.4 Grid and time convergence study

Before proceeding with the comparison of different interpolation schemes, we present grid and time convergence studies. The study serves dual purposes: first, it is an additional validation of the GKM code in the non-linear turbulence regime;

and second, it ensures that the grid and time steps used for further simulations are sufficient to resolve/capture the desired physics. We use six different grids with $64^3, 96^3, 128^3, 192^3$, 256^3 and 512^3 grid points to demonstrate grid convergence. For NS simulations of decaying isotropic turbulence with initial $M_t = 1.5$, Martin *et. al.* [65] report grid convergence with 196^3 box. We will also demonstrate time-convergence by comparing simulations using 128^3 grid with identical initial conditions but with different CFL numbers.

The initial conditions for grid convergence studies should be identical in-order to derive meaningful conclusions. Since the velocity field used for DIT simulation is very complex, we need to take extra care in generation of identical velocity field for different grid sizes. We generate an identical initial data in physical space for different grids by ensuring identical data in Fourier space. We compare the one dimensional energy spectra $E(\kappa)$ of the initial field for 128^3 and 256^3 grid against the desired spectra (Eq. 4.14) in Figs. 3.12(a) and 3.12(b). We can see that the energy spectra coincide, thereby ensuring an exact match in the Fourier space.

In Fig. (3.13) we present grid convergence for DIT case with $M_t = 1.2, Re_\lambda = 46.4$. We compare kinetic energy, dissipation and probability density function for u velocity in Figs. (3.13(a)) and (3.13(b)), respectively. With increasing resolution, we find concurrence in results. We find 128^3 to be sufficiently resolved and use 128^3 and 192^3 grids for further simulations. We also show time step convergence for 128^3 grid for $M_t = 1.2, Re_\lambda = 46.4$ in Fig. (3.14) by choosing three different CFL numbers (eq. 2.18) $C \in [0.2, 0.4, 0.8]$.

3.4.5 Comparison between different interpolation schemes for non-linear physics

We now present comparisons of different interpolation schemes for a range of turbulent Mach numbers and Taylor microscale Reynolds number in 128^3 domain. All simulations start with an incompressible velocity field following a specified energy-spectra (4.14). As turbulence evolves, triadic interactions arising due to the inertial

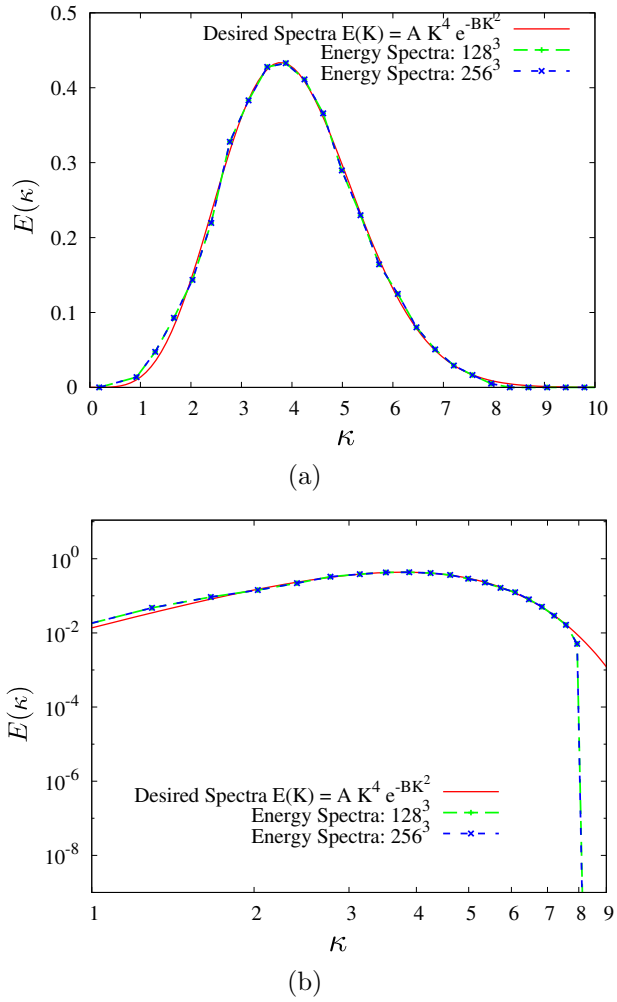

Fig. 3.12. Comparison of one dimensional energy spectra of the initial velocity field for 128^3 and 256^3 grid against the desired spectra $E(\kappa) = A\kappa^4 e^{-B\kappa^2}$: (a) x-y axes linear scale (b) x-y axes logarithmic scale.

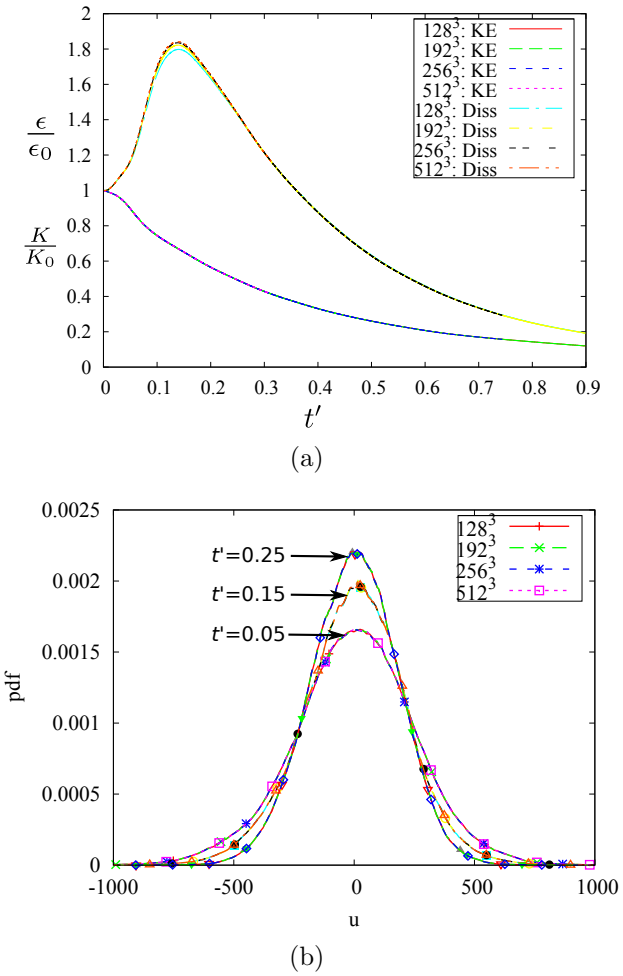

Fig. 3.13. Grid convergence study for 128^3, 192^3, 256^3 and 512^3 mesh ($M_t = 1.2, Re_\lambda = 46.4$): (a) kinetic energy and dissipation, (b) probability density function for u for different times $t' = 0.05, 0.15$ and 0.25.

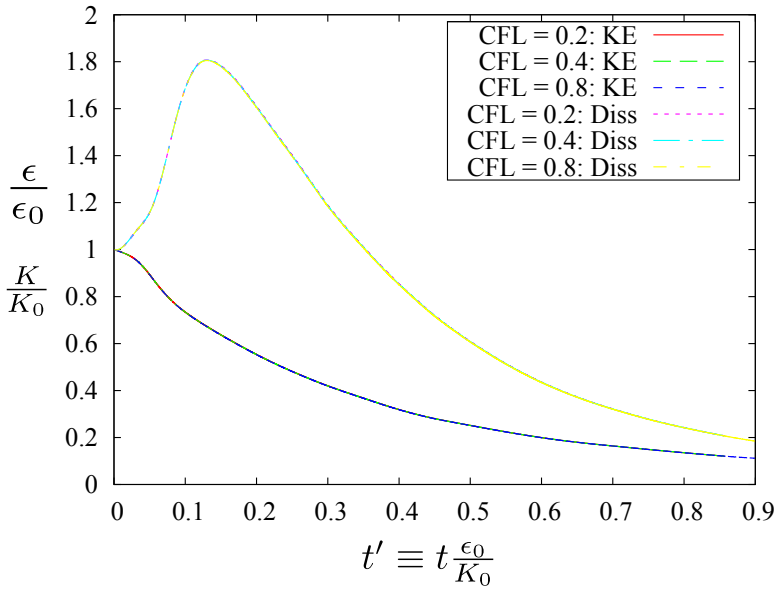

Fig. 3.14. Time step convergence study ($M_t = 1.2, Re_\lambda = 46.4$): comparison of kinetic energy and dissipation for 128^3 mesh with CFL $C \in (0.2, 0.4, 0.8)$.

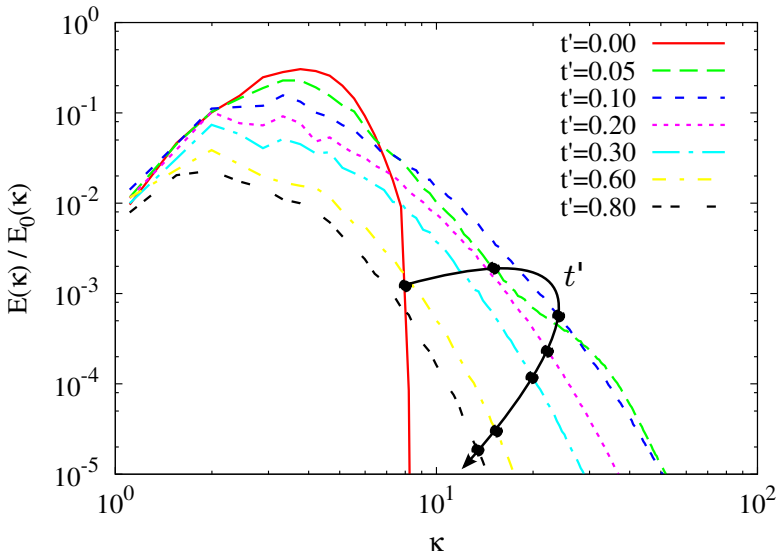

Fig. 3.15. Evolution of energy spectra for DHIT of $M_{t_0} = 2.25, Re_\lambda = 40$.

term lead to a forward cascade of energy. Forward cascade in turn leads to generation of smaller wavenumbers and thus gradient steepening. Large gradients lead to an increase in turbulent dissipation rate. This leads to an initial increasing trend in turbulent dissipation which peaks at 0.15 eddy turnover time. Since there is no mean flow to supply energy to turbulence, DIT (unforced) decays with time. When gradients are large enough to be quickly dissipated by action of viscosity, further gradient steepening stops. The steepest gradients correspond to the peak of turbulent dissipation and the farthest extent of energy spectra (see Fig. 3.15).

We compare the performance of different reconstruction schemes: VL scheme, WENO-JS (r=3,4), WENO-SYMOO (r=3,4), WENO-SYMBO (r=3,4), WENO-SYMOO-RL (r=3) in capturing different order statistics and non-linear physics in DIT. The quantities are defined in section (3.4.3). We compare the performance of interpolation schemes for different initial turbulent Mach numbers ($M_t = 1.0, 1.38, 1.75$). The following observations can be made from Figs. (3.17)–(3.28):

1. All interpolation schemes perform almost equally in capturing turbulent kinetic energy, solenoidal dissipation (ϵ_s), pressure dilatation ($\overline{p'd'}$) and pressure fluctuation ($\overline{p'p'}$). Although a closer look shows VL scheme slightly more dissipative than the rest.

2. Performance is put to real test in capturing higher order quantities involving larger gradients: dilatational dissipation (ϵ_d), total dissipation (ϵ), flatness (F) and skewness (S).

3. VL scheme is significantly more dissipative in capturing higher order quantities. Dilatational dissipation, flatness and skewness of the velocity field are under predicted by 7-10%.

4. Amongst the WENO schemes WENO-JS (r=3) is slightly more dissipative than the rest.

5. The gain in accuracy going from WENO-SYM (r=3) to WENO-SYM (r=4) is not significant for the current simulations. On, the other hand, WENO-SYM (r=4) is almost 20% computationally more expensive compared to WENO-SYM (r=3).

6. WENO-SYMOO (r=3) or WENO-SYMBO (r=3) seems to be best suited for DNS of homogeneous turbulence.

7. As the initial turbulent Mach number is increased, the dissipative nature of VL scheme is more pronounced. At $M_t = 1.75$ VL scheme grossly under predicts dilatational dissipation and Kurtosis.

In high M_t simulations of decaying turbulence, shocklets (regions of high gradients) arise stochastically in the flow while the rest of the velocity field is relatively smooth. VL scheme is very dissipative in regions of large gradients and thus prevents gradient steepening. In Fig. (3.16) we compare the energy spectra at eddy turnover time

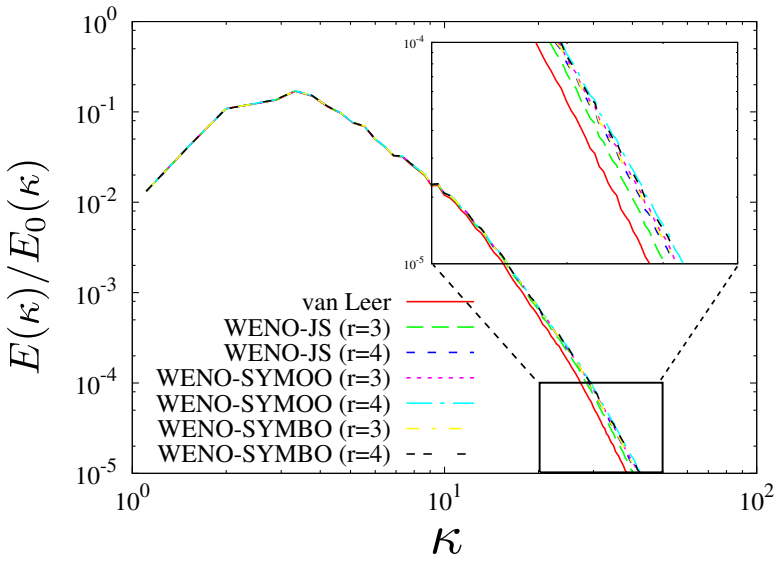

Fig. 3.16. Energy spectra of DHIT ($M_{t_0} = 1.75$ and $Re_{\lambda_0} = 40$ at $t' = 0.15$): comparison of different interpolation schemes - VL, WENO-JS (r=3,4), WENO-SYMOO (r=3,4), WENO-SYMBO (r=3,4).

$t' = 0.15$. The spread (maximum κ) of energy spectra is minimum for the VL scheme indicating a loss of high wavenumber content. Also, for a given wavenumber the peak is smaller in VL case and the difference is more pronounced for larger wavenumbers ($\kappa > 20$).

3.4.6 Effect of temperature vs. energy interpolation

We interpolate temperature (primitive variable) instead of energy (conservative variable) for DIT simulations of initial M_t greater than unity to avoid negative temperature arising around shocklets. Interpolation of primitive variable is associated with adding numerical dissipation to the scheme. In section (3.2.3) we justified the use of temperature interpolation as it helps prevent negative temperatures in high M_t simulations. Here we compare temperature vs. energy interpolation to evaluate

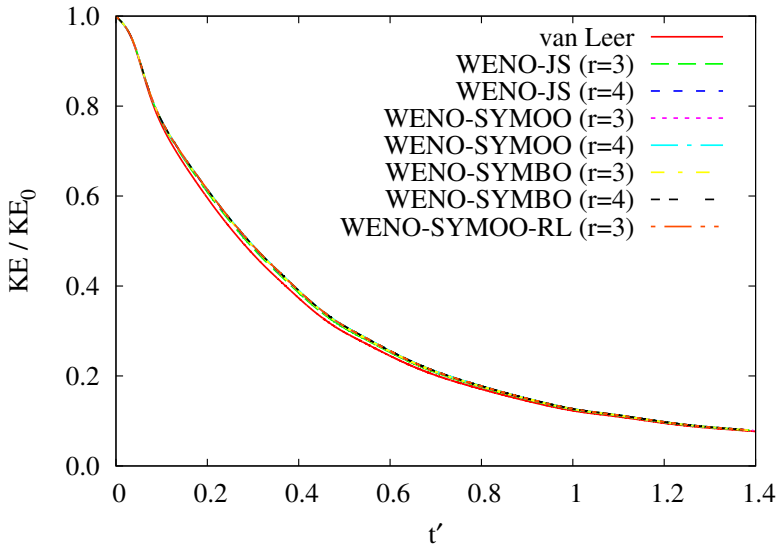

(a)

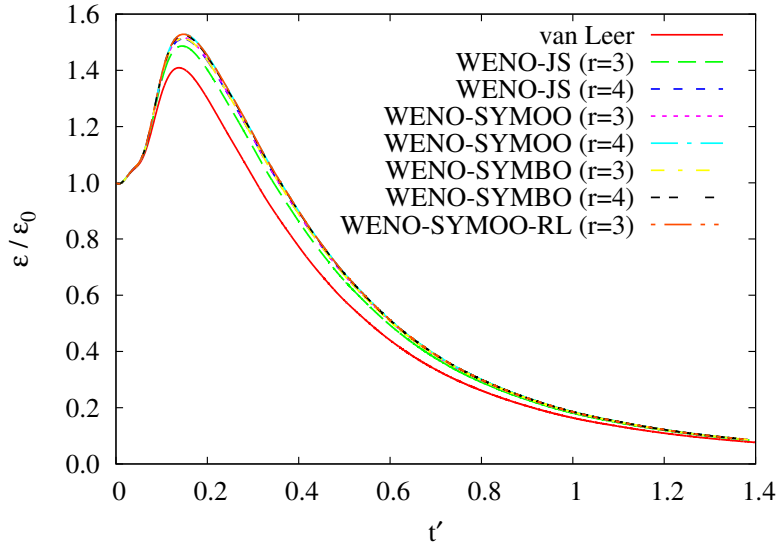

(b)

Fig. 3.17. DNS of decaying isotropic turbulence at $M_t = 1.0$ and $Re_\lambda = 40$: comparison of different interpolation schemes - VL, WENO-JS (r=3,4), WENO-SYMOO (r=3,4), WENO-SYMBO (r=3,4), WENO-SYMOO-RL (r=3) for 128^3 grid (a) turbulent kinetic energy $(k(t)/k_0)$ (b) total dissipation $(\epsilon(t)/\epsilon_0)$.

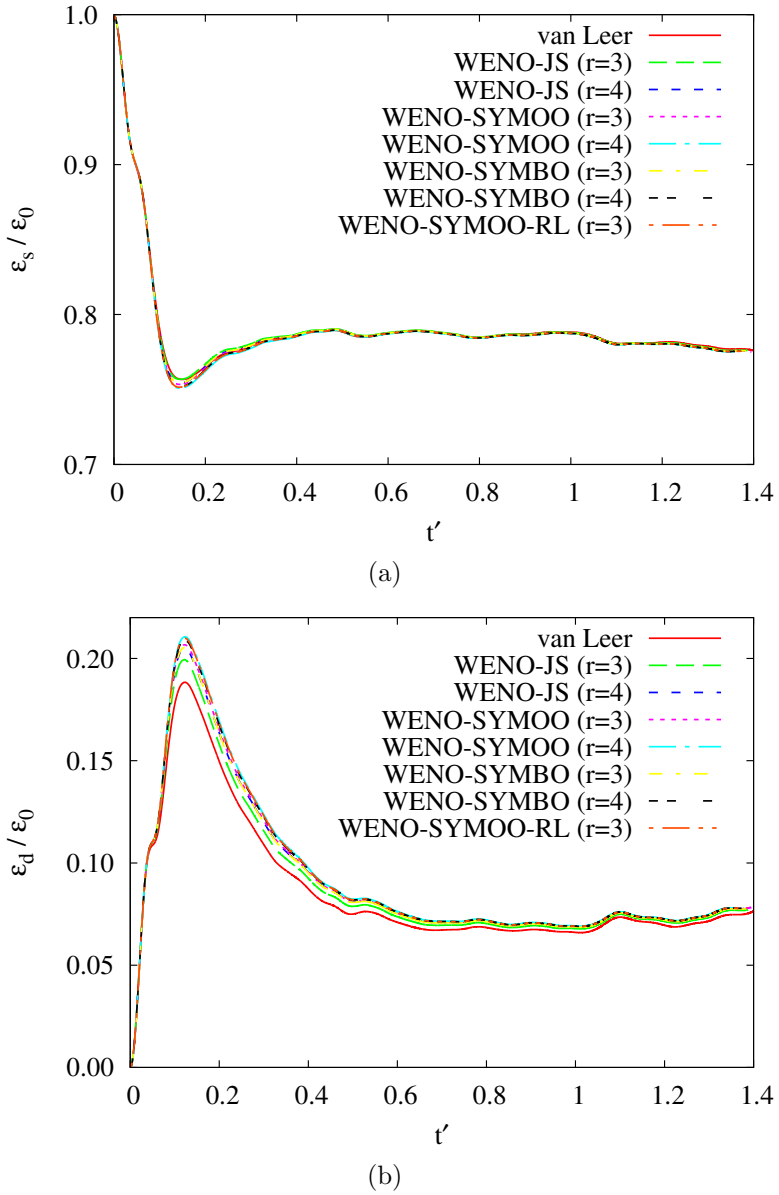

Fig. 3.18. DNS of decaying isotropic turbulence at $M_t = 1.0$ and $Re_\lambda = 40$: comparison of different interpolation schemes - VL, WENO-JS (r=3,4), WENO-SYMOO (r=3,4), WENO-SYMBO (r=3,4), WENO-SYMOO-RL (r=3) for 128^3 grid (a) solenoidal dissipation $(\epsilon_s(t)/\epsilon_0)$ (b) dilatational dissipation $(\epsilon_d(t)/\epsilon_0)$.

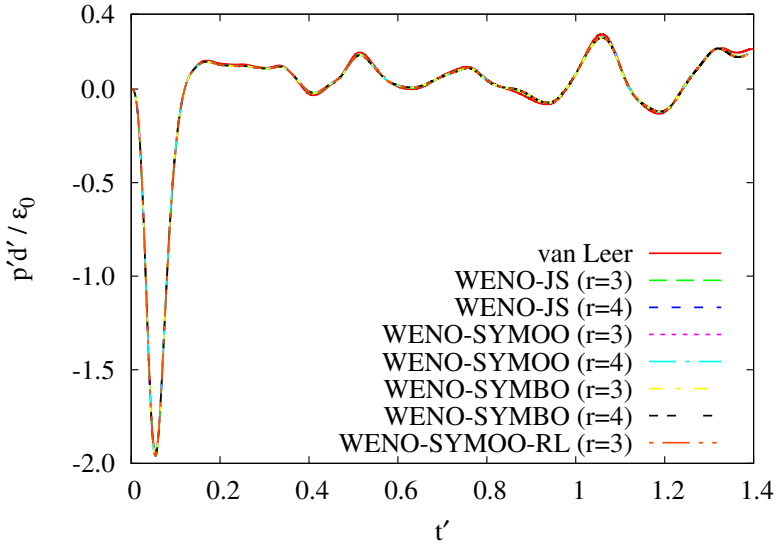

(a)

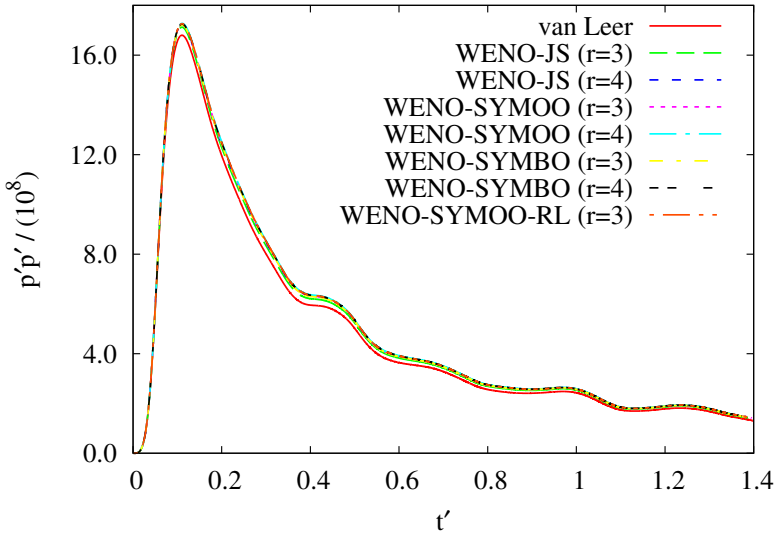

(b)

Fig. 3.19. DNS of decaying isotropic turbulence at $M_t = 1.0$ and $Re_\lambda = 40$: comparison of different interpolation schemes - VL, WENO-JS (r=3,4), WENO-SYMOO (r=3,4), WENO-SYMBO (r=3,4), WENO-SYMOO-RL (r=3) for 128^3 grid (a) pressure dilatation ($p'd'/\epsilon_0$) (b) pressure fluctuation ($p'p'/10^8$).

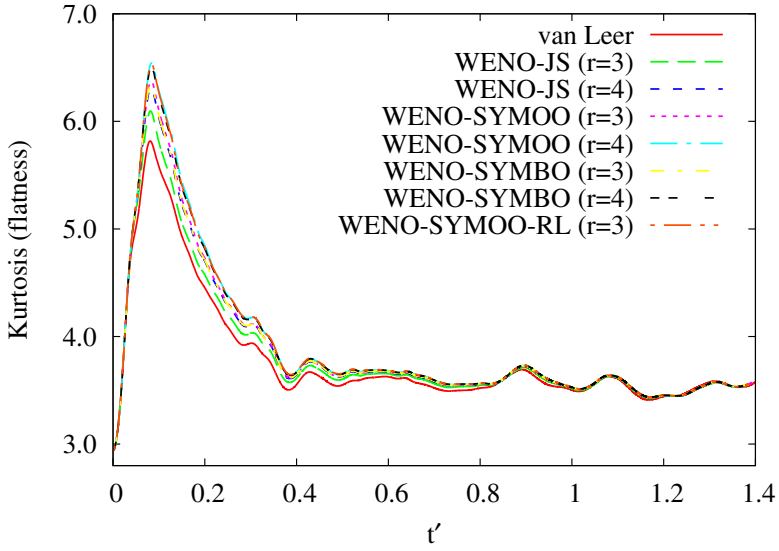

(a)

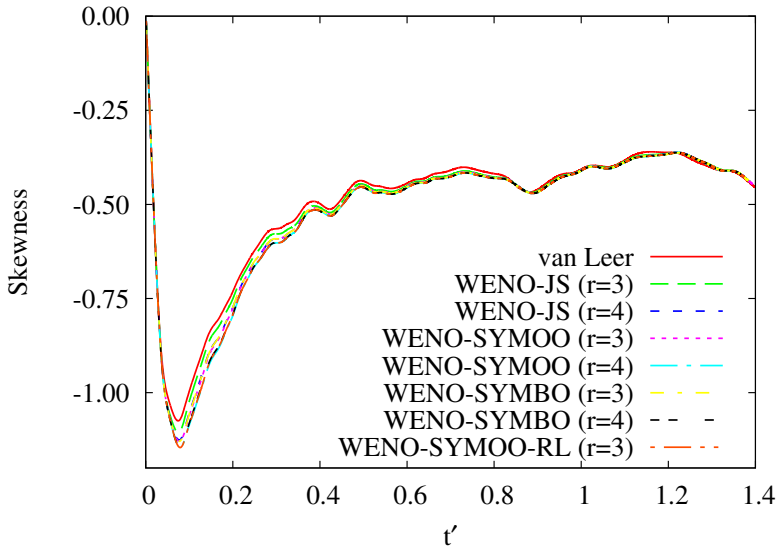

(b)

Fig. 3.20. DNS of decaying isotropic turbulence at $M_t = 1.0$ and $Re_\lambda = 40$: comparison of different interpolation schemes - VL, WENO-JS (r=3,4), WENO-SYMOO (r=3,4), WENO-SYMBO (r=3,4), WENO-SYMOO-RL (r=3) for 128^3 grid (a) Flatness (Kurtosis, F_u) (b) Skewness (S_u).

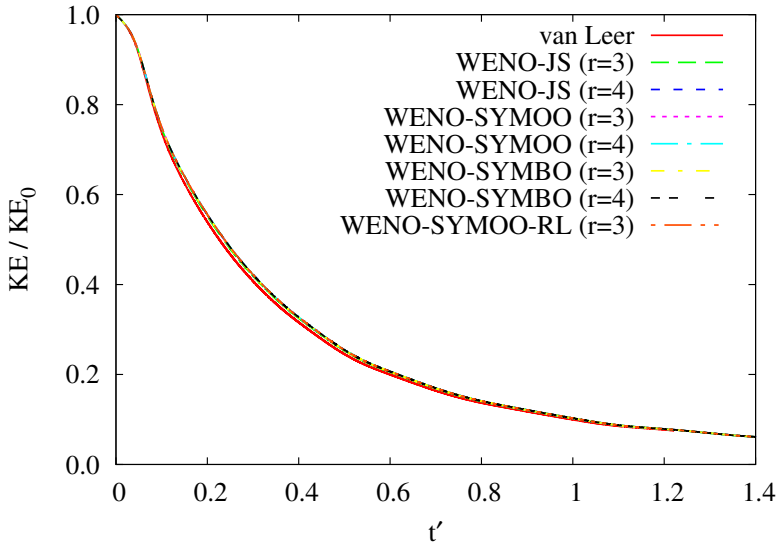

(a)

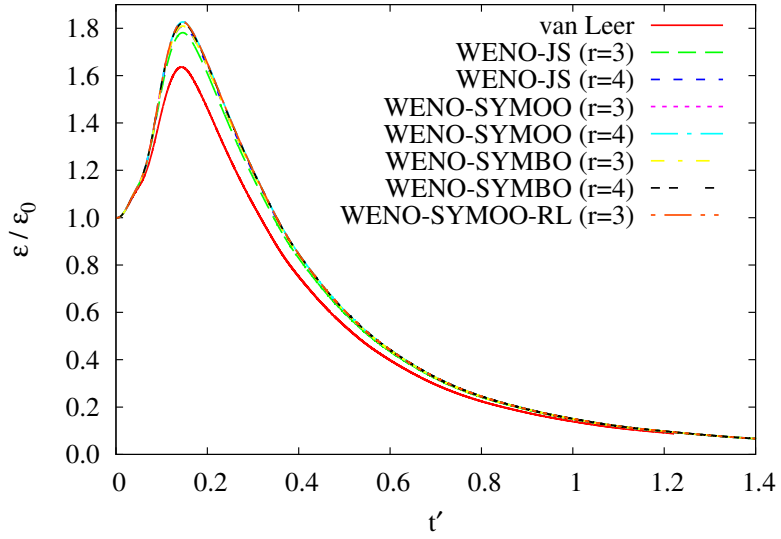

(b)

Fig. 3.21. DNS of decaying isotropic turbulence at $M_t = 1.38$ and $Re_\lambda = 40$: comparison of different interpolation schemes - VL, WENO-JS (r=3,4), WENO-SYMOO (r=3,4), WENO-SYMBO (r=3,4), WENO-SYMOO-RL (r=3) for 128^3 grid (a) turbulent kinetic energy $(k(t)/k_0)$ (b) total dissipation $(\epsilon(t)/\epsilon_0)$.

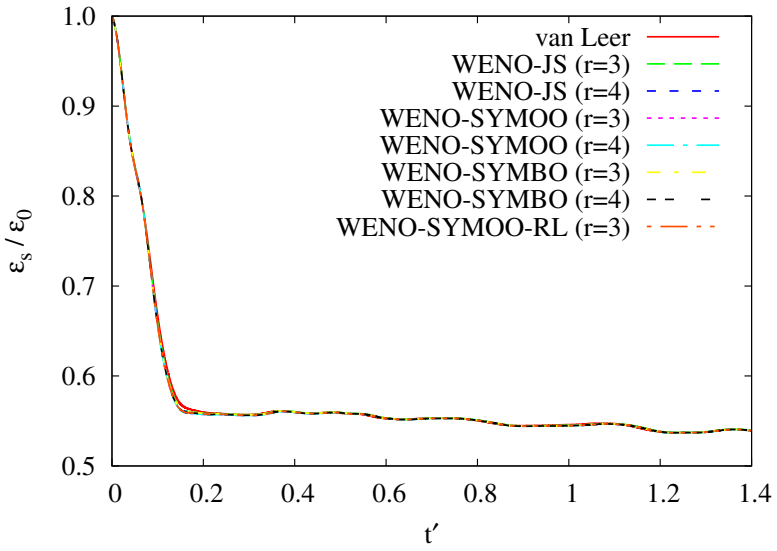

(a)

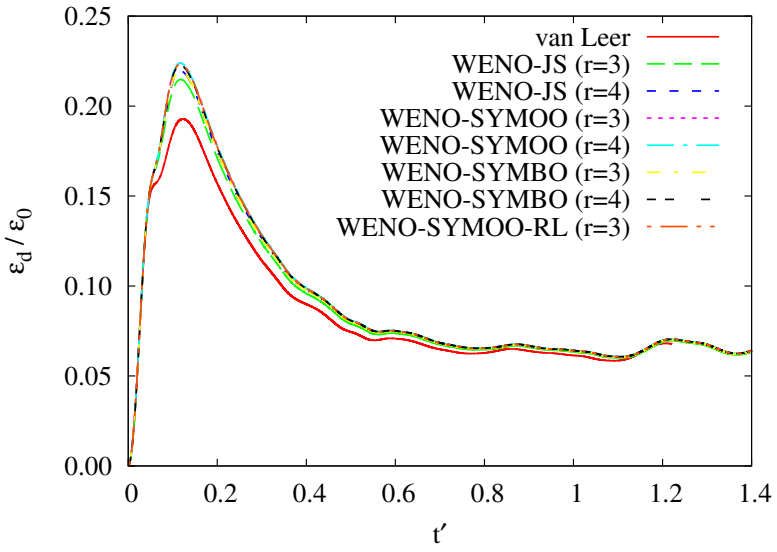

(b)

Fig. 3.22. DNS of decaying isotropic turbulence at $M_t = 1.38$ and $Re_\lambda = 40$: comparison of different interpolation schemes - VL, WENO-JS (r=3,4), WENO-SYMOO (r=3,4), WENO-SYMBO (r=3,4), WENO-SYMOO-RL (r=3) for 128^3 grid (a) solenoidal dissipation ($\epsilon_s(t)/\epsilon_0$) (b) dilatational dissipation ($\epsilon_d(t)/\epsilon_0$).

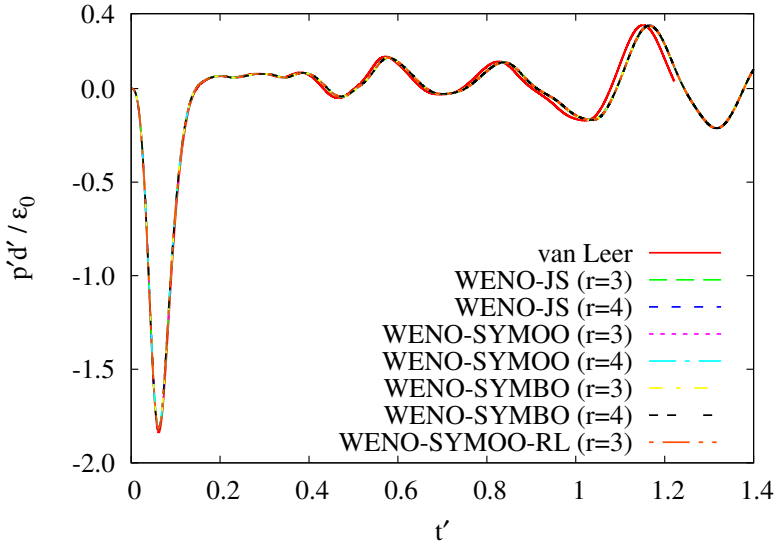

(a)

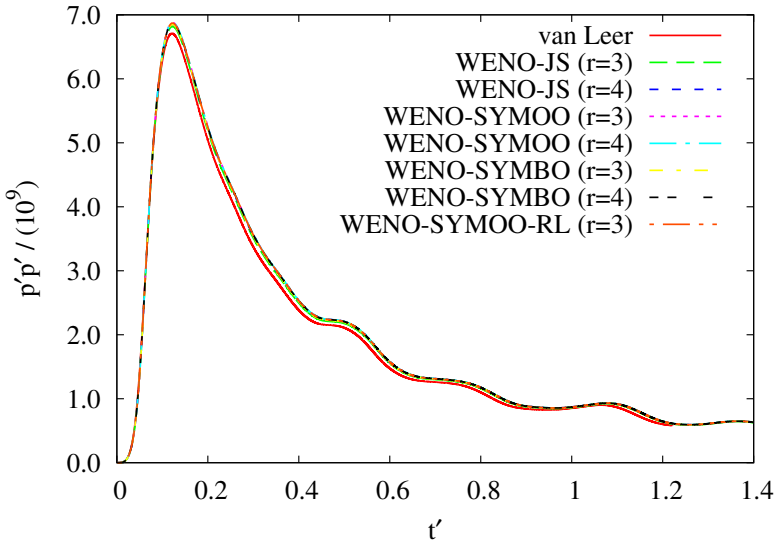

(b)

Fig. 3.23. DNS of decaying isotropic turbulence at $M_t = 1.38$ and $Re_\lambda = 40$: comparison of different interpolation schemes - VL, WENO-JS (r=3,4), WENO-SYMOO (r=3,4), WENO-SYMBO (r=3,4), WENO-SYMOO-RL (r=3) for 128^3 grid (a) pressure dilatation ($p'd'/\epsilon_0$) (b) pressure fluctuation ($p'p'/10^8$).

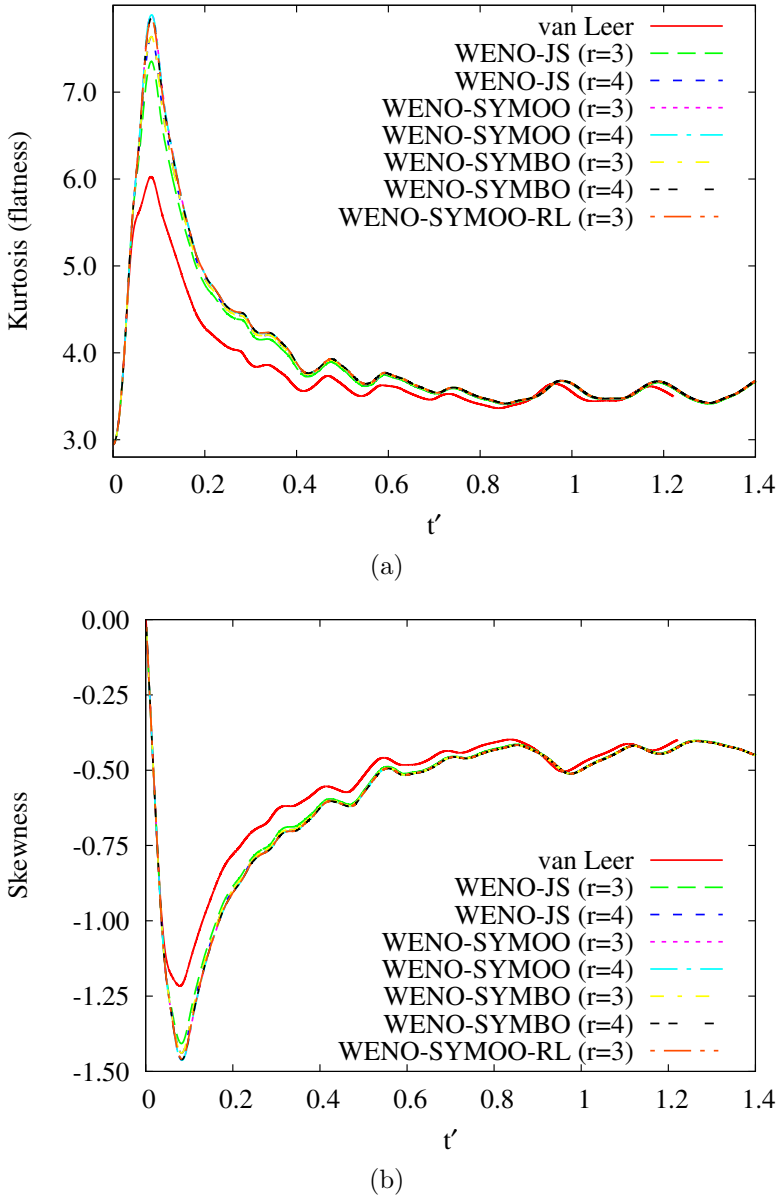

Fig. 3.24. DNS of decaying isotropic turbulence at $M_t = 1.38$ and $Re_\lambda = 40$: comparison of different interpolation schemes - VL, WENO-JS (r=3,4), WENO-SYMOO (r=3,4), WENO-SYMBO (r=3,4), WENO-SYMOO-RL (r=3) for 128^3 grid (a) Flatness (Kurtosis, F_u) (b) Skewness (S_u).

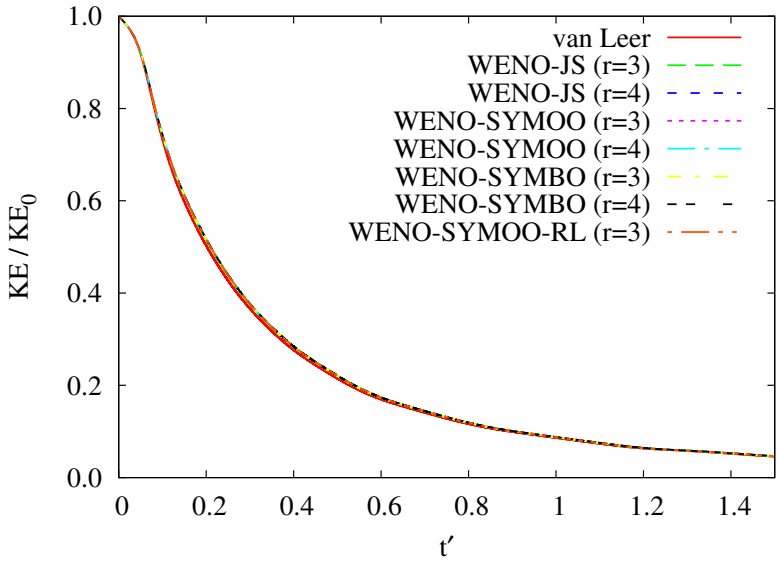

(a)

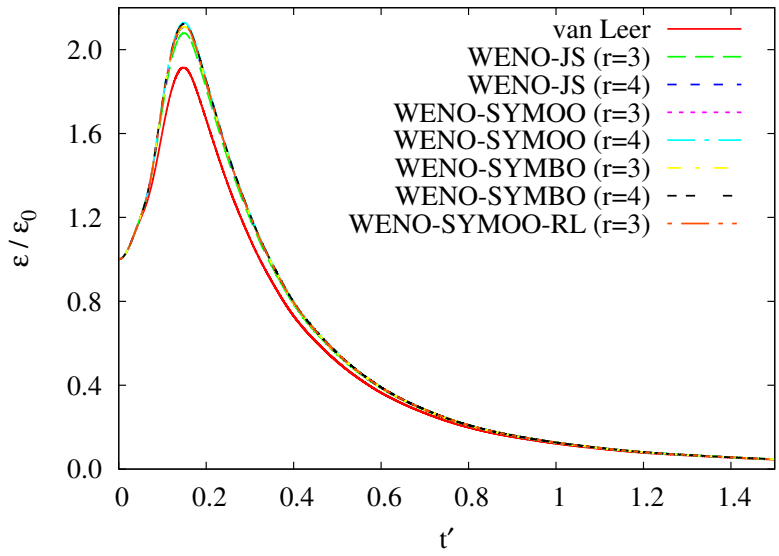

(b)

Fig. 3.25. DNS of decaying isotropic turbulence at $M_t = 1.75$ and $Re_\lambda = 40$: comparison of different interpolation schemes - VL, WENO-JS (r=3,4), WENO-SYMOO (r=3,4), WENO-SYMBO (r=3,4), WENO-SYMOO-RL (r=3) for 128^3 grid (a) turbulent kinetic energy $(k(t)/k_0)$ (b) total dissipation $(\epsilon(t)/\epsilon_0)$.

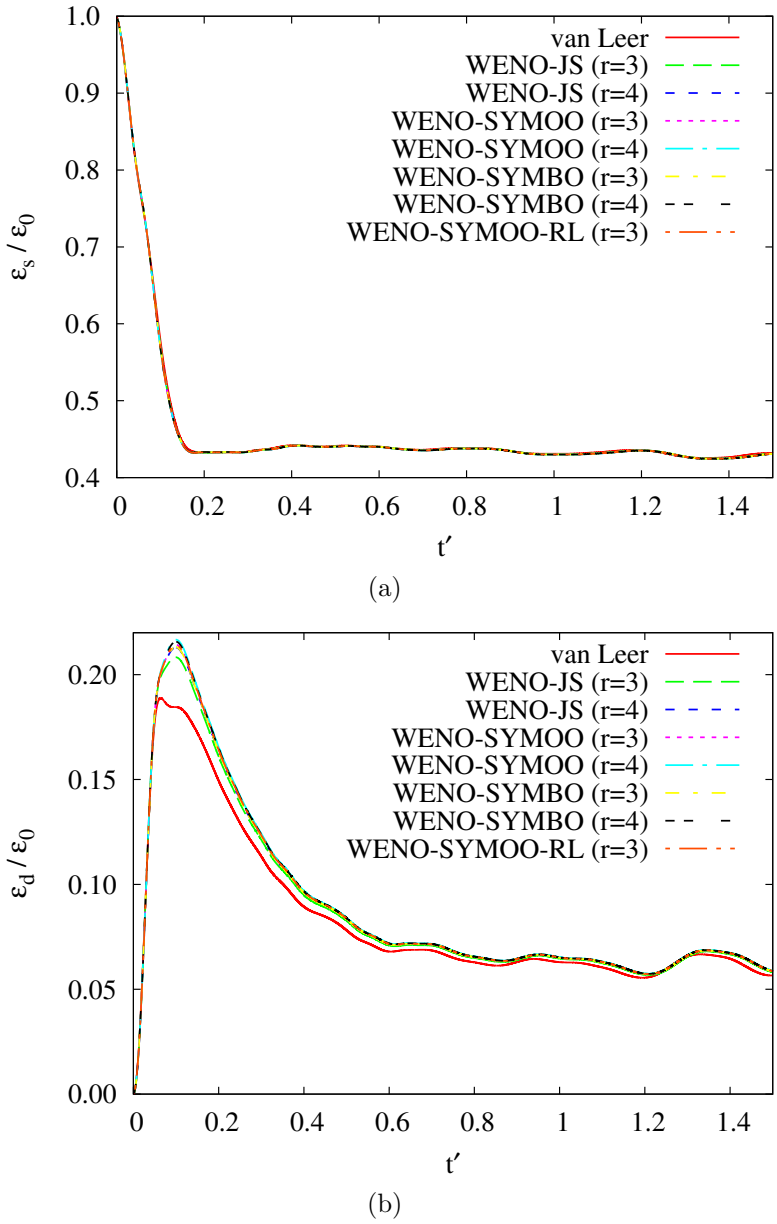

Fig. 3.26. DNS of decaying isotropic turbulence at $M_t = 1.75$ and $Re_\lambda = 40$: comparison of different interpolation schemes - VL, WENO-JS (r=3,4), WENO-SYMOO (r=3,4), WENO-SYMBO (r=3,4), WENO-SYMOO-RL (r=3) for 128^3 grid (a) solenoidal dissipation $(\epsilon_s(t)/\epsilon_0)$ (b) dilatational dissipation $(\epsilon_d(t)/\epsilon_0)$.

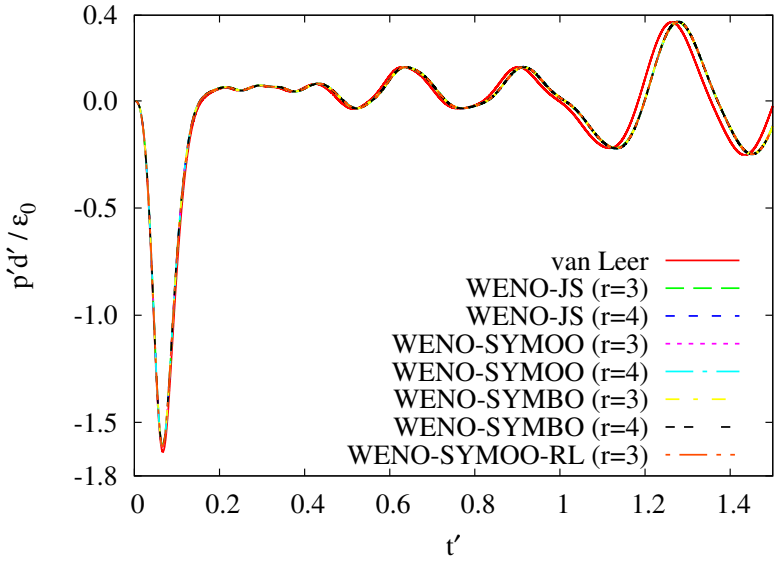

(a)

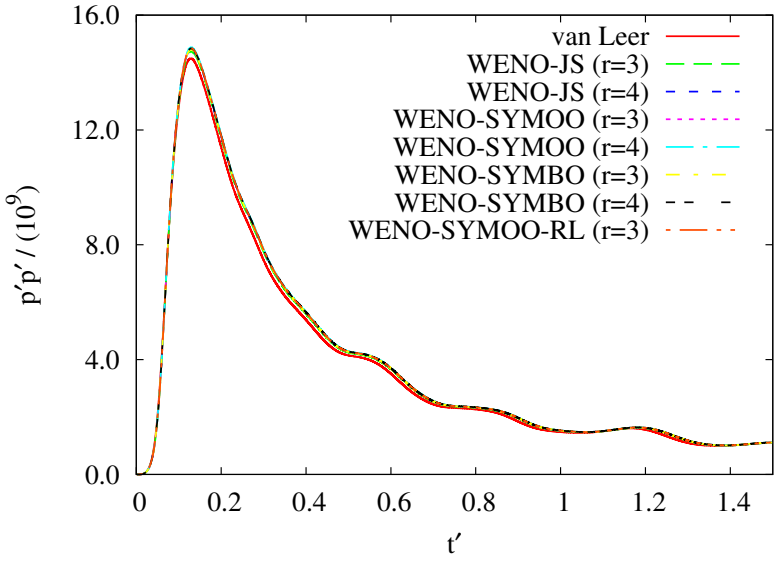

(b)

Fig. 3.27. DNS of decaying isotropic turbulence at $M_t = 1.75$ and $Re_\lambda = 40$: comparison of different interpolation schemes - VL, WENO-JS (r=3,4), WENO-SYMOO (r=3,4), WENO-SYMBO (r=3,4), WENO-SYMOO-RL (r=3) for 128^3 grid (a) pressure dilatation ($p'd'/\epsilon_0$) (b) pressure fluctuation ($p'p'/10^9$).

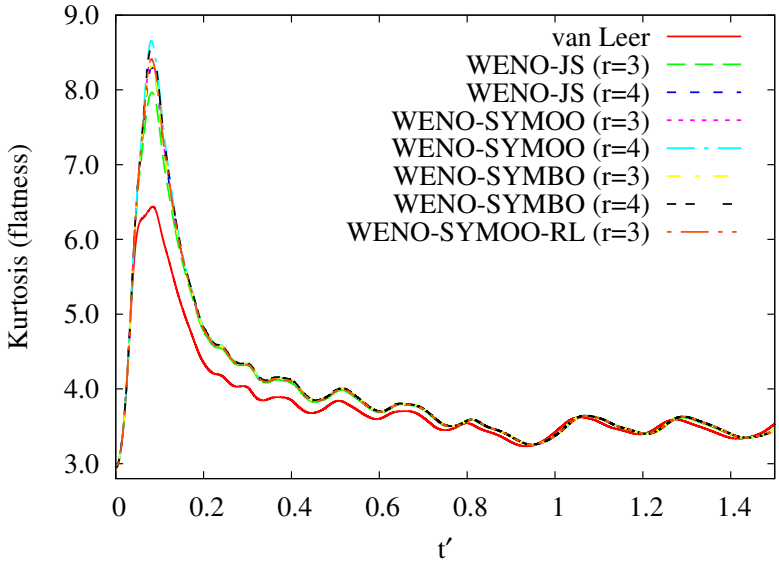

(a)

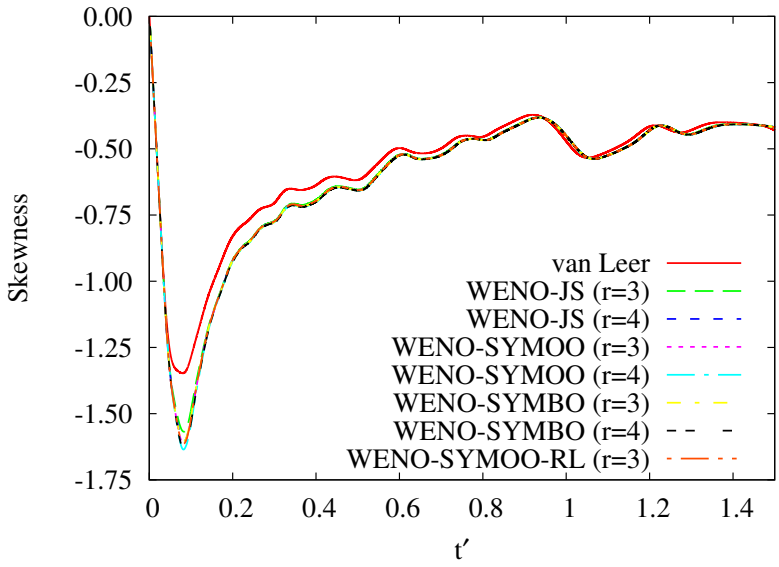

(b)

Fig. 3.28. DNS of decaying isotropic turbulence at $M_t = 1.75$ and $Re_\lambda = 40$: comparison of different interpolation schemes - VL, WENO-JS (r=3,4), WENO-SYMOO (r=3,4), WENO-SYMBO (r=3,4), WENO-SYMOO-RL (r=3) for 128^3 grid (a) Flatness (Kurtosis, F_u) (b) Skewness (S_u).

the increase in numerical dissipation due to the interploation of primitive variable (T). The rest of the interpolated variables are conservative.

Figures 3.29 and 3.30 compares evolution of kinetic energy, dissipation, flatness and skewness with time for $M_t = 1.0$ and $Re_\lambda = 70$ obtained using temperature and energy interpolation. In Figs. 3.29 and 3.30 VL limiter and WENO-SYMOO (r=3) have been used, respectively. There is negligible difference in results between temperature and energy interpolations in both cases. A closer look at Fig. 3.29 (VL case) shows temperature interpolation to be slightly more dissipative compared to energy interpolation. With WENO-JS and WENO-SYM as the interpolation schemes, the difference is even smaller.

3.4.7 Code efficiency study

Direct simulations of DIT is severely constrained by high computational costs. High order interpolation schemes use a significant amount of the computational time. We study the efficiency (in terms of computational time) of the different reconstruction schemes used in our GKM study. The following table shows time taken in GKM computation on a 128^3 grid for various reconstruction schemes. We run the parallelized code on IBM iDataplex High Performance Cluster (Texas A&M University) utilizing 512 processors (8 in each direction) and tabulate 'wall time' taken for 35000 iterations.

From table (3.1) we see that VL scheme is the least computationally intensive reconstruction scheme. WENO-SYMOO (r=3) takes 20% more time compared to VL while WENO-SYM (r=4) takes 36 % more time. Compared to WENO-SYMOO (r=3), WENO-SYMOO (r=4) is a negligible improvement (in terms of numerical accuracy on a 128^3 grid in the range of cases discussed) but computational cost is 13% higher. Considering the improvement in terms of accuracy and dissipative nature of WENO-SYMOO (r=3) over VL, the benefits outweighs the 20% difference

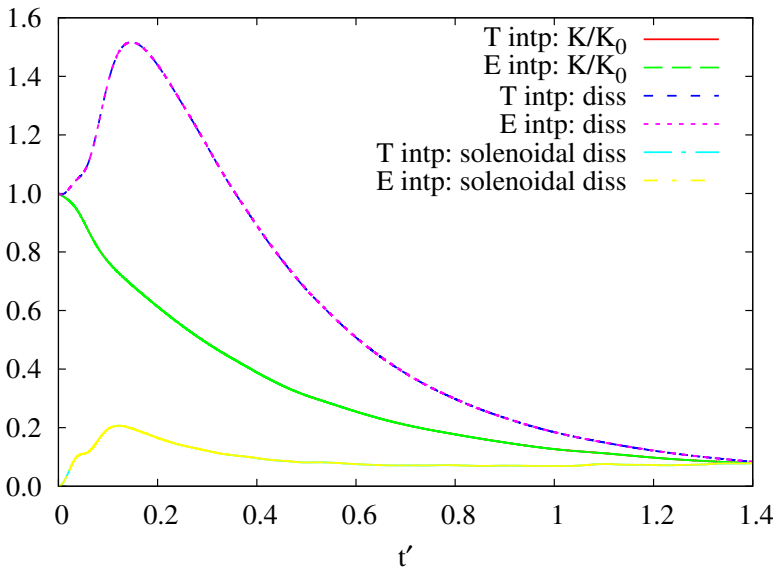

(a)

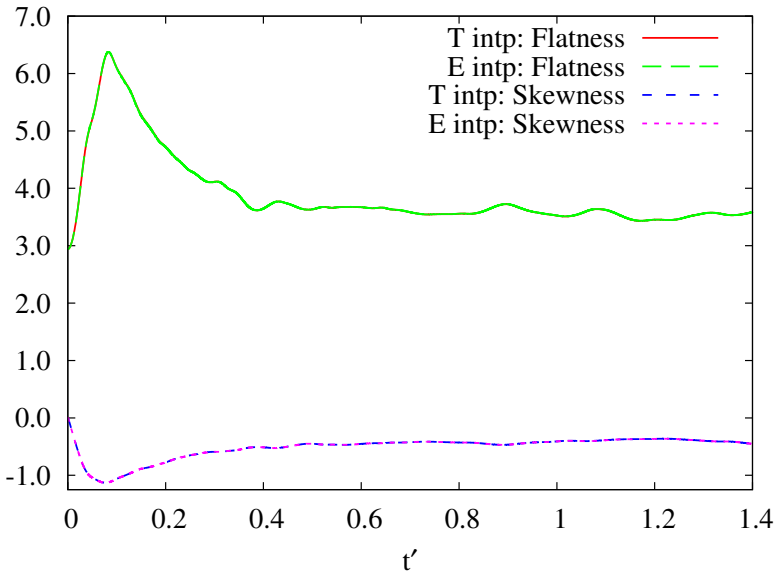

(b)

Fig. 3.29. DNS of decaying isotropic turbulence at $M_t = 1.0$ and $Re_\lambda = 40$: comparison of temperature and Energy interpolation using VL (a) turbulent kinetic energy and dissipation (b) Flatness and Skewness.

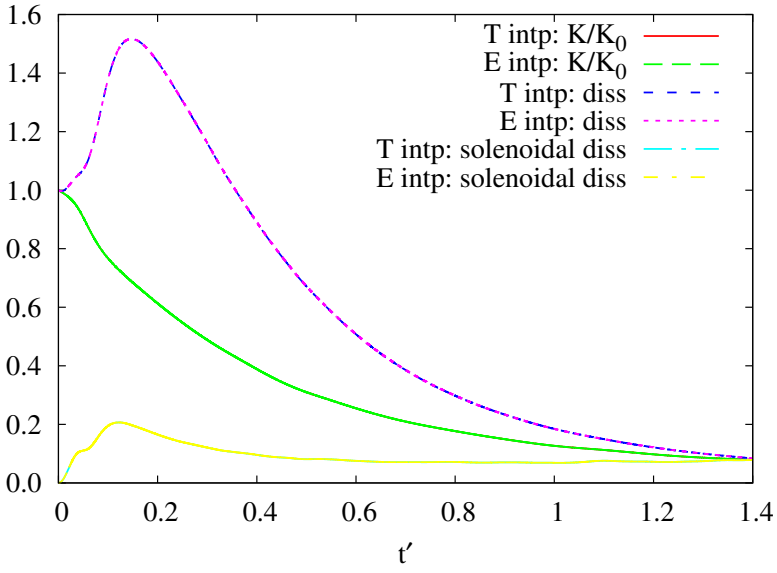

(a)

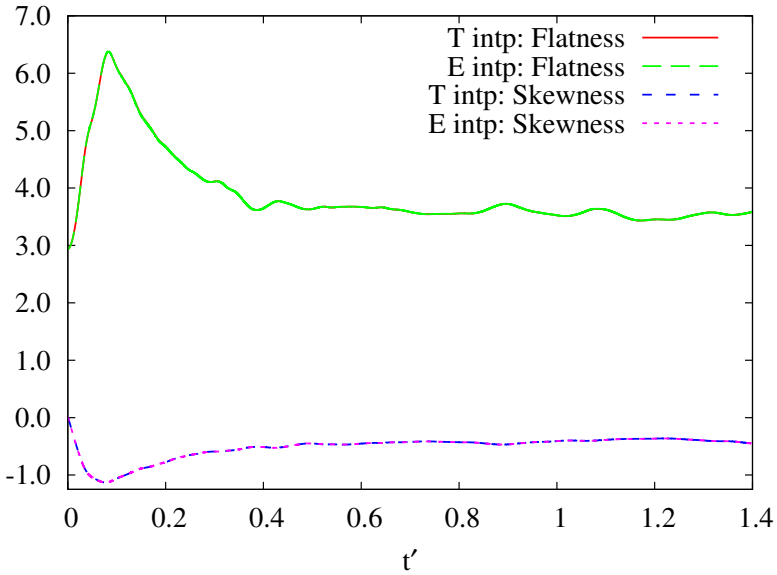

(b)

Fig. 3.30. DNS of decaying isotropic turbulence at $M_t = 1.0$ and $Re_\lambda = 40$: comparison of temperature and Energy interpolation using WENO-SYMOO (r=3) (a) turbulent kinetic energy and dissipation (b) Flatness and Skewness.

Scheme	iterations	processors	wall time
VL	35000	512	1042.256
WENO-Shu (r=3)	35000	512	1237.123
WENO-Shu (r=4)	35000	512	1321.578
WENO-SYMBO (r=3)	35000	512	1252.638
WENO-SYMBO (r=4)	35000	512	1415.713
WENO-SYMOO (r=3)	35000	512	1254.009
WENO-SYMOO (r=4)	35000	512	1417.449
WENO-SYMOO-RL (r=3)	35000	512	1282.478

Table 3.1
Code efficiency study: time taken in computation by GKM code for a 128^3 grid using different interpolation schemes - VL, WENO-JS (r=3,4), WENO-SYMOO (r=3,4), WENO-SYMBO (r=3,4), WENO-SYMOO-RL (r=3)

in computational time. Therefore we recommend WENO-SYM (r=3) for DNS of DIT for its accuracy, robustness and computational cost.

3.5 Conclusions

Gas Kinetic Method is increasingly becoming a popular choice for computing compressible flows. We apply GKM towards direct numerical simulations of compressible transition and turbulence. Direct simulations of highly compressible turbulence is more challenging than its incompressible counterpart due to strong spatio-temporal gradients which manifest as random shocklets in the flow. The presence of shocklets imposes severe restrictions on the choice of reconstruction schemes. The reconstruction scheme must be high order accurate in smooth regions while capturing steep gradients across shocks without adding significant dissipation. The problem of negative temperatures arising due to the Gibbs phenomenon across shocklets corrupts

DNS of compressible flows and restricts high turbulent and gradient Mach number simulations.

The objective of the study is to enhance GKM for direct simulations of high Mach number transition and turbulence. We examine several WENO-based advanced reconstruction schemes alongside well-known van Leer (VL) scheme. We perform comparative studies for evaluating numerical accuracy and robustness of various schemes. Our goal to study how different schemes perform in capturing linear and non-linear physics of compressible flows.

The conclusions for this study are summarized below:

1. Though GKM with WENO-based reconstruction is $20-30\%$ more computationally expensive than VL, improvement in terms of accuracy and numerical dissipation outweighs the difference in computational time. Amongst the WENO-based schemes, the class of WENO-SYM [65,66] are more accurate and robust than WENO-JS [64]. The symmetric stencil and improved non-linear weights in WENO-SYM are desirable for accuracy in DNS and their robustness is at par with WENO-JS. Amongst the WENO-SYM class of schemes, WENO-SYMOO-RL (relative limiter) [66] is least dissipative but is robust than WENO-SYMOO. A robust interpolation scheme is critical to highly compressible DIT simulation for avoiding negative temperatures arising out of undershoots around shocks. Typically, dissipative nature increases the robustness of interpolation schemes. We find WENO-based schemes to be more robust than VL despite being significantly less dissipative.

2. We perform detailed validation studies to determine accuracy and robustness of interpolation schemes in capturing solenoidal statistics, dilatational statistics, linear physics and non-linear physics. With transition and turbulence applications in mind we perform DNS for two relevant canonical flow fields: homogeneous shear and decaying isotropic turbulence. In decaying turbulence, simulations start with an isotropic velocity field made up of a collection of

Fourier waves (modes) with only lower wavenumbers energized. In contrast, for homogeneous shear flows we look at the evolution of individual Fourier waves.

(a) We examine interpolation schemes for their accuracy in capturing solenoidal (vortical) and dilatational (acoustic) portion of the velocity field individually (homogeneous shear) and collectively (DIT). We observe a key difference between the VL and WENO-based interpolation schemes in capturing solenoidal and dilatational statistics. VL performs as well as WENO-based schemes in capturing the solenoidal statistics. Since solenoidal behavior is associated with milder gradients, the dissipative nature of VL is not prominent. The difference between VL and WENO arises while computing dilatational statistics. The dilatational statistics are associated with steep gradients and often strong shocklets. Since VL reduces to first order across shocklets, it adds significantly larger dissipation compared to WENO-based interpolation. We compare the accuracy of schemes in capturing solenoidal and dilatational behavior in DIT by comparing solenoidal and dilatational dissipation, respectively. The dissipative nature of VL manifests as decreased peaks of statistics strongly related to the dilatational behavior. In homogeneous shear case with the 'dilatational' wave, dissipative nature of VL gives rise to under-prediction of turbulent kinetic energy at late 'shear time'.

(b) For validation of linear physical processes, we compare high gradient Mach number homogeneous shear DNS against Rapid Distortion Theory (RDT) and Burgers limit (3.19). Simulations with VL and WENO-SYMOO, both, follow the Burgers limit up to shear time $St \approx 2$ and so does the result from linear theory–RDT. For $St > 2$, DNS and RDT kinetic energy deviates from the Burgers evolution due to the action of pressure. Results from DNS and linear theory match closely till $St \approx 10$. For $St > 10$,

non-linear effects and viscosity are significant, and DNS shows significant departure from RDT. The WENO scheme is much closer to RDT than VL.

(c) For validation of non-linear physical processes we compare results against a simulation with very high spatial resolution. We use 512^3 grid as the 'gold standard' simulation for DIT. Turbulence statistics in non-linear regime is highly affected by shocks and steep gradients which have a significant contribution towards dissipation of kinetic energy and pressure dilatation. Capturing shocklets and steep gradients accurately, is key in capturing non-linear physics in DIT. By comparing against the 'gold standard' simulation, we conclude that WENO-based schemes can adequately capture turbulence statistics in DIT ($M_t = 1.2, Re_\lambda = 46$) with a reasonably coarser 128^3 grid.

3. Despite using highly robust WENO-based schemes, we frequently encounter negative temperature in DIT simulations. With total-energy E as the interpolated thermodynamic variable, the highest turbulent Mach number successfully simulated without negative temperatures is around unity. The problem is exacerbated as we move to higher turbulent Mach numbers. We propose interpolating temperature T instead of total-energy E for avoiding negative temperatures. A consistent interpolation of temperature is critical beacuse temperature is used explicitly in the GKM formulation. We also show that the accuracy of the solution is not degraded due to temperature interpolation and is minimal if higher order interpolation is used.

4. STABILIZING ACTION OF PRESSURE IN HIGHSPEED COMPRESSIBLE SHEAR FLOWS

4.1 Introduction

Compressibility exerts a strong and complex influence on turbulence and transition in high-speed shear flows. In turbulent mixing layers, it is well established that compressibility leads to reduced mixing [89–94]. Several investigations have been performed to explain the physical mechanism of reduced mixing with increasing Mach number. Sarkar [9] performed direct numerical simulations (DNS) of homogeneous shear turbulence at high Mach numbers and showed that pressure plays a pivotal role in stabilizing high speed flows. Indeed, modifying the pressure-strain correlation closure would be the physically consistent approach to achieve the observed mixing reduction in model calculations. Simone *et al.* [10], further demonstrate that the linear rapid distortion theory (RDT) calculations of high Mach number homogeneous turbulence also capture the stabilizing effect of compressibility and provide further insight into the mechanism. Lavin *et al.* [13, 78, 95] perform further RDT investigations and clearly exhibit the existence of three stages of perturbation evolution in homogeneous shear flows. These stages correspond to the different shear-to-acoustic timescale ratios and correspondingly different action of pressure. When the shear-to-acoustic timescale ratio is of order unity, there is strong harmonic-oscillator type coupling between dilatational velocity and pressure perturbations which ultimately leads to decreased levels of kinetic energy growth.

One of the prominent features of compressibility is its stabilizing effect on growth of turbulence. In experiments of high speed mixing layers, the normalized spreading rate (normalized by incompressible spreading rate) decreases with increasing relative Mach number. In Fig. (4.1), normalized spreading rate is compiled from different experiments along with the so-called Langely curve [7]. At low relative Mach numbers, the spreading rates are similar to incompressible values but decreases significantly

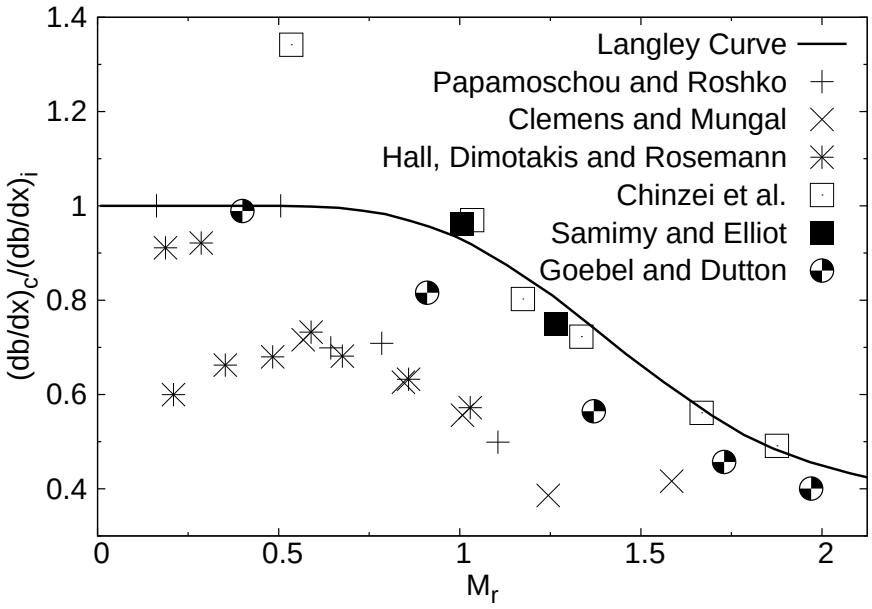

Fig. 4.1. Normalized mixing layer spreading rate in compressible flows.

with increasing relative Mach number. A similar stabilizing effect has also been observed in experiments of high speed transition layers. In hypersonic boundary layers, the transition zone is longer compared to incompressible. An increasing compressibility effect, decreases the normalized growth rate of turbulence thereby increasing the length of transition zone.

In hypersonic boundary layers, compressibility effects manifest in a prolonged transition zone [96–99] featuring strong velocity-pressure interactions. However, the extent of the transition region is strongly dependent on the type of perturbation modes introduced into the flow. Lavin *et al.* [78, 95] and Bertsch [100] propose that the pressure mechanism responsible for turbulence stabilization in mixing layers is also the fundamental cause of the prolonged transition zone. Depending upon the type and orientation of the perturbation mode, the duration of the prolongation can be reduced or enhanced. Hence, there is a strong motivation for understanding the effect of compressibility on individual perturbation/fluctuation modes as well as

statistical behavior of a collection of modes in shear flows. Several preceding studies [9,10,13,95] have established that the stabilizing mechanism in various shear flows is embodied in homogeneous shear flow. Furthermore, a comprehensive understanding of complex compressible shear flows must begin with the simplest form of such flows: homogeneously sheared turbulence.

4.1.1 Background

In RDT simulations of compressible homogeneous shear, Lavin *et. al* [78, 95] find that the evolution of kinetic energy exhibits three distinct stages/phases characterized by role of pressure. They quantify shear rate of various strengths by initial gradient Mach number M_{g0}. The three distinct stages of growth shown in Fig (4.2) in shear, mixed and acoustic time-scales are: (i) pressure-released (PR) stage $[St < \sqrt{M_{g0}}]$ where pressure effects are negligible and growth rate is like Burgers; (ii) wave-character (WC) stage $[\sqrt{M_{g0}} < St < \sqrt{M_{g0}}]$ where the wave/acoustic nature of pressure is evident and growth rate slows down to a plateau; and (iii) Low-Mach (LM) stage $[St > M_{g0}]$ where growth is like an incompressible field. Bertsch [100] and Bertsch *et. al* [101] further confirm the findings of [78, 95] in the framework of Favre averaged RDT and study the role of pressure in the three stages of evolution of kinetic energy in detail. These works demonstrate that in the second-stage (wave-character stage), pressure works to nullify production of Reynolds shear stresses. This leads to vanishing shear stresses and, in turn, to nearly zero or even a negative production. In the third-stage, pressure plays a role similar to that in incompressible RDT. However, role played by pressure in bringing about the three stage behavior and its effect on individual perturbation/fluctuation modes is not understood.

Mishra and Girimaji [102, 103] study the evolution of different Fourier modes in incompressible homogeneous shear flows in the framework of RDT dynamical system of equations. They find that only a few mode grow while the rest decay very rapidly. They demonstrate how a modal analysis of flow stability and pressure-action can lead

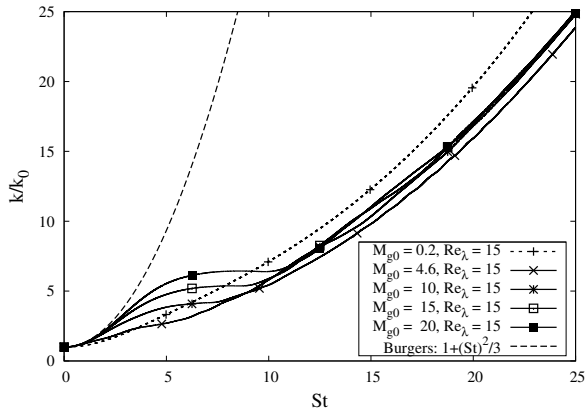

(a)

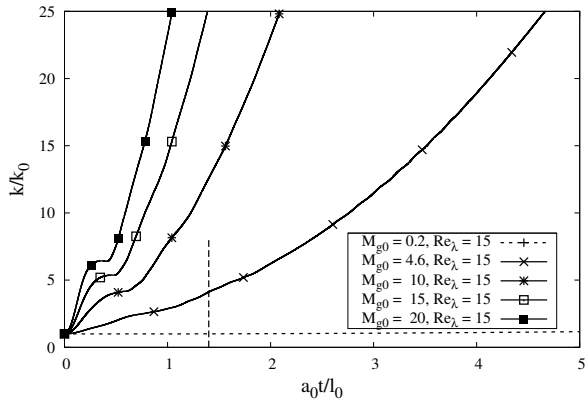

(b)

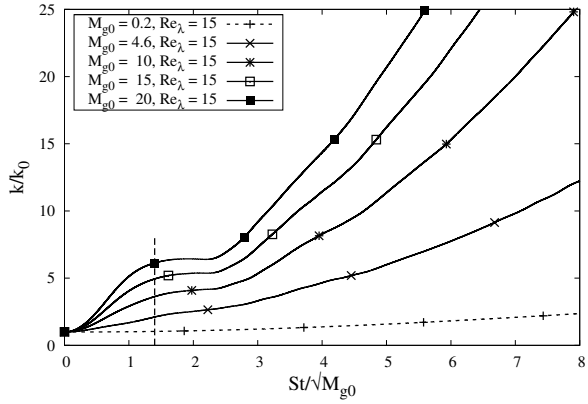

(c)

Fig. 4.2. Evolution of normalized kinetic energy (k/k_0) for collective behavior in shear flows in: a)shear time, b) acoustic time, c) mixed time.

to improved turbulence models in incompressible flows. In compressible flows, this type of modal analysis can be expected to have an even more significant impact as the mode-dependent action of pressure holds the key to understanding and modeling compressibility effects.

The objective of the present work is to perform DNS and linear analysis of individual and collective behavior of various perturbation/fluctuation modes in homogeneous shear turbulence. Specifically, we seek the following:

1. Characterize the modal behavior of thermodynamic pressure as a function of gradient Mach number (M_g) and obliqueness/orientation of mode (β).

2. Contrast the velocity perturbation evolution: pressure-less, Poission pressure and thermodynamic pressure.

3. Demarcate stable and unstable modes as a function of M_g and β.

4. Propose a more complete explanation of the collective compressibility effect on transition/turbulence behavior and explain the modal mechanism underlying the three-staged growth of kinetic energy.

4.2 Governing Equations and Numerical Approach

We perform DNS for studying the evolution of turbulent fluctuations in homogeneous shear. We compare results against inviscid Burgers (pressure-released limit) which is essentially the Navier-Stokes equation without the pressure and viscous terms. The results are also compared against RDT [76–78], a linear theory valid for initial times in turbulence when the effects of non-linearities are negligible. In this section we summarize the governing equations for full Navier-Stokes, RDT and Burgers analysis.

Full compressible ideal-gas Navier-Stokes equations

The compressible, ideal-gas Navier-Stokes equations governing the flow of interest in this study are:

$$\frac{\partial \rho}{\partial t} + \frac{\partial (\rho u_i)}{\partial x_i} = 0, \tag{4.1}$$

$$\frac{\partial (\rho u_i)}{\partial t} + \frac{\partial (\rho u_i u_j + p\delta_{ij})}{\partial x_j} = \frac{\partial \sigma_{ij}}{\partial x_j}, \tag{4.2}$$

$$\frac{\partial E}{\partial t} + \frac{\partial [(E+p)u_i]}{\partial x_i} = \frac{\partial (\sigma_{ij} u_j)}{\partial x_i} - \frac{\partial}{\partial x_i}\left(\kappa_t \frac{\partial T}{\partial x_i}\right). \tag{4.3}$$

The viscous stress tensor σ_{ij} is given by a constitutive relation

$$\sigma_{ij} = \mu \left[\frac{\partial u_i}{\partial x_j} + \frac{\partial u_j}{\partial x_i} + \lambda \delta_{ij} \frac{\partial u_k}{\partial x_k}\right], \tag{4.4}$$

and the thermodynamic pressure p is given by the ideal gas law

$$p = \rho R T. \tag{4.5}$$

Here, μ is the coefficient of dynamic viscosity, κ_t is the thermal conductivity, $\lambda = -(2/3)\mu$ is the second viscosity coefficient and R is the gas constant.

RDT equations

We compare results from DNS against linear RDT [13, 104]. The RDT equations in spectral space [95] are given by:

$$\frac{d\widehat{\rho'}}{dt} = -i\bar{\rho}\widehat{u'_j}\kappa_j, \tag{4.6}$$

$$\frac{d\widehat{u'_i}}{dt} = -\frac{i}{\bar{\rho}}\widehat{p'}\kappa_i - \widehat{u'_j}S_{ij}, \tag{4.7}$$

$$\frac{d\widehat{p'}}{dt} = -i\gamma\bar{p}\widehat{u'_j}\kappa_j, \tag{4.8}$$

where $i = \sqrt{-1}$ is the unit imaginary number, $\bar{(\cdot)}$ represent mean flow variables and $\hat{(\cdot)}$ represent the Fourier amplitude. The evolution equation for the wave vector κ_i is

$$\frac{\partial \kappa_i}{\partial t} + \bar{u}_j \frac{\partial \kappa_i}{\partial x_j} = -\kappa_i \frac{\partial \bar{U}_j}{\partial x_j}. \tag{4.9}$$

Pressure-released equations

The linearized Burgers equation has no non-linear, viscous and pressure effects. The 'pressure-released' limit is the solution to the inviscid Burgers equation given by

$$\frac{\partial u_i}{\partial t} + u_j \frac{\partial u_i}{\partial x_j} = 0. \tag{4.10}$$

An analytical solution to the Burgers equation for an isotropically distributed collection of modes is given by

$$\frac{K(t)}{K_0} = 1 + \frac{(St)^2}{3}. \tag{4.11}$$

The growth of kinetic energy for individual modes is given as

$$\frac{K(t)}{K_0} = 1 - \frac{\overline{u_1 u_3(0)}}{K_0} St + \frac{\overline{u_3 u_3(0)}}{K_0} (St)^2. \tag{4.12}$$

Kinetic energy equations

The evolution equation for turbulent kinetic energy in homogeneous shear flows can be derived by Favre averaging [79, 80] the instantaneous momentum equation (5.2.1) and is given as

$$\frac{dK}{dt} = P - \epsilon_s - \epsilon_c + \frac{\overline{p'd'}}{\bar{\rho}}, \tag{4.13}$$

where $K = \frac{1}{2}\widetilde{u_i u_i} = \frac{1}{2}\overline{\rho u'_i u'_i}/\bar{\rho}$ is the Favre averaged turbulent kinetic energy (TKE), $P = -S\widetilde{u'_1 u'_2}$ is the production of TKE, $\epsilon_s = \bar{\nu}\overline{\omega'_i \omega'_i}$ is the solenoidal dissipation rate,

$\epsilon_c = \frac{4}{3}\bar{\nu}\overline{d'^2}$ is the compressible/dilatational dissipation rate and $\overline{p'd'}$ is the pressure dilatation. Here $d' = u'_{i,i}$ is the fluctuating velocity dilatation, ω' is the fluctuation in vorticity ($\nabla \times \mathbf{u}$), $p' = \left(\rho'\overline{T} + \rho'T' + \overline{\rho}T' - \overline{\rho'T'}\right) R$ is the fluctuation in pressure and R is the gas constant. We monitor the budget of kinetic energy equation (5.2.1) in all collective and modal simulations in homogeneous shear.

4.2.1 Numerical procedure

We use gas-kinetic method for calculating numerical fluxes at the cell interface. The gas-kinetic method is a finite volume based method developed from Boltzmann Bhatnagar-Gorss-Krook theory for simulating compressible flows. The kinetic Boltzmann equation is an evolution equation for distribution function for a single particle. The gas-kinetic equation is a first order integro-partial differential equation with a linear advection term. The fundamental quantity in gas-kinetic equation is the particle distribution function from which any of the flow variables of interest, such as density, momentum and energy can be easily calculated. Details involved in the numerical solution of equations arising out of gas-kinetic method can be found in [2, 5, 14, 15, 105]. In the remainder of this section we present the Runge-Kutta procedure used for solving the RDT and Burgers equations, initial and boundary conditions for DNS simulations and results for numerical validation against previous results.

Initial conditions for DNS

The computational domain is a cubic box of dimension $l = 2\pi$. The box is discretized into $N_x \times N_y \times N_z$ cells with $N_x = 256, N_y = 256$ and $N_z = 512$ along the x, y and, z directions respectively. We apply uniform shear in u_1 along the x_2 direction such that the gradient of the mean flow field is $\bar{U}_{i,j} = S\delta_{i1}\delta_{2j}$ with S as the shearing rate.

We begin our simulations from a three dimensional, random, isotropic and solenoidal ($\nabla \cdot \mathbf{u} = 0$) velocity field. The temperature and density are initially uniform in the box which is different from consistent initial conditions suggested by Ristorchelli and Balisdell. The reasons underlying the choice of initial conditions without any thermodynamic fluctuations are:

1. In engineering mixing and boundary layers, velocity and thermodynamic variables are not in equilibrium.

2. The chosen conditions lead to an excellent agreement with DNS performed by Sarkar [9].

3. Precise agreement with RDT and 'pressure-released' turbulence possible with present conditions.

We energize only large scales in the flow by restricting energy containing wavenumbers in the range $\kappa \in [\kappa_{min}, \kappa_{max}]$. The velocity field is periodic and initially satisfies a specified one-dimensional energy spectra [22, 56, 88]

$$E(\kappa, 0) = \frac{\hat{u}_i \hat{u}_i^*}{4\pi\kappa^2} = A\kappa^4 e^{-B\kappa^2}, \quad \kappa \left(= \sqrt{\kappa_x^2 + \kappa_y^2 + \kappa_z^2}\right) \in [\kappa_{min}, \kappa_{max}], \tag{4.14}$$

where $B = 0.54$, $\hat{u}_i$ is the Fourier amplitude and $\hat{u}_i^*$ is its complex conjugate. The coefficient A magnifies the velocity field uniformly throughout the domain and is chosen to achieve the required turbulent Mach number.

The procedure [22, 88, 105–107] for generation of initial condition yields a velocity field which is random, isotropic, incompressible and satisfies a desired energy spectra. We choose A to match the prescribed initial turbulent Mach number M_{t0} and kinematic viscosity ν to get a desired initial Taylor microscale Reynolds number $Re_{\lambda 0}$.

Boundary conditions for DNS

We apply periodic boundary condition for boundaries normal to the x_1 and x_3 directions. For boundaries normal to x_2 (the shear direction), we apply shear-periodic boundary condition [82–85]

$$\phi(t, x + m_1 L_x, y + m_2 L_y, z + m_3 L_z) = \phi(t, x - S m_2 L_y t, y, z), \tag{4.14}$$

where L_x, L_y and L_z are the dimensions of the box along the three co-ordinate directions and m_1, m_2, m_3 are arbitrary integers. Along the direction of shear, only the fluctuating component of velocity is periodic while the mean velocity is specified to maintain the prescribed shear S.

Validation against DNS by Sarkar

Before we discuss DNS simulations performed for this work, we compare against DNS for homogeneous shear flows performed by Sarkar [9]. Sarkar performs a series of homogeneous shear flow simulations with varying M_{g0} and M_{t0}. We compare against one of the Sarkar's simulation cases for which the flow parameters are provided in Table 4.1. In Figs. 4.3 and 4.4 we compare our DNS results against that of Sarkar. It is clear that the evolution of Reynolds stress anisotropies $b_{11}, -2b_{12}, b_{22}$ and correlation coefficient $R(u,v) = \overline{u'v'}/\left(u'_{rms} v'_{rms}\right)$ computed in our DNS agree well with Sarkar. The comparison against DNS results in [9] also serves to validate the DNS code used for the current work.

Case	M_{g0}	M_{t0}	$Re_{\lambda 0}$	Pr_0	(Sk/ϵ_0)
A4	1.32	0.40	14	0.7	10.8

Table 4.1
DNS parameters of homogeneous shear case A4 of Sarkar [9].

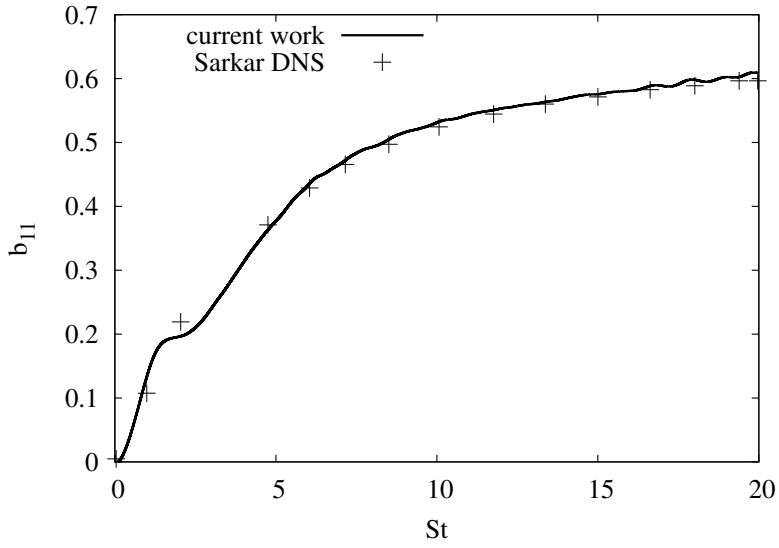

(a)

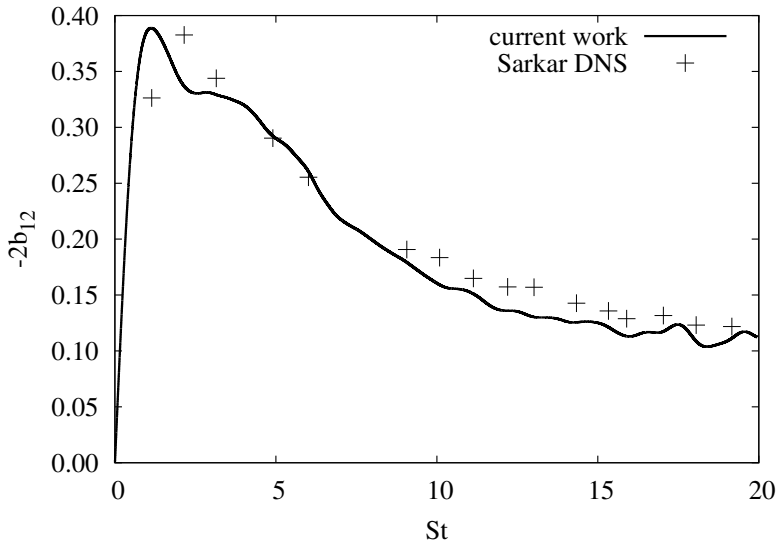

(b)

Fig. 4.3. Comparison against DNS case A4 of Sarkar [9]: a) b_{11}, and b) $-2b_{12}$.

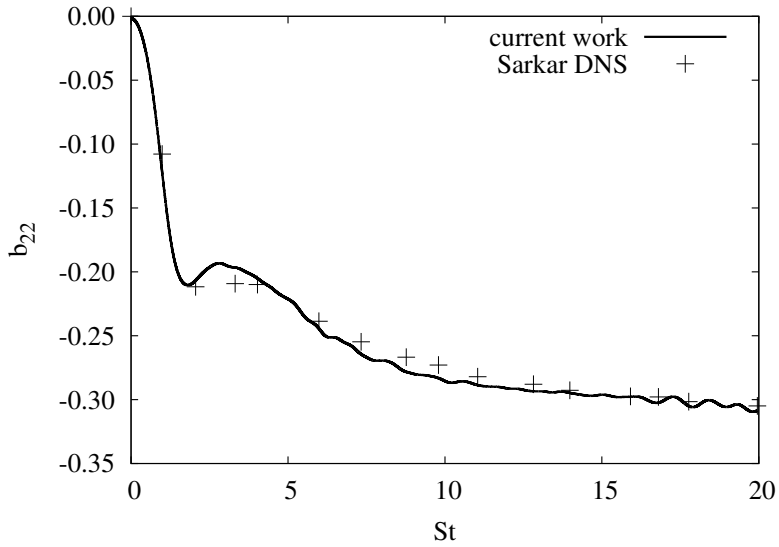

(a)

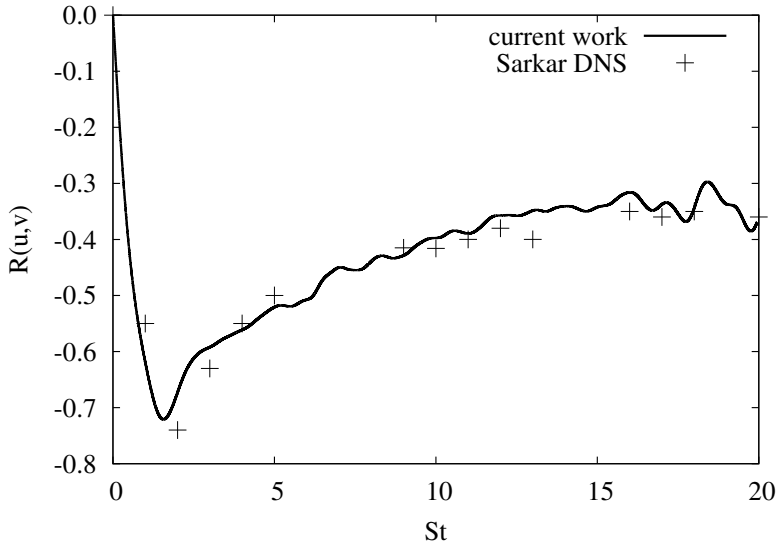

(b)

Fig. 4.4. Comparison against DNS case A4 of Sarkar [9]: a) b_{22}, and b) $R(u,v) = \overline{u'v'}/\left(u'_{rms}v'_{rms}\right)$.

RDT and Burgers: 4th order Runge-Kutta scheme

We use fourth order Runge-Kutta scheme (RK-4) for solving the ordinary differential equations arising out of RDT in spectral space. The RK-4 scheme for solving an 'initial value problem' given by

$$\dot{y} = f(t, y), \quad y(t_0) = y_0, \tag{4.14}$$

is summarized in the following steps:

$$\begin{aligned} y_{n+1} &= y_n + \frac{1}{6}\left(k_1 + 2k_2 + 2k_3 + k_4\right), \\ t_{n+1} &= t_n + \Delta t. \end{aligned}$$

Here $y_{n+1} = y(t_{n+1})$ and Δt is the time step. The increments $k_1, \ldots, k_4$ are calculated from

$$\begin{aligned} k_1 &= f(t_n, y_n)\Delta t, \\ k_2 &= f(t_n + \frac{\Delta t}{2}, y_n + \frac{k_1}{2})\Delta t, \\ k_3 &= f(t_n + \frac{\Delta t}{2}, y_n + \frac{k_2}{2})\Delta t, \\ k_4 &= f(t_n + \Delta t, y_n + k_3)\Delta t. \end{aligned}$$

4.3 Analysis of Modal Behavior

In order to explain the role played by individual Fourier components to bring about the collective behavior, we investigate the evolution of individual modes in isolation. We refer to this analysis of individual Fourier modes as 'modal analysis' (not to be confused with similar terminology used in stability analysis). Since the initial condition for *collective behavior* is divergence-free, we consider all possible modes that satisfy $\nabla \cdot \mathbf{u} = 0$ in physical space or equivalently $\hat{\mathbf{u}} \cdot \vec{\kappa} = 0$ in Fourier

	Fourier space		**Physical space**			
	$\vec{k}$	$\hat{\mathbf{u}}$	u	v	w	$\nabla \cdot \mathbf{u}$
Mode 1	(1,0,0)	(0,1,0)	0	$\sin(nx + \Delta)$	0	0
Mode 2	(1,0,0)	(0,0,1)	0	0	$\sin(nx + \Delta)$	0
Mode 3	(0,1,0)	(1,0,0)	$\sin(ny + \Delta)$	0	0	0
Mode 4	(0,1,0)	(0,0,1)	0	0	$\sin(ny + \Delta)$	0
Mode 5	(0,0,1)	(1,0,0)	$\sin(nz + \Delta)$	0	0	0
Mode 6	(0,0,1)	(0,1,0)	0	$\sin(nz + \Delta)$	0	0

Table 4.2

Mutually independent family of modes studied for analysis of modes in isolation. The velocity field is initially incompressible. ($n \in [1, 2, 3, \ldots]$) and $\Delta \in [0, \pi]$ is phase shift. The results shown in the paper have $n = 1$ and $\Delta = 0$.

space. The Cartesian axis is defined such that shear is along the y axis while the mean flow is along the x axis (streamwise direction). Therefore the third axis, z (spanwise direction), is normal to the direction of shear and mean flow.

Modes are characterized by wave-amplitude and wave-vector. A general mode with direction given by $\vec{\kappa} = (\kappa_x, \kappa_y, \kappa_z)$ is shown Fig. 4.5. We systematically investigate mutually orthogonal modes which are initially incompressible ($\nabla \cdot \mathbf{u} = 0$) and have wave-vectors oriented along either spanwise, streamwise or shear direction. Along with the incompressibility condition, this yields six mutually independent and orthogonal family of *initially-incompressible* modes for investigation which are detailed in Table 4.2.

We also investigate modes which are initially compressible with $\nabla \cdot \mathbf{u} \neq 0$. The investiagted modes are shown in Table 4.3. In the simulations performed for collective-behavior, modes with $\nabla \cdot \mathbf{u} \neq 0$ are not initially present, though at later times these modes are energized through non-linear interactions. For cases considered in this

	Fourier space		Physical space			
	$\vec{k}$	$\hat{\mathbf{u}}$	u	v	w	$\nabla \cdot \mathbf{u}$
Mode 7	(1,0,0)	(1,0,0)	$\sin(nx)$	0	0	$n\cos(nx+\Delta)$
Mode 8	(0,1,0)	(0,1,0)	0	$\sin(ny)$	0	$n\cos(ny+\Delta)$
Mode 9	(0,0,1)	(0,0,1)	0	0	$\sin(nz)$	$n\cos(nz+\Delta)$

Table 4.3
Mutually independent modes studied for analysis of modes in isolation. The velocity field is initially compressible. ($n \in [1,2,3,\ldots]$) and $\Delta \in [0,\pi]$ is phase shift. The results shown in the paper have $n = 1$ and $\Delta = 0$.

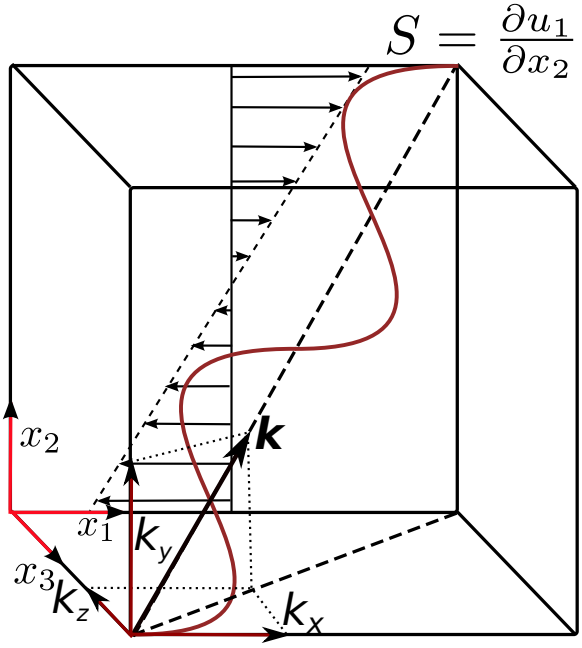

Fig. 4.5. Modal analysis: schematic diagram (not to scale) of the computational setup for a typical mode in homogeneous shear flow.

study non-linear interaction is relatively weak, so contribution of these modes is not very significant.

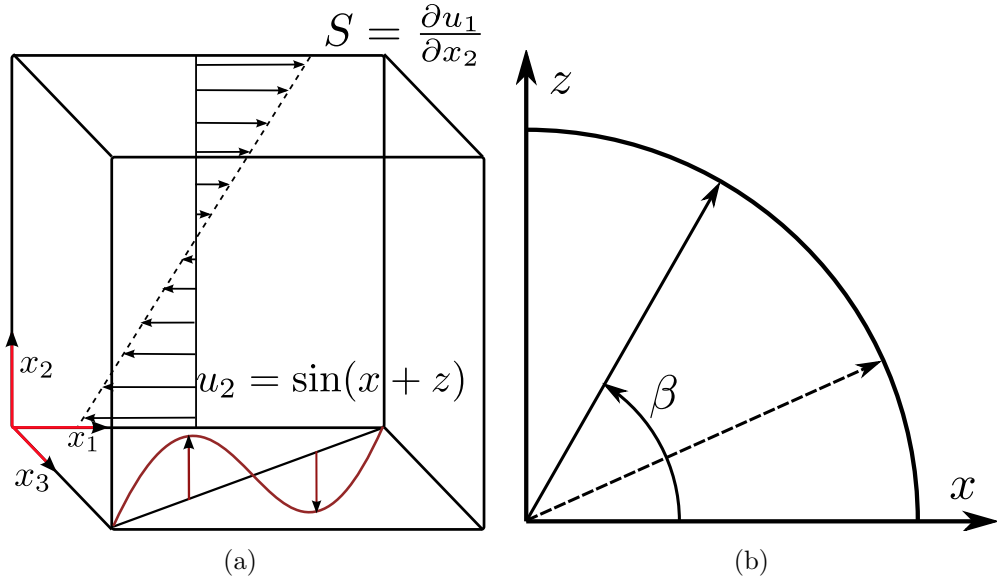

Fig. 4.6. Mixed modes: growth in incompressible compared to compressible case depend on direction of modes.

As we will see in later sections, another important family of modes are those with direction of propagation in the plane normal to the direction of shear. We refer to such modes as 'oblique modes' which are characterized by the angle β it makes with the streamwise direction and its amplitude. Modes 1 and 6 are limiting cases of oblique modes. A typical oblique-mode is given as

$$\vec{u} \equiv (u, v, w) = (0, \sin(mx + nz + \Delta), 0), \quad \Delta \in [0, \pi], \tag{4.8}$$

where $n \in I^+$ is the wavenumber and Δ is an arbitrary phase shift. In Fig. 5.4(a) we show a typical oblique mode along with the computational domain and the shear.

4.3.1 Characterization of modal behavior of pressure

Pressure plays a pivotal role in bringing about the three stage behavior in compressible homogeneous shear slows. Therefore, it is pertinent to first characterize

the behavior of pressure before we discuss the effect of pressure on the evolution of kinetic energy of different modes.

In incompressible flows, pressure acts as a Lagrange multiplier to enforce a divergence-free velocity field and evolves according to the pressure Poisson equation– an elliptic equation in space. On the other hand, in compressible flows pressure assumes the role of a thermodynamic variable and is governed by the equation-of-state. Also, in compressible flows pressure has an acoustic nature and evolves according to the wave equation. The timescale of pressure governs the acoustic timescale. When the acoustic timescale becomes comparable to the flow-timescale the wave nature of pressure becomes evident in the oscillatory behavior of the temporal evolution of different modes. The flow and acoustic time-scales for different modes could be greatly different. This demands a full characterization of behavior of pressure and an analysis in the evolution of timescale (or frequency) in homogeneous shear. For the ease of analytical amenability we will discuss the evolution in the context of RDT. Although, the analysis is valid for a single mode with an arbitrary direction, the discussion is primarily in the context of oblique modes.

The linearized non-dimensional transport equation for pressure were derived by Kovasznay [108] in the context of homogeneous turbulent flows. Livescu *et. al* [109] extended the linearized equations for homogeneous turbulent shear flows in the RDT limit. They derive equations for a moving co-ordinate system following the Rogallo's transformation of co-ordinates [106, 107]. The governing equation for fluctuating pressure [109] in the RDT limit for the moving reference frame is given as:

$$p'_{,t} = \gamma \langle p \rangle \Delta' + \frac{4 \langle \mu \rangle (\gamma - 1)}{Re_0} S s'_{12} + \frac{\langle \mu \rangle}{M_0^2 Re_0 Pr} \left(\frac{p'_{,jj}}{\langle p \rangle} - \frac{\rho'_{,jj}}{\langle p \rangle} \right) \langle T \rangle \tag{4.8}$$

where B_{ij} ($x'_i = B_{ij} x_j$) is the Rogallo's transformation matrix, $s'_{ij} = \frac{1}{2}(u''_{i,k} B_{kj} + u''_{j,k} B_{ki})$ is the strain rate tensor, $\Delta' = u''_{i,k} B_{ki}$ is the dilatation, S is the mean shear

and u_i'' is the Favre averaged [79] fluctuating velocity. The linearized equation for mean pressure is given by

$$\langle p \rangle_{,t} = \frac{\langle \mu \rangle (\gamma - 1)}{Re_0} S^2, \tag{4.8}$$

which yields mean pressure as constant in inviscid flows ($\mu = 0$) and small for viscous flows considered in this study. DNS results show that for $M_g = 20$, increase in $\langle p \rangle$ and $\langle T \rangle$ after $St = 20$ is about $10 - 15\%$. The equation for pressure fluctuations in inviscid RDT can finally be written as (details in [109])

$$\frac{p'_{,ttt}}{a_0^2} = p'_{,tjk} B_{ji} B_{ki} - 4S p'_{,jk} B_{j1} B_{k2} \tag{4.8}$$

where $a_0 = \sqrt{\gamma R \langle T \rangle}$ is the initial speed of sound. Applying Fourier transform to Eq. 4.3.1 in a fixed co-ordinate system ($B = \mathbf{I}$) yields pressure equation given as

$$\frac{d^3 \hat{p}}{dt^3} = -a_0^2 \left(\kappa^2 \frac{d\hat{p}}{dt} - 4\kappa_1 \kappa_2 S \hat{p} \right) \tag{4.8}$$

where $\hat{p}$ is the Fourier amplitude and $\kappa = (\kappa_1, \kappa_2, \kappa_3)$ is the wave vector with $\kappa = |\kappa|$ as the magnitude. Alternatively, eq. (4.3.1) can be derived directly from eqs. (4.6)–(4.8) through the following steps:

$$\frac{d^2 \hat{p}}{dt^2} = -i\gamma \left(\frac{d\bar{p}}{dt} (\hat{u}_j \kappa_j) + \bar{p} \frac{d}{dt} (\hat{u}_j \kappa_j) \right),$$

$$\frac{d^3 \hat{p}}{dt^3} = -i\gamma \left(2 \frac{d\bar{p}}{dt} \frac{d\bar{p}}{dt} (\hat{u}_j \kappa_j) + \bar{p} \frac{d^2}{dt^2} (\hat{u}_j \kappa_j) \right),$$

$$\frac{d}{dt} (\hat{u}_i \kappa_i) = -\frac{i \kappa_i^2 \hat{p}}{\bar{\rho}} - \hat{u}_j \kappa_i S_{ij} - \hat{u}_i \kappa_j S_{ji},$$

$$\frac{d^2}{dt^2} (\hat{u}_i \kappa_i) = -\frac{i}{\bar{\rho}} \left(\kappa^2 \frac{d\hat{p}}{dt} + 2\kappa_i \frac{d\kappa_i}{dt} \hat{p} \right) - 2 \frac{d}{dt} (\hat{u}_j \kappa_i S_{ij}),$$

$$\frac{d^3 \hat{p}}{dt^3} = -i\gamma \left[-\frac{i\bar{p}}{\bar{\rho}} \left(\kappa^2 \frac{d\hat{p}}{dt} - 2\hat{p} \kappa_i \kappa_j S_{ji} \right) + 2i \frac{\kappa_1 \kappa_2 S}{\bar{\rho}} \hat{p} \bar{p} \right],$$

which finally yields the evolution equation for pressure

$$\frac{d^3\hat{p}}{dt^3} = -a_0^2\left(\kappa^2\frac{d\hat{p}}{dt} - 4\kappa_1\kappa_2 S\hat{p}\right).$$

The evolution equation for pressure 4.3.1 is dependent on both magnitude and direction of wave through κ^2 and $\kappa_1\kappa_2$, respectively. The pressure equation is decoupled from the velocity equation but is still not amenable for analytical analysis. Equation (4.3.1) can be further simplified using the solution to the evolution equation for wave number $\left(\frac{d\kappa_i}{dt} + \kappa_k\frac{\partial\langle U_k\rangle}{\partial x_i} = 0\right)$ in homogeneous shear flow

$$\kappa_1(t) = \kappa_1(0) \equiv \kappa_1^0; \quad \kappa_2(t) = \kappa_2(0) - \kappa_1(0)St \approx -\kappa_1^0 St \text{ (for late } St); \quad \kappa_3(t) = \kappa_3(0) \equiv \kappa_3^0. \tag{4.8}$$

At sufficiently large shear times, κ_2 is large enough to make the following approximation: $\kappa(t) \approx \kappa_2(t) \approx \kappa_1^0 St$. Equation (4.3.1) can be further simplified into

$$\frac{d^3\hat{p}}{dt^3} \approx -a_0^2\kappa_1^2(0)S^2\left(t^2\frac{d\hat{p}}{dt} + 4t\hat{p}\right) \tag{4.8}$$

For oblique modes $\kappa_1(0)$ can be written as $\kappa_1(0) = \kappa(0)\cos(\beta) \equiv \kappa_0\cos(\beta)$, where, k_0 is the magnitude of the wave and β is the angle made by the wave-vector with respect to the direction of mean flow (x axis). Now, defining non-dimensional time as $t^* = (a_0\kappa_0 S\cos(\beta))^{1/2}\,t$, Eq. (4.3.1) can be written as

$$\frac{d^3\hat{p}}{dt^{*3}} = -\left(t^{*2}\frac{d\hat{p}}{dt^*} + 4t^*\hat{p}\right). \tag{4.8}$$

The non-dimensional time t^* can be cast in a form which is very similar to 'mixed-time'

$$t^* = \frac{S^*t}{\sqrt{M_{g0}^*}}, \tag{4.8}$$

where, $S^* = S\cos\beta$ and $M^*_{g0} = M_{g0}\cos\beta$ the effective shear and Mach number seen by the oblique wave. Since equation (4.3.1) is independent of the direction and magnitude of the oblique wave, it shows that frequency and amplitude of pressure scales in t^* time. It should be noted that the analysis assumes a late time approximation, therefore scaling is valid for late shear times. In Fig. (4.7) scaling of amplitude and frequency of pressure is shown for oblique modes with different β but same κ_0. In Fig. (4.8) scaling is shown when both β and κ_0 are varied. The important conclusions can be summarized as follows:

1. Oblique modes with different β see different effective shear $S^* = S\cos(\beta)$ and gradient Mach number $M^*_{g0} = M_{g0}\cos(\beta)$. Therefore, for a fixed S effective gradient Mach number seen by oblique mode decreases with increasing β. The limiting case is the oblique mode with $\beta = 90$ (mode 6) for which $M^*_{g0} = 0$ for all S.

2. In non-dimensional mixed-timescale t^*, evolution of pressure is independent of β. It is concluded that frequency scales in mixed-time in homogeneous shear.

3. The relevant parameter in homogeneous shear is M_{g0} and not S, β or κ_0.

4. For large β or κ_0, the effective gradient Mach number seen by an oblique mode could be near incompressible.

RDT simulations for collection-of-modes in [11, 13] show a critical gradient Mach number of unity beyond which three stage behavior is observed. We postulate that such a behavior results from certain modes showing growth for an effective M^*_{g0} greater than unity. This leads us to define $M^*_{g0} = 1$ as the critical gradient Mach number and a corresponding β_{crit} given by

$$\cos(\beta_{crit}) = \frac{1}{M_{g0}}, \quad \left[M^*_{g0} = 1 = M_{g0}\cos\left(\beta_{crit}\right)\right]. \tag{4.8}$$

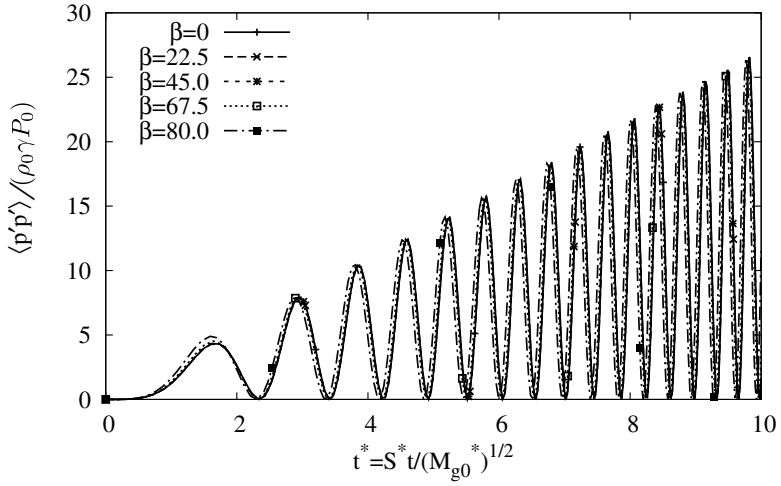

Fig. 4.7. Scaling of amplitude and frequency of pressure in RDT for different β in t^* time. For all cases $|\kappa_0|$ and S are identical. For $\beta = 0$ and $\kappa_0 = 1$ the effective initial Mach number is $M_{g0} = 10$.

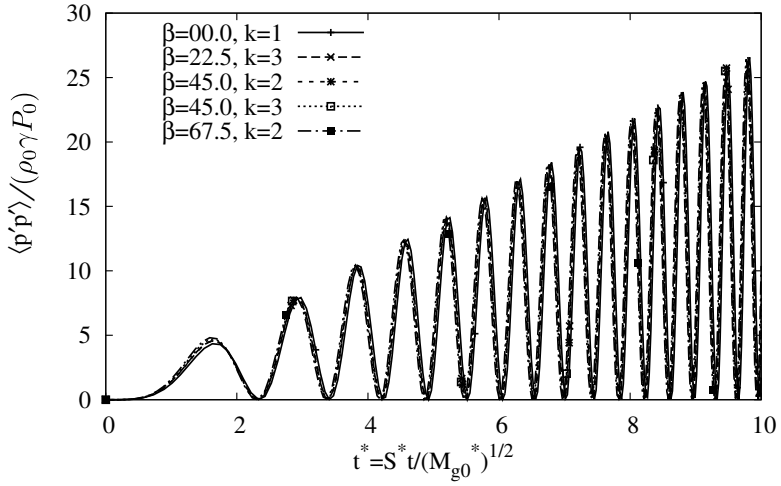

Fig. 4.8. Scaling of amplitude and frequency of pressure in RDT for different β in t^* time. For all cases only S is identical. For $\beta = 0$ and $\kappa_0 = 1$ the effective initial Mach number is $M_{g0} = 10$.

Kinetic energy of oblique modes with $\beta > \beta_{crit}$ grows and those with $\beta < \beta_{crit}$ decays in time. We will discuss this is further sections.

Till now we have discussed the scaling of frequency of pressure without a quantifying analysis. We now analyze the evolution of frequency of pressure (acoustic frequency) in homogeneous shear. The coefficient $\omega_0^4 = (a_0\kappa_1(0))^2 S^2$ of the right hand side of Eq. 4.3.1 is proportional to the product of initial acoustic frequency $(a_0\kappa_1(0))$ and that of the mean flow (S). Equation 4.3.1 can be further cast into

$$\frac{d^3\hat{p}}{dt^3} + q\frac{d\hat{p}}{dt} + r\hat{p} \approx 0 \tag{4.8}$$

where $q = \omega_0^4 t^2$ and $r = 4\omega_0^4 t$ are the time-dependent coefficients of the third-order ordinary differential equation (ODE). It is not trivial to find analytical solutions to third order ODE's with coefficients functions of the independent variable. But if the coefficients are monotonic and 'moderate' functions of time, a qualitative insight can be obtained about the nature of solutions to the ODE by treating the coefficients (q, r) as local constants. With q and r as local constants, a general solution to Eq. 4.3.1 can be written as $\hat{p}(t) \sim \hat{p}_0 e^{yt}$. Putting the general solution for $\hat{p}(t)$ in Eq. 4.3.1 we get the following characteristic equation

$$y^3 + qy + r = 0 \tag{4.8}$$

A solution to the cubic equation (4.3.1) can be found using Cardano's formula [110] by using guess solution of the following forms

$$y_1 = \left(a + \sqrt{b}\right)^{\frac{1}{3}} + \left(a - \sqrt{b}\right)^{\frac{1}{3}} \tag{4.8}$$

$$y_2 = \omega\left(a + \sqrt{b}\right)^{\frac{1}{3}} + \omega^2\left(a - \sqrt{b}\right)^{\frac{1}{3}} \tag{4.8}$$

$$y_3 = \omega^2\left(a + \sqrt{b}\right)^{\frac{1}{3}} + \omega\left(a - \sqrt{b}\right)^{\frac{1}{3}} \tag{4.8}$$

where $\omega = \frac{-1+i\sqrt{3}}{2}$ is one of the imaginary solutions of the cube root of unity. By substituting Eqs. (4.3.1)–(4.3.1) in Eq. (4.3.1) one can easily find the values of constants to be: $a = -\frac{r}{2}$ and $b = \left(\frac{r}{2}\right)^2 + \left(\frac{q}{3}\right)^3$. Defining intermediate variables

$$s_1 = \left(-2\omega_0^4 t + \left(\frac{\omega_0^{12}t^6}{27} + 4\omega_0^8 t^2\right)^{\frac{1}{2}}\right)^{\frac{1}{3}}, \quad s_1 = \left(-2\omega_0^4 t - \left(\frac{\omega_0^{12}t^6}{27} + 4\omega_0^8 t^2\right)^{\frac{1}{2}}\right)^{\frac{1}{3}} \tag{4.8}$$

the roots of the characteristic equation (4.3.1) can be written in the following form

$$\begin{aligned} y_1 &= (s_1 + s_2) \\ y_2 &= -\frac{1}{2}(s_1 + s_2) + i\frac{\sqrt{3}}{2}(s_1 - s_2) \\ y_3 &= -\frac{1}{2}(s_1 + s_2) - i\frac{\sqrt{3}}{2}(s_1 - s_2). \end{aligned} \tag{4.7}$$

The imaginary part of the roots y_2 and y_3 represent frequency of temporal oscillation of pressure modes and thus are related to frequency of acoustic oscillations in the shear flow. Acoustic frequency increases monotonically in time and the growth is linear at late shear times. Notably, the region of linear growth starts once acoustic frequency becomes larger than that of the mean flow.

Early time behavior

In this section we will investigate the early time behavior of frequency of acoustic oscillations s_1 and s_2. We cast s_1 and s_2 in the following form:

$$s_1 = \left(2\omega_0^4 t\right)^{\frac{1}{3}}\left(-1 + \left(\frac{\omega_0^4 t^4}{108} + 1\right)^{\frac{1}{2}}\right)^{\frac{1}{3}}, \quad s_2 = -\left(2\omega_0^4 t\right)^{\frac{1}{3}}\left(1 + \left(\frac{\omega_0^4 t^4}{108} + 1\right)^{\frac{1}{2}}\right)^{\frac{1}{3}}. \tag{4.7}$$

When $\frac{\omega_0^4 t^4}{108} \ll 1$, $|s_1| \approx 0$ and $|s_2| \approx \omega_0^{4/3} t^{1/3}$. Using definitions of $\omega_0^2 = a_0 \kappa_1(0) S$ and the initial modal Mach number $M_{g0} = \frac{Sl}{a_0} = \frac{S}{a_0 \kappa_1(0)}$, the condition for *early time* can be written as:

$$\frac{\omega_0^4 t^4}{108} \ll 1 \Rightarrow \frac{St}{\sqrt{M_{g0}}} \ll (108)^{1/4} \approx 3.23 \tag{4.7}$$

Now, at early times, the relevant time-scale for pressure evolution is given by

$$\frac{1}{|s_2|} \approx \frac{1}{\omega_0^{4/3} t^{1/3}}. \tag{4.7}$$

For times small compared to the time-scale of pressure evolution, the pressure field can be considered frozen and thus unresponsive to the velocity field. Since evolution of pressure is frozen, velocity field is driven only due to inertial forces. The velocity field evolves like Burgers flow and the resulting behavior is termed as 'pressure-released limit'. The aforementioned inequality can be written as

$$t \ll \frac{1}{\omega_0^{4/3} t^{1/3}} = \frac{1}{((a_0 \kappa_1(0) S)^2 t)^{1/3}} = \frac{1}{\left(\left(\frac{S}{M_{g0}} S \right)^2 t \right)^{1/3}} \quad \Rightarrow \frac{St}{\sqrt{M_{g0}}} \ll 1. \tag{4.7}$$

The time regime $\frac{St}{\sqrt{M_{g0}}} \ll 1$ constitutes the first stage. The corresponding equality $\frac{St}{\sqrt{M_{g0}}} = 1$ demarcates the transition from first to second stage. At times comparable to the time-scale of pressure, pressure starts playing a significant role and acoustics begin to dominate the evolution of the flow field.

Late time behavior

In this section, we investigate late time behavior of the frequency (s_1, s_2) of pressure evolution. We begin by looking at s_1 and s_2 in the following form:

$$s_1 = \frac{\omega_0^2 t}{\sqrt{3}} \left(-\frac{\sqrt{108}}{\omega_0^2 t^2} + \left(1 + \frac{108}{\omega_0^4 t^4} \right)^{\frac{1}{2}} \right)^{\frac{1}{3}}, \quad s_2 = -\frac{\omega_0^2 t}{\sqrt{3}} \left(\frac{\sqrt{108}}{\omega_0^2 t^2} + \left(1 + \frac{108}{\omega_0^4 t^4} \right)^{\frac{1}{2}} \right)^{\frac{1}{3}}. \tag{4.7}$$

When $\frac{\sqrt{108}}{\omega_0^2 t^2} \ll 1$ or, equivalently, $\frac{St}{\sqrt{M_{g0}}} \gg \sqrt{108}$ we have,

$$|s_1| \approx |s_2| \approx \omega_0^2 t \tag{4.7}$$

Thus, at late times frequency of pressure increases linearly with time. It is reasonable to say that, for sufficiently large time, time-scale of pressure would be much smaller than the flow time scale. Such small time scale or pressure would make it behave like-incompressible where time-scale of pressure is zero. This leads to the following inequality between time-scales of pressure and velocity field at large times

$$\frac{1}{\omega_0^2 t} \ll \frac{1}{S} \quad \Rightarrow \frac{1}{a_0 \kappa_1(0) S t} \ll \frac{1}{S} \quad \Rightarrow a_0 t \kappa_1(0) \equiv \frac{a_0 t}{l_0} \gg 1 \tag{4.7}$$

Indeed, the transition from second to third stage occurs approximately at the corresponding equality $\frac{a_0 t}{l_0} = 1$. In Figs. (4.9) and (4.10) we compare late stage frequency of pressure evolution (or acoustics) obtained from DNS against analytical results for mode-1 at different gradient Mach numbers. We see an excellent match in acoustic frequency supporting the approximate analysis performed in this section for the late-stage behavior.

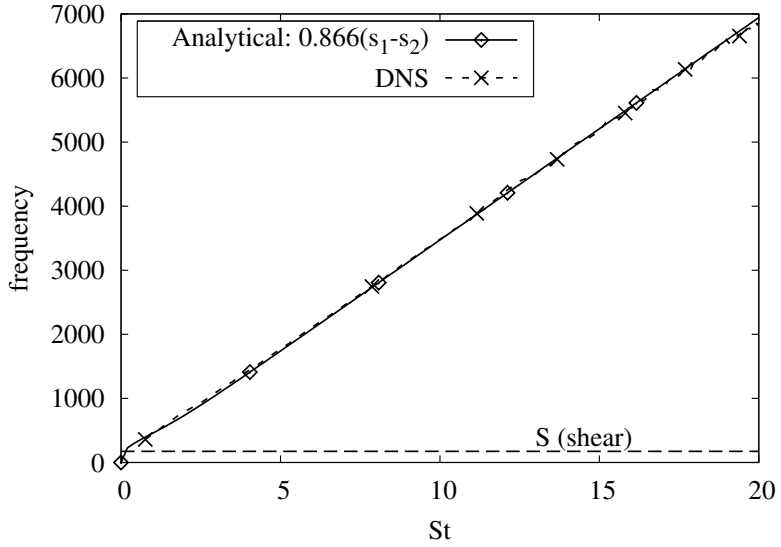

(a)

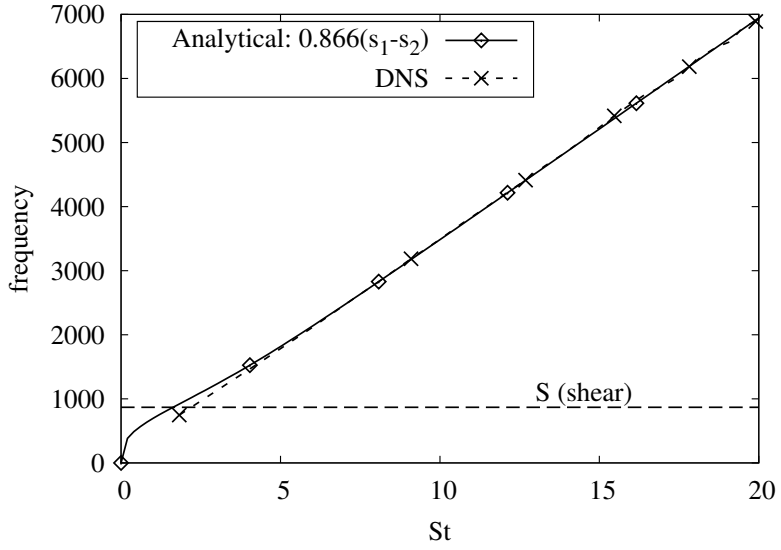

(b)

Fig. 4.9. Comparison of DNS and RDT analysis for frequency of acoustics/pressure: (a)$M_g = 0.5$, and (b)$M_g = 2.5$.

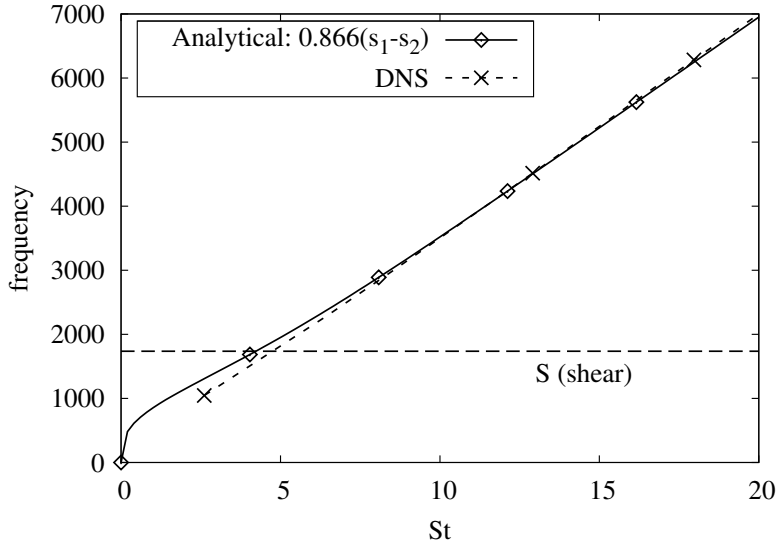

(a)

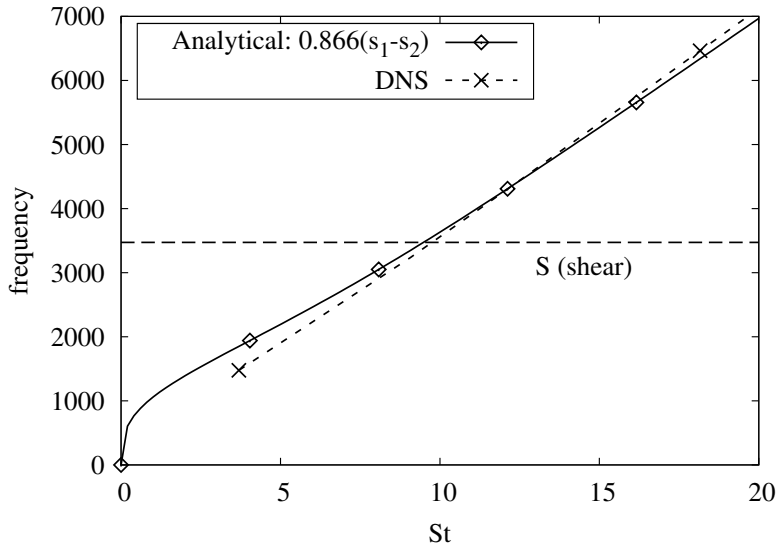

(b)

Fig. 4.10. Comparison of DNS and RDT analysis for frequency of acoustics/pressure: (a)$M_g = 5.0$, and (b)$M_g = 10.0$.

Intermediate time behavior

We identified two limiting behaviors of the evolution of pressure time-scale. For an intermediate time given by

$$\frac{l_0}{a_0} \ll t \ll \frac{\sqrt{M_{g0}}}{S} \tag{4.7}$$

is a distinct regime of evolution where time-scale of pressure competes with that of velocity field. In this intermediate time pressure evolves to significantly effect the velocity field. At very late times, pressure eventually has such small time-scale that it starts to immed($\beta = \pi/2$)iately react to inertia and thus behaves like-incompressible.

4.3.2 Modal kinetic energy

We study the effect of pressure on evolution of kinetic energy of different modes. We perform DNS to study each mode (modes 1-9) independently and identify modes whose kinetic energy grows in time. All simulations start without any thermodynamic fluctuations ($\rho' = T' = 0$) and identical initial kinetic energy. In a similar analysis in incompressible homogeneous shear, it was found that only mode-6 grows. The kinetic energy of modes 2–5 either stays constant (with slow decay due to viscosity) or decays quickly in time. We will refer mode-6 as the 'solenoidal mode' for it is the only mode that grows in incompressible flows. Since, mode-6 is also associated with an increasingly large vorticity, we also refer to it as the 'vortical mode'. DNS in the compressible regime show that mode-6 still grows with growth rate very similar to that in the incompressible. But unlike incompressible shear flows, in compressible regime, characterized by high M_{g0}, additional family of modes grow. We identify three families of unstable modes in highly compressible shear flows: Mode 1, 6 and 9. The rest of the modes either do not grow or decay rapidly in time.

Evolution of mode-6 ($\beta = \pi/2$): solenoidal mode

The initial velocity field for this family mode is given by $(u, v, w) = (0, \sin(nz + \Delta), 0)$, where $n \in [1, 2, 3, \ldots]$ is the wavenumber and $\Delta \in [0, \pi]$ is an arbitrary phase shift. The velocity field is initially divergence-free with fluctuations along the direction of shear. The evolution of kinetic energy in shear time in DNS for mode-6 is given in Fig. 4.11(a). Kinetic energy for both RDT and DNS follow Burgers growth at all shear times. The Burgers growth is given by:

$$\frac{k}{k_0} \equiv \frac{\overline{u_i' u_i'}(t)}{\overline{u_i' u_i'}(t=0)} = 1 + (St)^2 \,. \tag{4.7}$$

Since RDT and DNS follows Burgers growth at all times, and since effect of pressure is absent in Burgers, it is evident that pressure plays no role in the evolution of mode-6. Also a close match between RDT and DNS shows that non-linearity does not play a significant role. Although, at late shear times growth rate in DNS shows a slow down due to the dissipative action of viscosity.

In mode-6, u_1 is the dominant fluctuation containing almost all kinetic energy ($k \approx \overline{u_1 u_1}$) at late times. Also, at late times, the wave-vector along the direction of shear κ_2 is dominant. Therefore, presence of all kinetic energy in u_1 maintains the incompressibility condition. Velocity field in evolution of mode-6 is solenoidal with only a negligible dilatational component. The solenoidal nature of mode-6 is also evident due to: (i) zero dilatation at all times and, (ii) growth of vorticity (ω') to very large values. Similar behavior is exhibited in solenoidal and dilatational dissipation.

The incompressible-like growth of mode-6 in compressible flows is not surprising because the effective Mach number seen by mode-6 ($\beta = \pi/2$) is zero irrespective of M_{g0}

$$M_{g0}^* = M_{g0} \cos\beta = M_{g0} \cos\left(\frac{\pi}{2}\right) = 0 \tag{4.7}$$

Evolution of kinetic energy for different initial modal gradient Mach number (M_{g0}) for mode-6 is plotted in Fig. 4.11(a). We see that M_{g0} has negligible effect on the growth of mode-6. It is clear that the behavior of mode-6 is unaffected by compressibility. Evolution of kinetic energy for different initial fluctuation Mach number (M_{t0}) is plotted in Fig. 4.11(b) and we see a negligible effect of M_t at all times on mode-6.

Evolution of mode-1 ($\beta = 0$): dilatational mode

The initial velocity field for this family of modes is given by $(u, v, w) = (0, \sin(nx + \Delta), 0)$, where $n \in [1, 2, 3, \ldots]$ is the wave number and $\Delta \in [0, \pi]$ is an arbitrary phase shift. This velocity field is initially divergence-free with fluctuations along the direction of shear. For initial shear time ($St < 2$), growth rate for mode-1 follows Burgers growth due to: (i) the inability of pressure to react quickly to inertia of the mean shear field thereby rendering pressure effect to be negligible, (ii) the negligible effect of viscosity on large length scales which in turn are associated with weaker gradients. The flow field behaves like Burgers till the time scale of the velocity field is much smaller than that of acoustic. The behavior at initial time for mode-1 is very similar to stage-1 in the 'collective behavior'. As compressibility builds up and flow time-scale becomes comparable to acoustic time-scale, the growth rate of kinetic energy slowly departs from Burgers. The growth of kinetic energy after the departure from Burgers ($St > 2$) is highly oscillatory which is characteristic of acoustic modes. A buildup of compressibility (large divergence) till the departure from Burgers, together with the fact that pressure in compressible flows is governed by the wave equation, leads to strong pressure waves being set up in the flow. Since pressure plays a key role in evolution of kinetic energy through the pressure-dilatation term $\overline{p' \frac{\partial u_i'}{\partial x_i}}$, oscillations in pressure is manifested in kinetic energy. Since mode 1 has (i) large dilatational dissipation compared to solenoidal dissipation and, (ii) large dilatational component of velocity compared solenoidal component, we refer to this

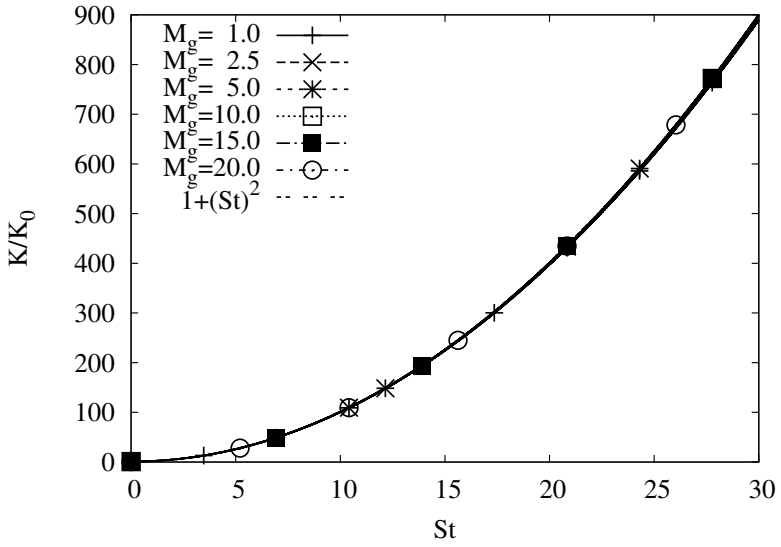

(a)

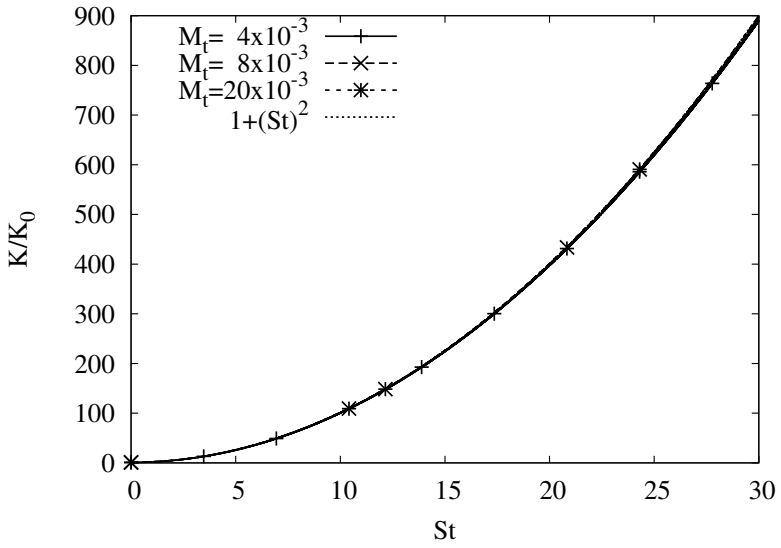

(b)

Fig. 4.11. Evolution of kinetic energy (k/k_0) for the solenoidal mode in shear time: (a) effect of initial modal gradient Mach number M_{g0} and, (b) effect of initial turbulent Mach number M_{t0}.

mode as the 'dilatational mode' or 'compressible mode'. Dilatation quickly builds up and at late shear times the flow field is primarily dilatational because the diagonal component of velocity gradient (trace of velocity gradient is dilatation) becomes dominant compared to the magnitude of the velocity gradient tensor $|u_{i,j}|$. At late shear times, the following approximations for solenoidal (k_s) and dilatational kinetic energies (k_d) are true for mode-1

$$k_s \approx \overline{u_1 u_1 + u_3 u_3} = \overline{u_1 u_1}, \qquad k_d \approx \overline{u_2 u_2}. \tag{4.7}$$

Starting with an initial condition where all energy is in the solenoidal component, dilatational kinetic energy becomes increasingly larger and at late shear times almost all energy is in the dilatational mode.

The effect of gradient Mach number on the evolution of kinetic energy for mode-1 is shown in Fig. (4.12). in mixed time. We see that in mixed time, peaks of kinetic energy align for high gradient Mach numbers ($M_{g0} > 2$. A similar alignment can be seen the evolution of pressure $\overline{p'p'}$. The alignment of peaks is an indicator of scaling of frequency in mixed time. The mixed time in the discussion is based on initial M_{g0}, which in-turn is depends on initial values of acoustic speed a_0 and the length-scale l_0 in the flow field. Using the equation for length-scale evolution from RDT $l \approx l_0/(St)$ and gradient Mach number $M_{g0} = Sl_0/a_0$ we can show that mixed time is proportional to the acoustic time based on the local length-scale as

$$\frac{St}{\sqrt{M_{g0}}} = \frac{St}{\sqrt{Sl_0/a_0}} \approx \frac{St}{\sqrt{S^2 lt/a_0}} = \sqrt{\frac{a_0 t}{l}}. \tag{4.7}$$

Therefore the scaling of frequency of pressure also occurs in local acoustic time scale. Since the oscillations are closely related to the pressure modes it can be concluded that the acoustic frequency scales in mixed time and local acoustic time. Because of its scaling characteristics, mixed time presents itself as an important timescale for modeling considerations.

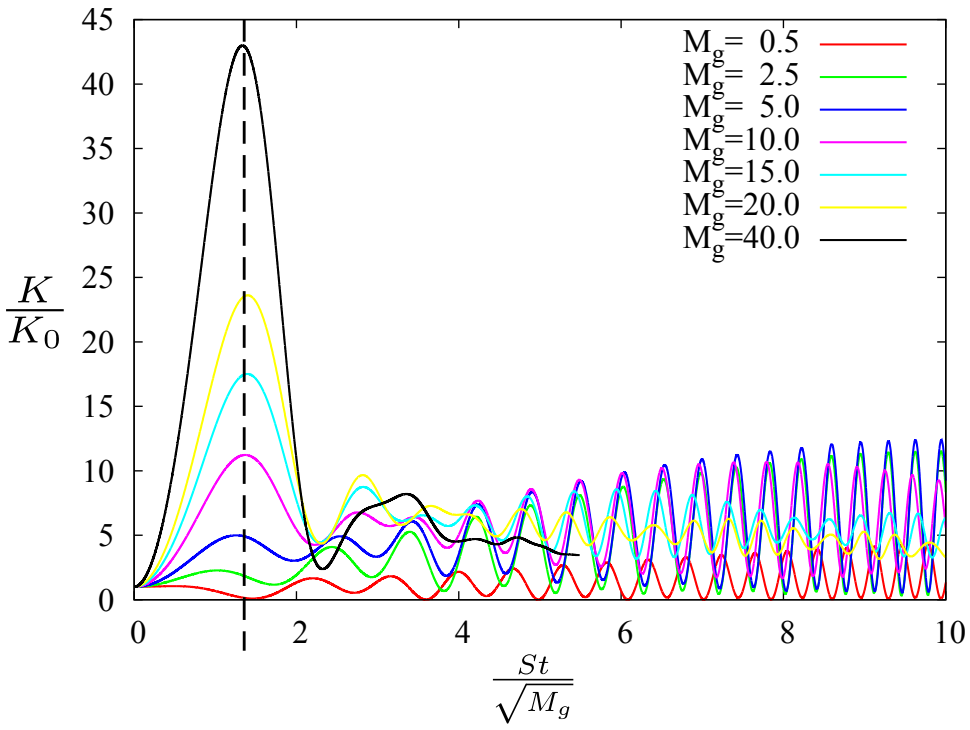

Fig. 4.12. Effect of initial gradient Mach number (M_{g0}) on a dilatational mode ($\beta = 0$) in mixed time.

Also, with increasing initial modal gradient Mach number M_{g0}, evolution of kinetic energy for mode-1 follows Burgers evolution for a longer shear time. This behavior is attributed to a larger effect of inertia compared to pressure in higher M_g simulations. Eventually kinetic energy evolution for all M_{g0} departs from Burgers when pressure effect becomes comparable to inertia or equivalently acoustic time scale increases to become comparable to timescale of velocity fluctuations.

Initial fluctuation Mach number has negligible effect on growth of mode-1 at initial times ($St < 5$) while at late shear times modes with higher M_t have smaller kinetic energy. The decrease in kinetic energy with increasing M_{t0} is attributed to a larger dissipation because of increased viscous effects in-order to keep the initial Re constant.

Evolution of mode-9

The initial velocity field for this family mode is given by $(u, v, w) = (0, \sin(ny + \Delta), 0)$, where $n \in [1, 2, 3, \ldots]$ is the wavenumber and $\Delta \in [0, \pi]$ is an arbitrary phase shift. The velocity field initially is along the direction of shear and has non-zero divergence. All kinetic energy is initially present in the dilatational component. It should be noted that in simulations of collective behavior, which start with an initially incompressible field, mode-9 is not energized. But, as dilatation builds up in the velocity field due to the family of dilatational modes, mode-9 is slowly energized. Due to small energy at initial times, contribution of mode-9 in collective behavior at late times remains negligible.

Evolution of oblique modes: $\beta \in (0, \pi/2)$

Till now we have identified two initially incompressible and unstable family of modes in homogeneous shear–solenoidal and dilatational modes. Initially incompressible modes with direction of propagation in the plane normal to the direction

of shear (x-z plane) carry characteristics of both solenoidal and dilatational modes. We refer such modes as the 'oblique modes' and are defined as

$$\vec{u} \equiv (u, v, w) = (0, \sin(mx + nz + \Delta), 0), \quad \Delta \in [0, \pi], \tag{4.7}$$

where $n \in I^+$ is the wavenumber and Δ is an arbitrary phase shift.

The key behavior of interest for the oblique mode is the dependence on initial gradient Mach number (M_{g0}). In Fig. (4.13) we study the effect of M_{g0} on oblique modes with different initial solenoidal and dilatational components. Evolution of kinetic energy for oblique modes with larger solenoidal component ($\kappa_z > \kappa_x$) is shown in Fig. 4.13(a). We see that at initial times all modes grow like Burgers which is consistent with initial time behavior of both mode-1 and mode-6. Oblique modes with higher M_{g0} follow Burgers growth for a longer time and have larger kinetic energy. Eventually all modes depart from Burgers evolution and show an oscillatory evolution of kinetic energy which is characteristic of mode-1. With increasing M_{g0}, the amplitude of temporal oscillations increase while temporal frequency decreases. At late shear times, the overall growth (growth of mean of oscillations) show an inverse relationship with M_{g0}. With increasing initial gradient Mach number, growth of mean kinetic energy decreases and eventually become lower than incompressible. Therefore, oblique modes with larger solenoidal component (large β) have lower mean kinetic energy than the incompressible counterpart.

Evolution of kinetic energy for oblique modes with larger dilatational component ($\kappa_x > \kappa_z$, small β) is shown in Fig. 4.13(b). In incompressible flows, dilatational modes (mode-1) decay in time. We see that the kinetic energy of oblique modes, in the incompressible regime (small M_{g0}), decays in time which is consistent with the observed behavior for dilatational modes in the similar regime. With increase in M_{g0} the growth in kinetic energy increases. All oblique modes with high enough gradient Mach number $M_{g0} > 1$ follow Burgers growth at small shear times. Modes with higher M_{g0} follow Burgers for a longer time but all oblique modes eventually

depart from Burgers evolution and show an oscillatory growth of kinetic energy typical of mode-1. Therefore, kinetic energy of oblique modes with higher dilatational component (small β) increases with increasing M_{g0}.

M_{g0} is the parameter for the effect of compressibility. With increasing effect of compressibility (or increasing M_{g0}) the behavior of oblique mode is dependent on ratio of amount of inherent solenoidal to dilatational component in the mode. When dilatational component is higher, increasing compressibility has a destabilizing effect. When solenoidal component is higher increasing compressibility has a stabilizing effect. We observe that the overall kinetic energy associated with oblique modes having higher solenoidal component is significantly higher (~ 5 times) than its counterpart having larger dilatational component. Therefore it is easy to conclude that in simulations of 'collective behavior', oblique modes with larger solenoidal content dictate the overall growth of kinetic energy at late shear times. Since oblique modes overall show a stabilizing effect of compressibility, they form an important basis for explanation of reduced growth of kinetic energy in the studies of 'collective behavior'.

Critical angle: β_{crit}

In Eq. (4.3.1), we discussed the critical angle β_{crit} for oblique modes. Kinetic energy of oblique modes with $\beta > \beta_{crit}$ grows and those with $\beta < \beta_{crit}$ decays in time. In Fig. (4.14), we show growth of kinetic energy for oblique modes around β_{crit} for $M_{g0} = 5$ and 10. We see that kinetic energy for oblique mode with $\beta = \beta_{crit}$, shows oscillations but the mean does not grow. For modes with $\beta > \beta_{crit}$, kinetic energy shows a clear trend of growth. For $M_{g0} = 5$ and 10, β_{crit} is 78.463° and 84.26°, respectively.

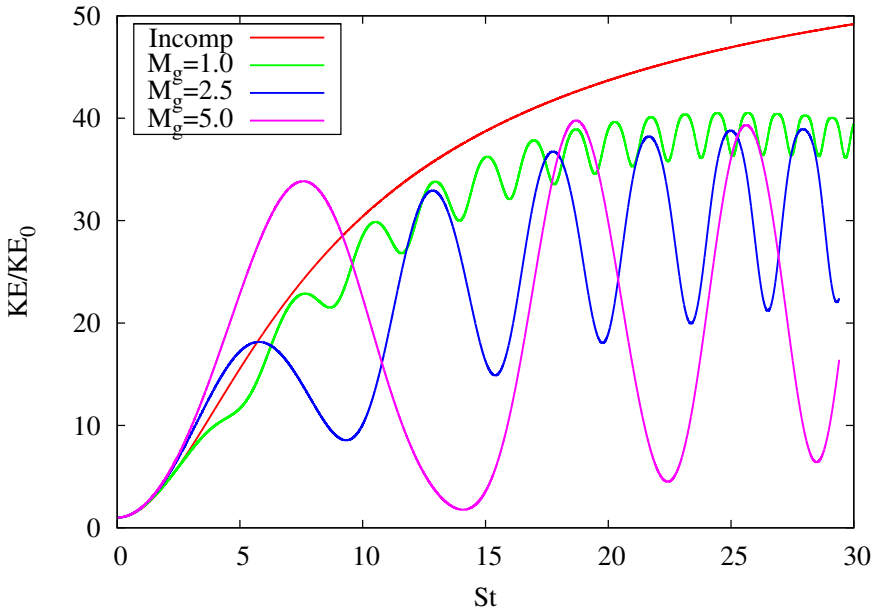

(a)

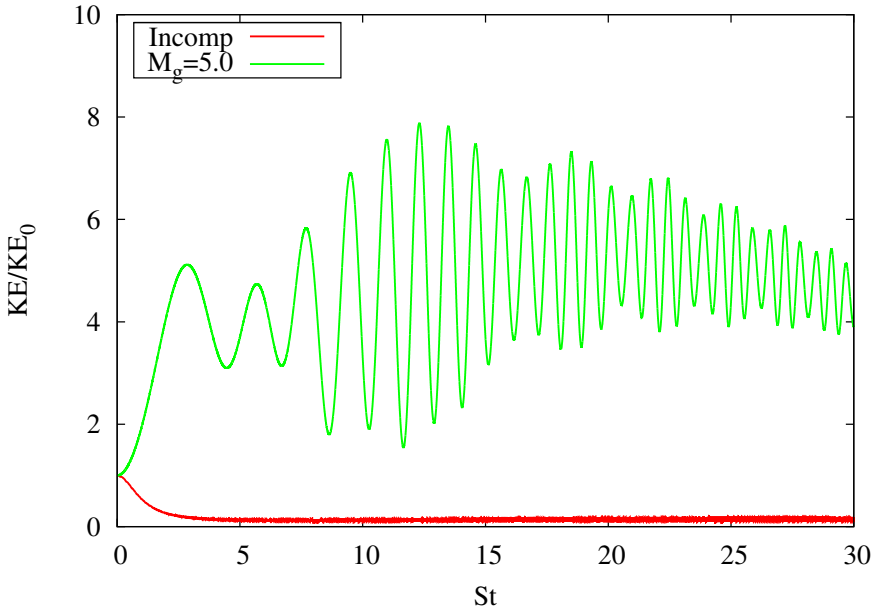

(b)

Fig. 4.13. Growth of kinetic energy for oblique modes: (a) $\beta = 78.69°$, (b) $\beta = 11.31°$

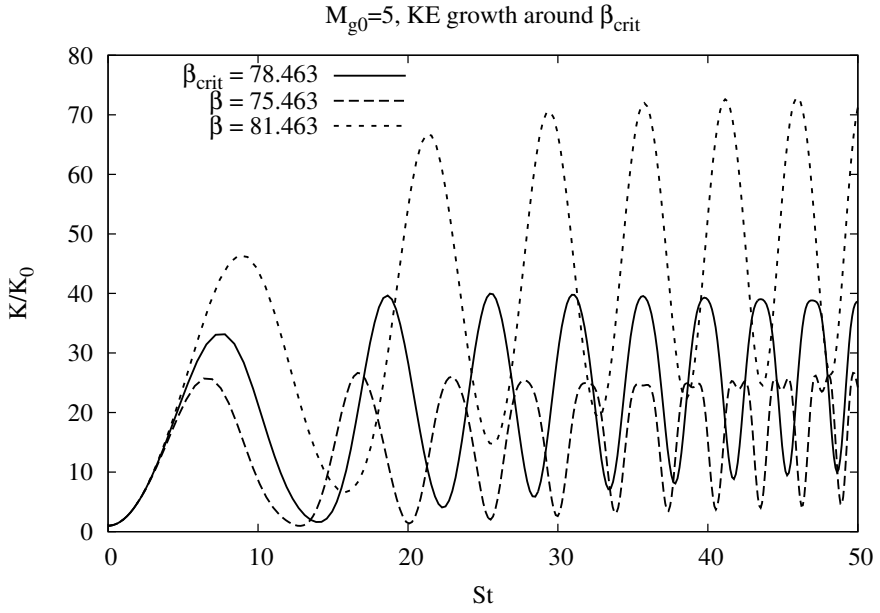

(a)

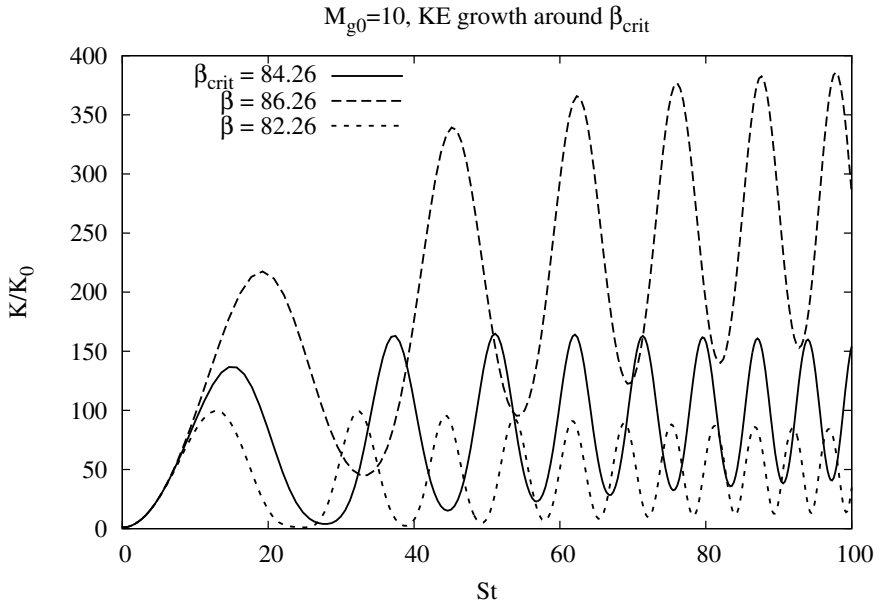

(b)

Fig. 4.14. Evolution of kinetic energy for oblique modes around β_{crit}: (a) $M_{g0} = 5$, (b) $M_{g0} = 10$.

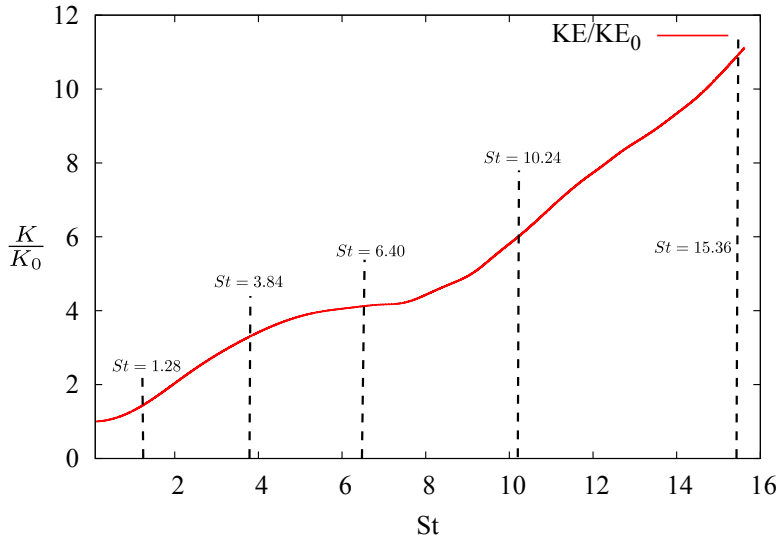

Fig. 4.15. Kinetic energy evolution for collection of modes for $M_g = 10, Re_\lambda = 15$

4.4 Role of Pressure in Collective Behavior

Using modal studies we have characterized the behavior of pressure and studied it's effect on the evolution of kinetic energy of individual modes. We now explain the three-stage behavior observed in DNS and RDT simulations of 'collection of modes' using the modal understanding. First we analyze the wave-content of velocity field in DNS of collective behavior. In order to understand the wave content of the velocity field at different stages of evolution in, we transform the physical space velocity field to Fourier space. We perform DFT on the velocity field for the case $M_{g0} = 10$ and $Re_{\lambda 0} = 15$ at various shear times as shown in Fig. 4.15: $St = 0.0$ (random, isotropic velocity field at $t = 0$), $St = 1.28$ (in stage-1), $St = 3.84$ (beginning of stage-2), $St = 6.40$ (in stage-2), $St = 10.24$ (early stage-3) and $St = 15.36$ (late stage-3). The DFT yields kinetic energy as a function of wave-number $(\kappa_x, \kappa_y, \kappa_z)$

$$E(\kappa_x, \kappa_y, \kappa_z) \equiv E(\kappa) = \frac{1}{2}\hat{u}(\kappa)\hat{u}^*(\kappa) \tag{4.7}$$

We study the distribution of energy in the plane normal to the shear (x-z plane) in Fig. (4.16). The x-z plane contains the most energetic modes–solenoidal, dilatational and oblique modes. For any given (κ_x, κ_z) we add the energies of modes with $\kappa_y \in [-3, 3]$, for all such modes are close to the x-z plane and have significant energy. The kinetic energy is initially distributed isotropically in the x-z plane. With time, we observe a decay in energy of dilatational modes with large κ_x. Also, oblique modes with large dilatational components begin to decay. Very quickly only modes with large solenoidal component ($\beta > \beta_{crit}$) survive and contain most of the energy. Therefore, oblique modes with $\beta > \beta_{crit}$ dominate the flow at late shear times while dilatational modes have decayed. This shows a largely solenoidal or the incompressible nature at late shear times of the initially compressible shear field.

In the previous sections we studied the evolution of modes as a function of obliqueness and initial gradient Mach number in the three regimes for (a) inviscid Burgers, (b) incompressible (DNS/RDT), and (c) compressible (DNS). Based on the understanding gained in the previous sections, we divide β in three regimes as shown in Fig. (4.17) and compare the growth of modes in Burgers, incompressible RDT/DNS and compressible DNS. We now provide an explanation using Fig. (4.17) for: (a) the three-staged behavior observed in DNS of homogeneous shear and, (b) the role of different modes in different stages.

1. Stage-1

   (a) Burgers: All oblique modes grow isotropically with $k/k_0 = 1 + (St)^2$.

   (b) Incompressible: Oblique modes with β smaller than the 'incompressible no-growth line' decay. Growth rate of oblique modes with larger β increases with increasing β but remains lower than Burgers growth.

   (c) Compressible: For initial times, all modes have Burgers-like growth rate. Mode with $\beta = 0$ departs from Burgers growth first, marking the onset

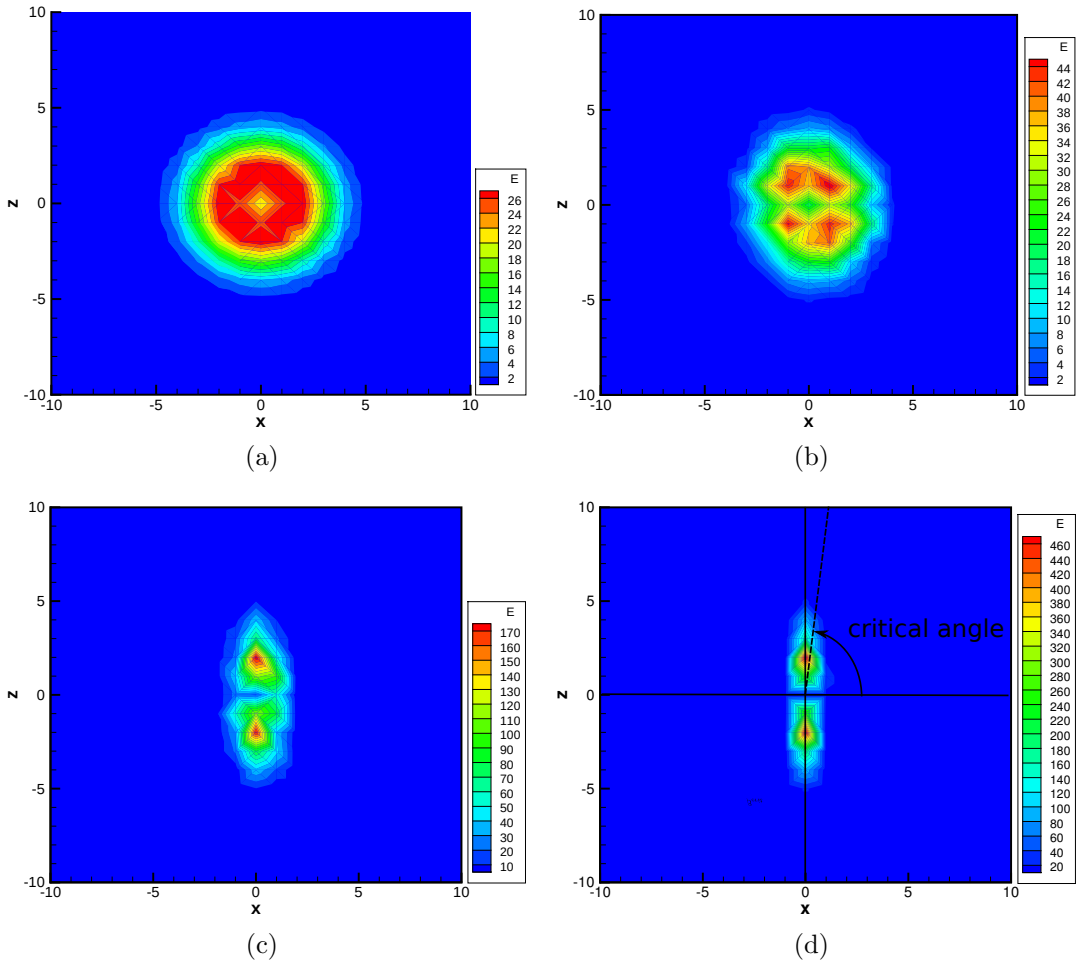

Fig. 4.16. Amplitude growth rate for different wave vectors: a) St=0.0, b) St=1.28, c) St=3.84, d) St=6.4

of stage-2. modes with higher β follows Burgers for a longer time but eventually depart from Burgers-growth.

(d) Result: Compressible follows Burgers growth while growth rate of incompressible is lower than compressible.

2. Stage-2

(a) Burgers: All oblique modes continue to grow isotropically with $k/k_0 = 1 + (St)^2$.

(b) Incompressible: Modes decaying in stage-1 continue to decay, while unstable modes grow monotonically with a growth rate increasing with increasing β. Mode with $\beta = \frac{\pi}{2}$ (solenoidal wave) has maximum kinetic energy (equal to Burgers).

(c) Compressible

i. The departure of purely dilatational mode $\beta = 0$ from Burgers marks the onset of stage-2. The mixed time for individual modes corresponding to the departure from Burgers is approximately 1.25. We observe a similar alignment in the point of departure from Burgers evolution in 'collective behavior' supporting the modal explanation for the initiation of stage-2.

ii. Oblique modes with higher β follow Burgers for a longer time but eventually depart from Burgers. We see an alignment of first peak of kinetic energy in mixed time $t^* = S^* t/\sqrt{M^*_{g0}}$.

iii. After departure from Burgers, kinetic energy of oblique modes decreases and then evolves with an oscillatory behavior. Kinetic energy of oblique modes with $\beta < \beta^*$ eventually decay in a long time while those with $\beta > \beta^*$ continue to grow.

iv. When an oblique mode departs from Burgers its kinetic energy decreases while the mode with next higher β continues to grow and the two kinetic energies (decay + growth) sum to give a flat profile.

v. The oscillations in stage-2 are mutually canceled due to phase and wavelength differences between various modes.

vi. For sufficiently high $\beta(\gtrsim 60$ kinetic energy of oblique modes becomes lower and stays lower after departure from Burgers. Oblique modes ($\beta > 45$) have kinetic energies an order of magnitude higher than those with smaller β. The kinetic energy of collective evolution in compressible regime eventually becomes lower than that of incompressible at late stage-2 because kinetic energy of oblique modes with large β becomes lower than that of incompressible.

vii. Oblique mode with $\beta = \beta^*$ departs from Burgers somewhere in mid stage-2 and starts to decay. This mode eventually starts growing marking the onset of stage-3.

3. Stage-3

(a) Burgers: All oblique modes continue to grow isotropically with $k/k_0 = 1 + (St)^2$.

(b) Incompressible: Kinetic energy of modes with large β dominate the overall growth in this stage. Effectively the overall growth is dominated by modes closer to the solenoidal mode.

(c) Compressible: Oblique modes with $\beta < \beta^*$ decay with a decay-rate faster for smaller β. Thus modes with large dilatational component die quickly. Those with large solenoidal component $\beta > \beta_{crit}$ continue to grow and since these modes have a largely solenoidal characteristic the overall growth in late third stage looks like-incompressible.

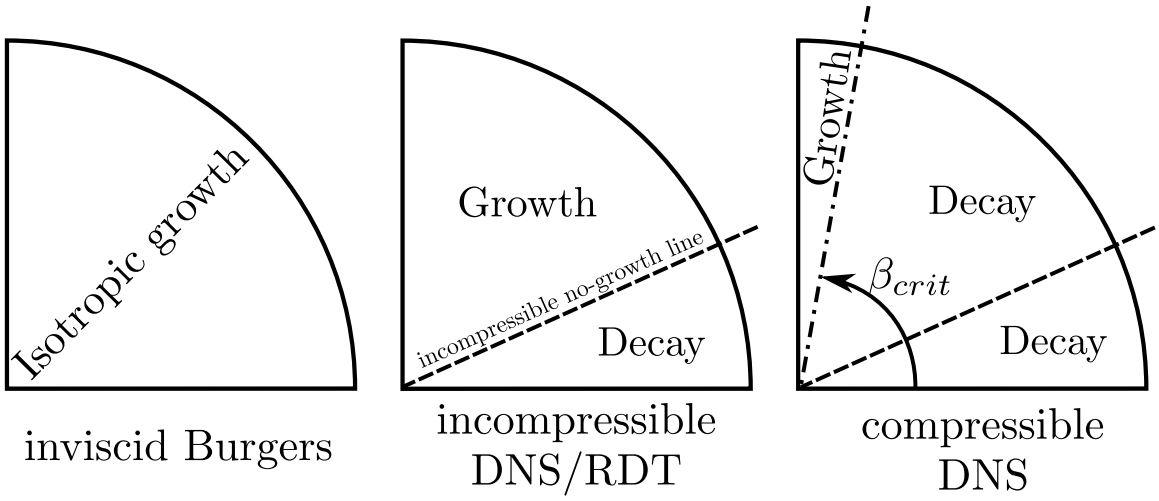

Fig. 4.17. Three stage behavior: Burgers, incompressible RDT and compressible DNS

4.5 Conclusions

The objective of this study is to examine the physics underlying the stabilizing influence of compressibility in high speed shear flows. The changing action of pressure at different Mach numbers is first established in the small perturbation limit and it is ultimately demonstrated that this leads to stabilization of the growth rate of kinetic energy.

The study commences with a linear analysis of the pressure perturbation equation and the behavior of pressure as a function of gradient Mach (M_g) and obliqueness angle (β). The analysis results in the identification of an effective gradient Mach number (Mg_0^*) that incorporates both Mach number and obliqueness effects. Further a critical obliqueness angle β^* is defined beyond which the effective gradient Mach number is less than unity. Linear analysis also indicates that the pressure perturbation frequency grows monotonically in time. The results of the linear analysis are confirmed by comparison against DNS data.

For a collection of Fourier modes we start our simulations with initially random, incompressible and isotropic velocity field without any thermodynamic fluctuations. We refer to the corresponding behavior as the 'collective-behavior'. The analysis of Fourier modes in isolation is referred to as the 'modal-behavior'. We discuss the three regimes observed in the 'collective-behavior' at high gradient Mach numbers and the relevance of time-scales of pressure and flow-field in the individual regimes. With an aim to explain the role of individual Fourier modes in bringing about the three-stage collective-behavior, we perform modal simulations for six initially incompressible modes, three initially compressible modes and oblique modes. The oblique modes are initially incompressible and are classified based on the ratio of the content of solenoidal to dilatational component or equivalently the angle β made with the direction of mean flow. The following observations are made in modal simulations:

1. Like incompressible flows, not all Fourier modes grow in the compressible regime. Of the 9 basic modes, only 3 modes grow: Mode 1, 6 and 9. Mode 1 and 6 are initially incompressible and most significant and are referred as the dilatational and solenoidal modes, respectively. Besides basic Fourier modes, oblique modes with varying component of solenoidal and dilatational content grow with growth dependent on the ratio of the solenoidal to dilatational content.

2. Growth of mode-1 increases with an increase in initial gradient Mach number. While fluctuation Mach number has no effect on growth of mode-1 at initial times, it decreases the growth rate at late times due to the larger viscous effect. Mode-1 has large dilatation field and compressible dissipation and negligible solenoidal dissipation and enstrophy.

3. Mode-6 has no effect of initial modal gradient Mach number and fluctuation Mach number. Mode-6 has negligible dilatation and compressible dissipation but large solenoidal dissipation and vorticity.

4. Oblique modes with larger solenoidal content show decrease in kinetic energy with increasing modal gradient Mach number at late shear time. oblique modes with larger dilatational content show an increased growth of kinetic energy with increasing M_{g0}.

5. Kinetic energy of oblique modes with $\beta > \beta_{crit}$ grows and those with $\beta < \beta_{crit}$ decays in time.

6. We see an scaling in kinetic energy and pressure in mixed time $t^* = S^* t/\sqrt{M^*_{g0}}$ or equivalently the local acoustic time.

7. Pressure plays a significant role in evolution of mode-1 while in mode-6 role of pressure is absent. We discuss the scaling of 'frequency of pressure'for dilatational mode at early and late shear times.

We finally explain the three-staged behavior observed in the ‘collective’ DNS cases using the behavior of individual modes in different stages.

5. VELOCITY THERMODYNAMICS INTERACTION IN HIGH SPEED SHEAR FLOWS: MODAL ANALYSIS OF POSSIBLE CONTROL STRATEGIES

5.1 Introduction

Controlling the onset and growth of turbulence has been one of the key focuses in engineering applications of fluid flows. The requirement for controlling turbulence becomes even more critical in applications involving high Mach and Reynolds numbers. Development of hypersonic vehicles faces two critical challenges directly related to fluid flow in and around the vehicle: (i) generation of tremendous amount of heat in the boundary layer due to shock, shock-boundary layer interaction and turbulence, thus subsequent heat flux to the body of the vehicle, (ii) poor combustion due to a reduced mixing and small resident time of the flow inside the combustor. Therefore, in hypersonic flows where turbulence critically controls the heat flux to the flight vehicle and mixing inside the combustor (besides mass flux in the engine, drag and noise), the demand for turbulence-control strategies becomes even more important. Control strategies are sought for: (a) delaying the transition to turbulence by extending the transition zone, (b) reducing turbulence intensity, thereby reducing the convective heating inside the boundary layer, (c) enhancing micro mixing by increasing turbulence intensity which in-turn facilitates combustion and subsequent heat generation, (d) reducing drag, (e) augment/minimize mass/heat transfer, (f) control pressure fluctuations (sound and pseudo-sound), and (g) delay flow separation.

Historically there has been more focus on turbulence closure compared to the control aspect of turbulence [111]. But the last two decades have witnessed an increased interest in the scientific community in turbulence control mechanisms. But till date, most of the fundamental studies and control strategy formulation have focussed on incompressible flows. Some of the important advances in turbulence-control are reviewed in [112–114]. Control strategies in turbulence can be broadly classified into active and passive methods. Active control schemes involve adding

energy (mostly unsteadily) to the flow, with or without a feedback loop. Few active control schemes are: controls based on predefined motion of actuators, unsteady mass injection/removal from the boundary layer through the wall. Passive methods of flow control do not feed/exchange energy in/with the flow. Riblets [115], deformable walls [116] are examples of passive control.

Design of control strategies for high speed and highly compressible flows, esp. hypersonic flows, poses additional challenges because fluid flows in such regimes are not fully understood. Compressibility introduces new flow-physics which makes studying turbulence more complicated than incompressible, for e.g. (i) relaxation of the incompressibility constraint, $\nabla \cdot \mathbf{u} = 0$, (ii) introduction of additional degrees of freedom in terms of permissible Fourier modes constituting the flow, (iii) a stabilizing effect in the normalized growth rate of turbulence, (iv) drastic change in the behavior/action of pressure, (v) appearance of additional terms in evolution equations – like pressure-dilatation in evolution equation of turbulent kinetic energy which exchanges energy between the internal and mechanical modes. But compressibility also opens new avenues for novel control strategies. Since in highly compressible flows, the acoustic timescale becomes comparable to the flow timescale, control strategies based on pressure/acoustics can be used. Also, a strong coupling between energy and momentum equation allows application of thermodynamics in design of control strategies. Important physical tendencies such as the equipartition of energy between the dilatational kinetic energy and potential energy of turbulence (resident in $p'^d p'^d$) can be used in design of control mechanisms. The aim of the current work is to demonstrate a proof-of-concept for thermodynamics/acoustics based strategies for control applications in compressible turbulence.

5.1.1 Background and motivation

One of the prominent features of compressibility is its stabilizing effect on the growth of turbulence. In experiments of high speed mixing layers, the normalized

spreading rate (normalized by incompressible spreading rate) decreases with increasing relative Mach number. At low relative Mach numbers, the spreading rates are similar to incompressible values but decrease significantly with increasing relative Mach number. Stabilizing effect of compressibility has also been observed in experiments of high speed (hypersonic) transition layers wherein the transition zone is prolonged compared to incompressible [96–99]. In simple canonical flows, like homogeneous shear flows, wherein the underlying physics is very similar to that in mixing and boundary layers, a similar stabilizing effect is observed. In RDT simulations of compressible homogeneous shear, Lavin *et. al* [78, 95] find that the evolution of kinetic energy exhibits three distinct stages/phases characterized by role of pressure. The three distinct stages of growth shown in Fig. 5.1(a) are: (i) stage-1: pressure-released phase where pressure effects are negligible compared to inertia and growth rate (of kinetic energy) is faster than incompressible in shear time (St); (ii) stage-2: acoustic/wave character stage where acoustic/wave nature of pressure is evident and growth rate slows down to a plateau and eventually becomes lower than incompressible; (iii) stage-3: incompressible-like stage where the growth rate of kinetic energy is similar to the incompressible counterpart. In stage-2, where acoustic timescale becomes comparable to flow timescale, growth is dominated by acoustic waves. Therefore pressure plays a critical role in the evolution of kinetic energy in stage-2 through the pressure-strain correlation and pressure dilatation terms.

The behavior and role of pressure changes as we move from incompressible to compressible regime. Depending upon the gradient Mach number, shear flows vary between two extreme limits: (i) incompressible limit ($M_g \approx 0$), where pressure maintains the incompressibility condition ($\nabla \cdot \mathbf{u} = 0$), (ii) Burgers limit ($M_g \to \infty$), where pressure plays no role. Within these two limits, at high enough M_g, there is a complex interplay between pressure and inertia. The role played by pressure varies with increasing compressibility. In incompressible flow, pressure maintains continuity or a divergence-free velocity field. It evolves according to the pressure Poisson

equation–an elliptic equation in space. Also in this regime pressure has a mechanical interpretation and is not a thermodynamic variable. However, in compressible flows pressure becomes a thermodynamic variable. In this regime, pressure has an acoustic nature and evolves according to the wave equation. With increasing compressibility, pressure and inertia effects start competing. In flows where the fluid time scale is small compared to acoustic time scale, inertia dominates. While pressure takes time to react to inertia, incompressibility is violated, leading to build-up of compressibility. When the acoustic time scale becomes comparable to the fluid time scale, role of pressure becomes increasingly significant and a marked change (slow down) in growth rate is observed. The wave nature of pressure and its strong coupling with the velocity field has a profound effect in stage-2 of compressible flows.

A key role played by pressure in stage-2, which is dominated by flow-thermodynamics interactions, opens up new avenues for the formulation of novel control strategies for controlling turbulence. Such control strategies can have foundations in the energy equation and exploit the strong coupling between momentum and energy balance equations. In Fig. 5.1(b), we explore different ways of controlling stage-2 for delaying the onset of turbulence.

1. *Reduction of kinetic energy*: If the kinetic energy of fluctuations can be reduced in the second stage, an overall supression in kinetic energy in stage-3 can be achieved. Therefore the 'controlled' shear flow would take longer to reach the kinetic energy threshold and thus delay the onset of turbulence. In boundary and mixing layers, it would mean an extension in the transition zone before the flow becomes fully turbulent.

2. *Extension of the stage*: If the second stage can be extended, with or without a reduction in kinetic energy, it would take longer for the fluctuations to reach the cut-off limit for the onset of turbulence in stage-3.

Different methods of acoustic-thermodynamics based control can be used to achieve extension or delay (or a combination) of growth of kinetic energy in stage-2 to control the onset of turbulence. Each strategy exploits different aspect of the flow-thermodynamics interaction. In this work we use 'equi-partition of kinetic and potential energy' observed in the second stage of growth of kinetic energy in homogeneously sheared flow to bring about the proposed control.

In compressible homogeneous shear flows, an equi-partition of energy is observed between the dilatational kinetic energy and the potential energy of fluctuations. The so-called potential energy of turbulence resides in the fluctuating dilatational pressure ($\overline{p'^d p'^d}$) and exchanges energy with dilatational kinetic energy ($\overline{u'^d u'^d}$) through the pressure dilatation term $\overline{p'd'}$. In Fig. (5.2) we describe the equi-partition and ways in which it can be used for controlling the onset of turbulence through a *two-tank* analogy. Compressibility is like a valve controlling the flow between two separate tanks containing potential energy of turbulence (fluctuating internal energy) and dilatational kinetic energy. The exchange of energy takes places through pressure-dilatation which is the pipe connecting the tanks. The valve of compressibility sits on top of the connecting pipe. In incompressible flows, the valve is fully closed and there is no-exchange of energy. In highly compressible regimes, the valve is fully open thus allowing an exchange of energy between the two tanks. The pressure-dilatation works to maintain an equal level of energy in both tanks. Now, if we devise a control mechanism to drain energy from either of the tanks, the level in other tank would also come down. The internal energy and therefore potential energy of turbulence can be drained through endothermic reactions while kinetic energy can be drained through the body forces. We can mimic the effect of chemical reactions draining the internal energy through a change in transport coefficient namely, the Prandtl number. When internal energy is drained, $\overline{p'^d p'^d}$ reduces. The pressure dilatation transfers energy from kinetic mode ($\overline{u'^d u'^d}$) to compensate the reduction in $\overline{p'^d p'^d}$. This leads to a reduction in dilatation kinetic energy. Since, the production of

turbulence in homogeneous shear is highly dependent on the dilatational component of velocity field, a reduction in dilatational kinetic energy reduces the overall kinetic energy and its subsequent growth.

The objective of this study is to demonstrate acoustic based novel flow control strategies in highly compressible shear flows and provide a modal-analysis based insight in the flow physics. Towards this end, we perform direct numerical simulations with the following aims:

1. Study the effect of change in Prandtl number on the growth of kinetic energy especially in acoustic dominated second stage.

2. Examine the effect of change in Prandtl number on growth of straight and oblique modes. We also aim to investigate the behavior of equipartition function for different Fourier modes.

3. Provide a modal understanding based explanation of control strategy in bringing about a delay in the onset of turbulence.

5.2 Governing Equations and Numerical Setup

We perform DNS for studying the evolution of turbulent fluctuations in homogeneous shear for different Prandtl numbers. The parameters characterizing a homogeneous shear flow setup, are the initial gradient Mach number (M_{g0}), initial turbulent Mach number (M_{t0}) and initial Taylor micro-scale Reynolds number ($Re_{\lambda 0}$) defined as:

$$M_{g0} = \frac{Sl_0}{\sqrt{\gamma RT_0}}, \quad M_{t0} = \frac{\overline{u_i' u_i'}}{\sqrt{\gamma RT_0}}, \quad Re_{\lambda 0} = \frac{\overline{u_i' u_i'}}{\mu\sqrt{\omega'\omega'}} \tag{5.0}$$

where S is the shear-rate of the mean flow field, l_0 is the relevant lengthscale of the problem. The gradient of the mean velocity field is given by $\bar{U}_{i,j} = S\delta_{i1}\delta_{2j}$. The lengthscale l_0 is related to initial integral lengthscale of the fluctuating field u'.

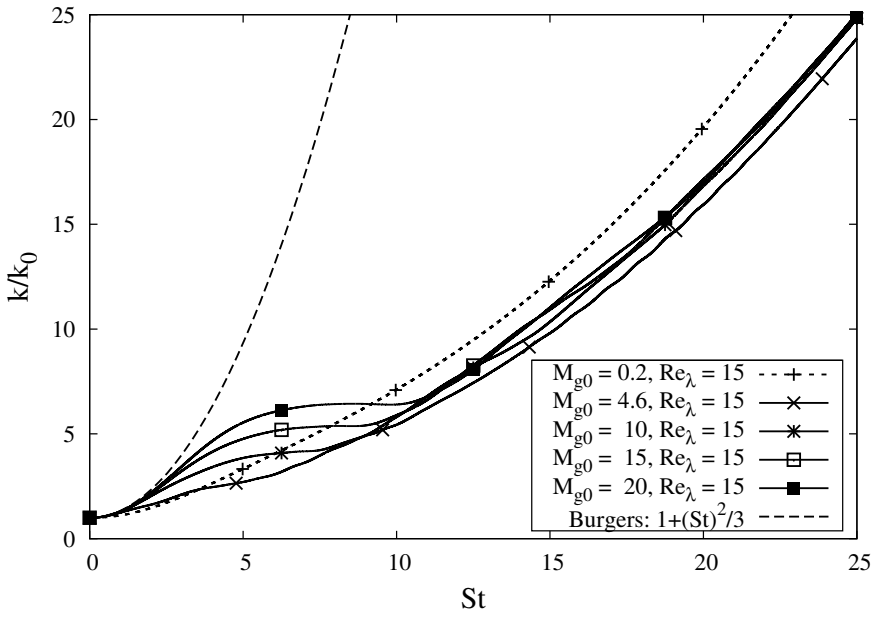

(a)

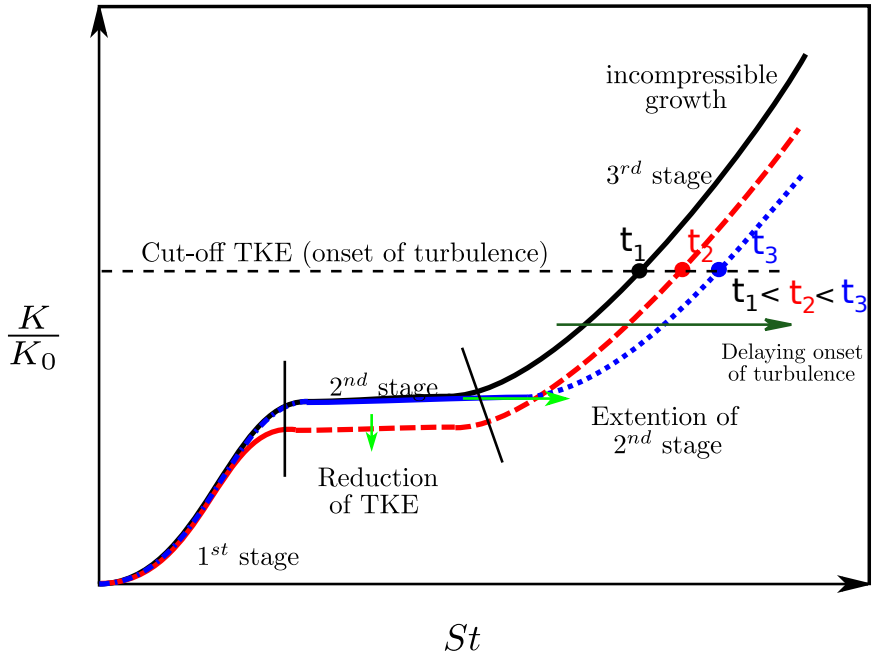

(b)

Fig. 5.1. Evolution of normalized kinetic energy (k/k_0) for collective behavior in shear flows in: a)shear time, b) schematic diagram showing different ways of delaying the onset of turbulence.

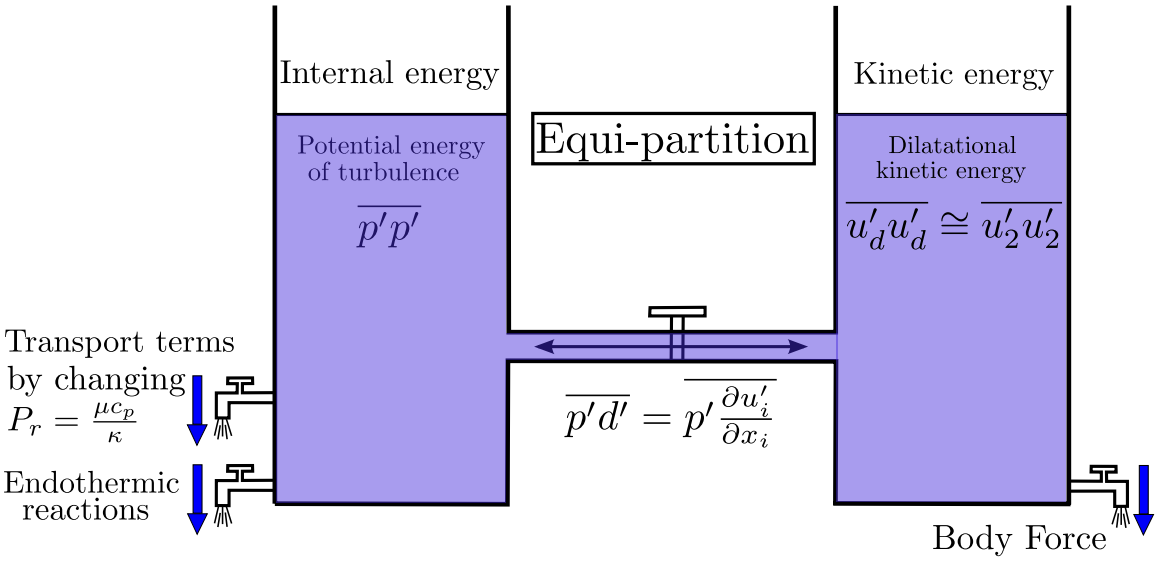

Fig. 5.2. Schematic for possible control mechanisms which are based on the 'equipartition of energy'.

5.2.1 Governing equation

The Navier-Stokes equations governing the flow are

$$\begin{aligned}
\frac{\partial \rho}{\partial t} + \frac{\partial(\rho u_i)}{\partial x_i} &= 0, \\
\frac{\partial(\rho u_i)}{\partial t} + \frac{\partial(\rho u_i u_j + p\delta_{ij})}{\partial x_j} &= \frac{\partial \sigma_{ij}}{\partial x_j}, \\
\frac{\partial E}{\partial t} + \frac{\partial[(E+p)u_i]}{\partial x_i} &= \frac{\partial(\sigma_{ij}u_j)}{\partial x_i} - \frac{\partial}{\partial x_i}\left(\kappa_t \frac{\partial T}{\partial x_i}\right).
\end{aligned}$$

The viscous stress tensor σ_{ij} is given by a constitutive relation

$$\sigma_{ij} = \mu\left[\frac{\partial u_i}{\partial x_j} + \frac{\partial u_j}{\partial x_i} - \frac{2}{3}\delta_{ij}\frac{\partial u_k}{\partial x_k} + \eta\delta_{ij}\frac{\partial u_k}{\partial x_k}\right],$$

where μ is the dynamic viscosity coefficient, κ_t is the thermal conductivity, η is the bulk viscosity and γ is the ratio of specific heat coefficients.

The evolution equation for turbulent kinetic energy in homogeneous shear flows derived by Favre averaging [79, 80] the instantaneous momentum equation (5.2.1) is

$$\frac{dK}{dt} = P - \epsilon_s - \epsilon_c + \frac{\overline{p'd'}}{\bar{\rho}}, \tag{5.0}$$

where $K = \frac{1}{2}\widetilde{u_i u_i} = \frac{1}{2}\overline{\rho u_i' u_i'}/\bar{\rho}$ is the Favre averaged turbulent kinetic energy (TKE), $P = -S\widetilde{u_1' u_2'}$ is the production of TKE, $\epsilon_s = \bar{\nu}\overline{\omega_i'\omega_i'}$ is the solenoidal dissipation rate, $\epsilon_c = \frac{4}{3}\bar{\nu}\overline{d'^2}$ is the compressible/dilatational dissipation rate and $\overline{p'd'}$ is the pressure dilatation. Here $d' = u_{i,i}'$ is the fluctuating velocity dilatation, ω' is the fluctuation in vorticity ($\nabla \times \mathbf{u}$), $p' = \left(\rho'\overline{T} + \rho' T' + \overline{\rho} T' - \overline{\rho' T'}\right) R$ is the fluctuation in pressure and R is the gas constant. The pressure field can be decomposed into mean pressure, fluctuating incompressible and compressible pressure as $p = \bar{p} + p^{I'} + p^{C'}$. The component of pressure associated with the incompressible velocity field is given as

$$\nabla^2 p^{I'} = -2\bar{\rho} S u_{2,1}^{I'} - \bar{\rho} u_{i,j}^{I'} u_{j,i}^{I'}. \tag{5.0}$$

The fluctuating velocity field can be decomposed on incompressible and compressible components ($u' = u^{I'} + u^{C'}$) through the Fourier transformation as

$$\hat{u}^{C'} = \hat{u} \cdot \kappa; \quad \hat{u}^{I'} = \hat{u'} - \hat{u} \cdot \kappa \tag{5.0}$$

where $\hat{u}$ is the Fourier amplitude of the velocity field.

5.2.2 Computational domain and boundary conditions

The computational domain is a cubic box of dimension $l = 2\pi$. The box is discretized into $N_x \times N_y \times N_z$ cells with $N_x = 256, N_y = 512$ and $N_z = 256$ along the x, y and, z directions respectively. We apply uniform shear in u_1 along the x_2 direction such that the gradient of the mean flow field is $\bar{U}_{i,j} = S\delta_{i1}\delta_{2j}$ with S as the shearing rate. Periodic boundary conditions are applied for boundaries normal to the stream-wise (x_1) and span-wise/stream-normal (x_3) directions. For boundaries normal to the direction of shear (x_2), we apply shear-periodic boundary condition [82–85,]

$$\phi(t, x + m_1 L_x, y + m_2 L_y, z + m_3 L_z) = \phi(t, x - S m_2 L_y t, y, z), \tag{5.0}$$

where L_x, L_y and L_z are the dimensions of the box along the three co-ordinate directions and m_1, m_2, m_3 are arbitrary integers. Along the direction of shear, only the fluctuating component of velocity is periodic while the mean velocity is specified to maintain the prescribed shear S.

5.3 Results and Discussion

In this section we present a modal-analysis based explanation of the effect of change of Prandtl number on the statistical behavior of collection of modes. We

start with a description of modal-analysis and provide details of different individual modes studied.

5.3.1 Modal analysis

Any general three dimensional flow field can be visualized as a summation or collection of Fourier modes. We refer to the statistical behavior of this flow field (which is a collection of waves/modes) as the 'collective' behavior. In order to explain the role played by different Fourier modes in bringing about the collective behavior, we investigate the evolution of individual modes in isolation. We refer to this analysis of Fourier modes as 'modal analysis' (not to be confused with similar terminology used in stability analysis). Since the initial condition for *collective behavior* is divergence-free, we consider all possible modes that satisfy $\nabla \cdot \mathbf{u} = 0$ in physical space or equivalently $\hat{\mathbf{u}} \cdot \vec{\kappa} = 0$ in Fourier space. The Cartesian axis is fixed such that shear is along the y axis and mean flow is along the x axis. This fixes the third axis z to be normal to the shear and mean flow direction. First, we consider only those modes whose direction of propagation is along the Cartesian axes. This, along with the incompressibility condition, yields six mutually independent and orthogonal family of *initially-incompressible* modes for investigation as given in Table 5.1.

As we will see in later sections, another important family of modes are those with direction of propagation in the plane normal to the direction of shear. We refer to such modes as 'oblique modes'. The oblique modes are charaterized by the angle β it makes with the stream-wise direction (x_1) and its amplitude. A typical oblique mode can be represented as

$$\vec{u} \equiv (u, v, w) = (0, \sin(mx + nz + \Delta), 0), \quad \Delta \in [0, \pi], \tag{5.0}$$

	Fourier space		**Physical space**			
	$\vec{k}$	$\hat{\mathbf{u}}$	u	v	w	Fig.
Mode 1	(1,0,0)	(0,1,0)	0	$\sin(nx + \Delta)$	0	5.3(a)
Mode 2	(1,0,0)	(0,0,1)	0	0	$\sin(nx + \Delta)$	5.3(b)
Mode 3	(0,1,0)	(1,0,0)	$\sin(ny + \Delta)$	0	0	5.3(c)
Mode 4	(0,1,0)	(0,0,1)	0	0	$\sin(ny + \Delta)$	5.3(d)
Mode 5	(0,0,1)	(1,0,0)	$\sin(nz + \Delta)$	0	0	5.3(e)
Mode 6	(0,0,1)	(0,1,0)	0	$\sin(nz + \Delta)$	0	5.3(f)

Table 5.1

Mutually independent, initially incompressible family of modes studied in isolation, where ($n \in [1, 2, 3, \ldots]$) is the wavenumber and the phase shift is given by $\Delta \in [0, \pi]$.

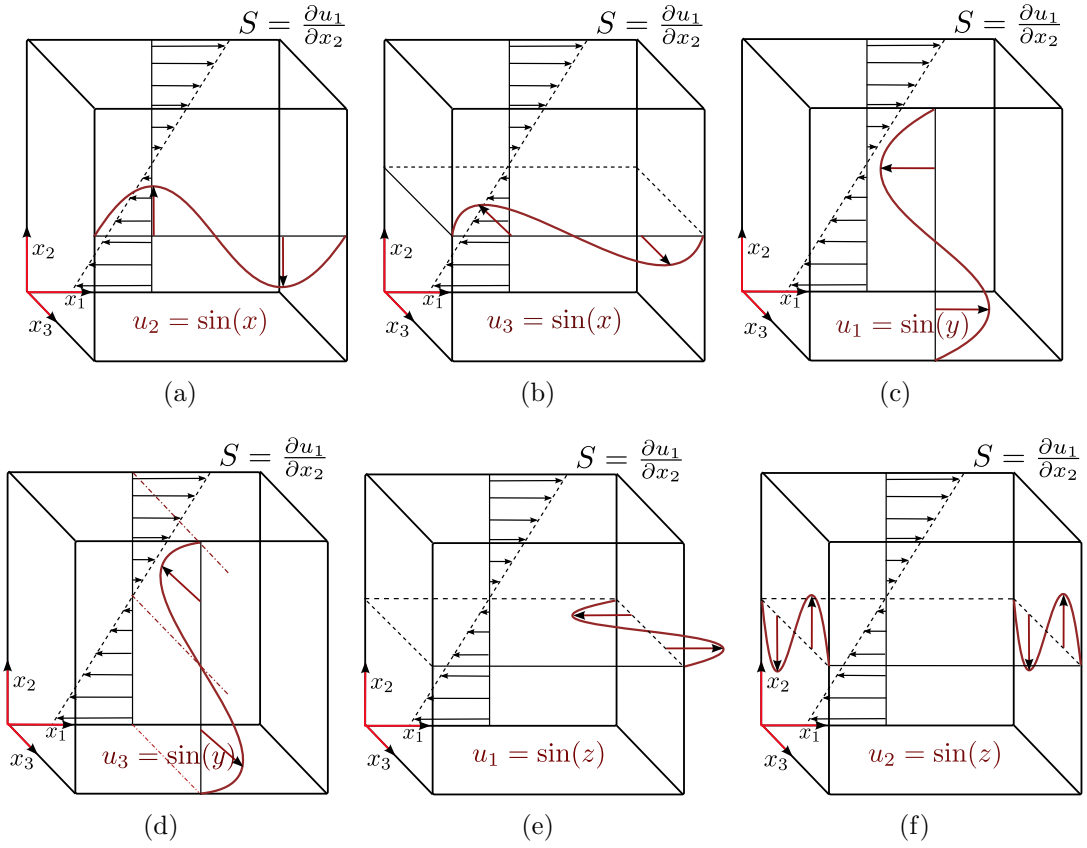

Fig. 5.3. Modal analysis: schematic diagram (not to scale) of the computational setup for different Fourier modes in homogeneous shear flow ($S = \frac{\partial \overline{U}}{\partial y}$) (a) Mode 1 (dilatational mode): $(u, v, w) = (0, \sin(nx + \Delta), 0)$, (b) Mode 2: $(u, v, w) = (0, 0, \sin(nx + \Delta))$, (c) Mode 3: $(u, v, w) = (\sin(ny + \Delta), 0, 0)$, (d) Mode 4: $(u, v, w) = (0, 0, \sin(ny + \Delta))$, (e) Mode 5: $(u, v, w) = (\sin(nz + \Delta), 0, 0)$ (f) Mode 6 (solenoidal mode): $(u, v, w) = (0, \sin(nz + \delta), 0)$, where $\Delta \in [0, \pi]$ is the phase shift and $n \in I$ is an arbitrary integer. For the above schematic, $\Delta = 0$ and $n = 1$ is chosen for demonstration purposes. All of the above modes are initially incompressible.

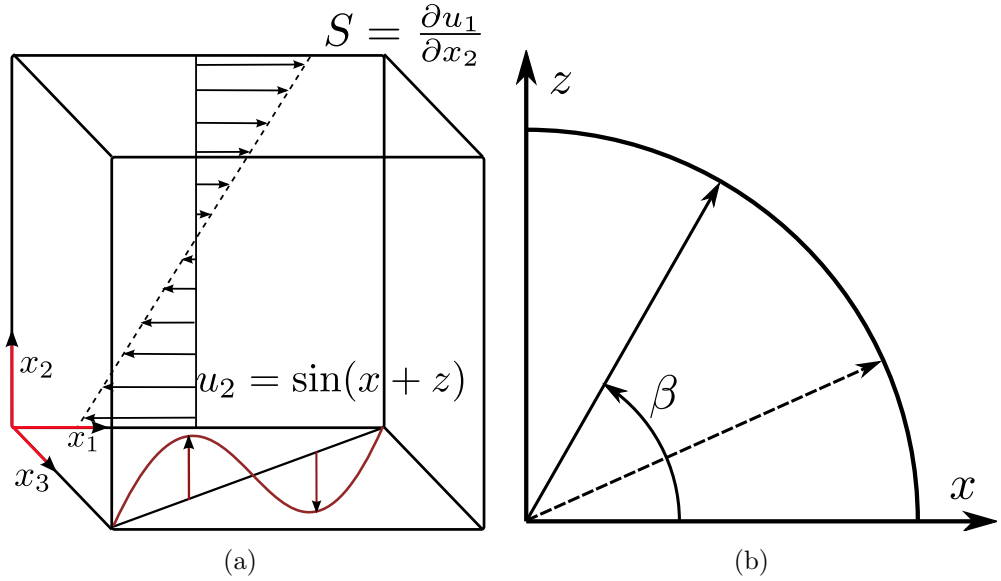

Fig. 5.4. Oblique modes: growth in incompressible compared to compressible case depend on direction of modes.

where $n \in I^+$ is the wavenumber and Δ is an arbitrary phase shift. In Fig. 5.4(a) we show a typical oblique wave along with the computational domain and the shear. Modes 1 ($\beta = 0$) and 6 ($\beta = \pi/2$) are limiting cases of oblique modes.

$$\beta = \tan^{-1}\left(\frac{\kappa_z}{\kappa_x}\right), \quad \text{where } \vec{\kappa} = (\kappa_x, \kappa_y, \kappa_z).$$

5.3.2 Equipartition of energy

In RDT analysis of homogeneous shear flows Lavin *et al.* [95] demonstrate a tendency of turbulence towards an equipartition of energy between dilatational component of kinetic energy and potential energy of turbulence. Dilatational component of velocity is the projection of the Fourier amplitude of velocity along the direction of wave vector: $\hat{\mathbf{u}}_d = \hat{\mathbf{u}} \cdot \vec{\kappa}$. At late shear times, the component of wave-vector along

the shear direction ($\kappa_2 = \kappa_2(0) - \kappa_1(0)St$) becomes increasingly large compared to other components ($\kappa_1 = \kappa_1(0), \kappa_3 = \kappa_3(0)$). In homogeneous shear, this makes the wave-vector $\vec{\kappa}$ to increasingly align along the shear-direction (x_2). Therefore u_2 becomes a good approximation of the dilatational component of kinetic energy at late times

$$\hat{\mathbf{u}}_d \equiv \mathbf{u}^{C'} = \hat{\mathbf{u}} \cdot \vec{\kappa} = \hat{\mathbf{u}} \cdot (\kappa_1(0), \kappa_2 = \kappa_2(0) - \kappa_1(0)St, \kappa_3(0))/|\kappa| \approx \hat{u}_2\kappa_2/|\kappa|. \quad (5.\text{-}1)$$

For sufficiently large St, $\overline{u_2 u_2}$ is a good approximation of the dilatational component of kinetic energy [109, 117]. Pressure, through the pressure-strain correlation, plays an important role in exchange of energy between mechanical and internal modes and in driving the two modes towards an equipartition. Since pressure is a thermodynamic variable in compressible flows, an equipartition of energy in compressible regime shows a key role played by flow-thermodynamic interactions.

The evolution equation for variance of pressure (potential energy of turbulence) [118] in compressible decaying turbulence and homogeneous shear is given by:

$$\frac{d}{dt}\left(\overline{p'p'}\right) = -2\gamma\bar{p}\overline{p'd'} - (2\gamma - 1)\,\overline{p'p'd'} - 2\epsilon_p + \varphi_p \quad (5.\text{-}1)$$

where $\varphi_p \ll \epsilon_p$ is a term depending on mean viscosity and conductivity, $\epsilon_p = (\gamma - 1)R\bar{\rho}\,\overline{\kappa_c}\,\overline{T'_{,j}T'_{,j}}$ is dissipation term for pressure variance and $d' = u'_{i,i}$ is the fluctuating dilatation.

The evolution equation for kinetic energy in homogeneous shear flow is given by

$$\frac{d}{dt}\left(\bar{\rho}K\right) = -S\bar{\rho}\widetilde{u''_1 u''_2} - \bar{\rho}\epsilon_s - \bar{\rho}\epsilon_d + \overline{p'd'} \quad (5.\text{-}1)$$

where ϵ_s and ϵ_d are the solenoidal and dilatational (compressible) dissipation, respectively. In Eq. (5.3.2) and (5.3.2), $\overline{p'd'}$ appears with opposite signs, therefore playing a role of exchange term. Pressure dilatation ($\overline{p'd'}$) transfers energy between

the kinetic energy ($\bar{\rho}K$) and potential energy of turbulence $\overline{p'p'}/(2\gamma\bar{p})$. Equations (5.3.2) and (5.3.2) can be linearized and analyzed in the context of viscous RDT. The linearized equation for variance of pressure is given by

$$\frac{d}{dt}\left(\overline{p'p'}\right) \approx -2\gamma\bar{p}\left(\overline{p'u'_{i,i}}\right) - 2\epsilon_p. \tag{5.-1}$$

The linearized equation for dilatational kinetic energy is given by

$$\frac{d}{dt}\left(\overline{u'_2u'_2}\right) \approx \frac{2}{\bar{\rho}}\left(\overline{p'u'_{2,2}}\right) - \epsilon_d. \tag{5.-1}$$

Since in the limit of viscous RDT, mean pressure does not grow significantly, $\bar{p}$ can be assumed to be a constant. Using the fact $\bar{\rho}$ is a constant and the assuming that $\bar{p}$ is also a constant, Eqs. (5.3.2) and (5.3.2) are reduced to the following equation

$$\frac{d}{dt}\left(\overline{u'_2u'_2} + \frac{\overline{p'p'}}{\gamma\bar{p}\bar{\rho}}\right) \approx -\frac{2}{\bar{\rho}}\left(\overline{p'u'_{1,1}} + \overline{p'u'_{3,3}}\right) - \epsilon_d - \frac{2}{\gamma\bar{p}\bar{\rho}}\epsilon_p. \tag{5.-1}$$

Integrating both sides with time and using initial conditions $\overline{p'p'}(t=0) = 0$ and $\overline{u'_2u'_2}(t=0) = \overline{u'_2u'_2}(0)$ we get

$$\left[\frac{\bar{\rho}}{2}\left(\overline{u'_2u'_2} + \frac{\overline{p'p'}}{\gamma\bar{p}\bar{\rho}}\right)\right](t) \approx \frac{\bar{\rho}}{2}\overline{u'_2u'_2}(0) - \int_0^t \left(\overline{p'u'_{1,1}} + \overline{p'u'_{3,3}}\right) dt - \int_0^t \left(\frac{\bar{\rho}}{2}\epsilon_d + \frac{1}{\gamma\bar{p}}\epsilon_p\right) dt \tag{5.-1}$$

In DNS performed in this work we observe that $\overline{p'u'_{1,1}} \gg \overline{p'u'_{3,3}}$ and $\overline{p'u'_{1,1}} < 0$. From Eq. (5.3.2) we see that the sum of dilatational kinetic energy and potential energy of turbulence increases due to $\int_0^t \overline{p'u'_{1,1}}dt$ and decreases due to $\int_0^t \left((\bar{\rho}/2)\epsilon_d + 1/(\gamma\bar{p})\epsilon_p\right) dt$. Thus the system of equations (5.3.2) and (5.3.2) mimics a forced harmonic oscillator with damping, where $\overline{p'u'_{1,1}}$ is the primary forcing term while $(\bar{\rho}/2)\epsilon_d$ and $1/(\gamma\bar{p})\epsilon_p$ are damping terms. The exchange term $\overline{p'u'_{2,2}}$ transfers energy between the dilatational and potential modes like a harmonic oscillator. The key point to be noted is that pressure-dilatation $\overline{p'd'}$ contains both the exchange and forcing term. Now we will

look into the ratio of dilatational kinetic energy and potential energy of turbulence to investigate equipartition of energy.

Starting with linearized equation for pressure and transverse velocity in inviscid RDT Bertsch *et al.* [101] derive the following relationship between variance of pressure and transverse (dilatational component of velocity) kinetic energy for homogeneous shear flows:

$$\frac{\overline{u_2' u_2'}}{\overline{p'p'}/(\bar{p}\gamma\bar{\rho})} = 1 \tag{5.-1}$$

They use the following observations made in [95], using RDT simulations for a range of initial modal Mach numbers, towards the late time asymptotic behavior of pressure-strain correlation tensor Π_{ij}:

$$\frac{\int_0^t \Pi_{22} dt}{\int_0^t \Pi_{11} dt} \approx -\frac{1}{2} \quad \text{and} \frac{\int_0^t \Pi_{33} dt}{\int_0^t \Pi_{11} dt} \approx 0. \tag{5.-1}$$

They show that for all initial modal Mach numbers, pressure fluctuations tend to equipartition with dilatational component of kinetic energy. In [95,101] equipartition has been shown in the context of inviscid RDT where viscous dissipation, inertial cascade and non-linearity is absent. In this section we will analyze equipartition of energy using DNS of compressible N-S for homogeneous shear flows.

We modify the equipartition relationship of Eq. (5.3.2) to

$$F_{equi} \equiv \frac{\overline{u_2' u_2'}}{\overline{u_2' u_2'} + \overline{p'p'}/(\bar{p}\gamma\bar{\rho})} = \frac{1}{2} \quad \text{at late } St, \tag{5.-1}$$

where we refer to F_{equi} as the equipartition function. In DNS of a 'collection of modes' in a homogeneous shear flow set-up, the equipartition function converges to ≈ 0.5 at late times as shown in Fig. (5.5). Similar partitioning tendency has been observed previously in DNS of decaying compressible homogeneous turbulence and of compressible turbulence in homogeneous shear by by Sarkar *et. al* [119] and Sarkar

et. al [118], respectively. The non-dimensional equipartition parameter is defined in [118, 119] as

$$F \equiv \frac{\gamma M_t^2 \chi}{p_c^2} \simeq 1 \tag{5.-1}$$

where $M_t = \frac{\overline{u_i u_i}}{\sqrt{\gamma R \bar{T}}}$ is the turbulent Mach number, χ is the ratio of compressible (dilatational) to total turbulent kinetic energy, and $p_c^2 = \overline{p^{C'^2}}/\bar{p}^2$ is the ratio of variance of compressible pressure to root-mean-square of the mean pressure.

Equipartition between the dilatational kinetic energy and potential energy of turbulence is also observed in DNS of the dilatational mode (mode-1, $\beta = 0$). Since the simulation involves a single wave (to begin with), physics underlying equipartition is revealed clearly. Equipartition is brought about by an exchange of energy between the dilatational velocity and compressible pressure through the pressure strain correlation. The transfer of energy is not uni-directional, instead resembles oscillatory exchange of energy between kinetic and potential modes as in a harmonic oscillator. In a harmonic oscillator F_{equi}-like term oscillates sinusoidally between 0 and 1 due to the exchange of energy between kinetic and potential modes. A similar oscillatory behavior is evident in the evolution of F_{equi} for the dilatational mode as shown in Fig. (5.6). It shows a clear exchange between $\overline{u_2' u_2'}$ and $\overline{p'p'}$ for pure dilatational mode. The exchange of energy evident in F_{equi} for the dilatational mode is masked in the collective behavior (Fig. 5.5). This is due to the cancellation of oscillations in the equipartition function (F_{equi}) due the phase differences between contributions from various modes. For a more physical picture, we present evolution of $\overline{u_2' u_2'}$ and $\overline{p'p'}/(\bar{p}\gamma\bar{\rho})$ in Fig. (5.7) for the DNS of the dilatational mode. It is clear that $\overline{u_2' u_2'}$ and $\overline{p'p'}$ are oscillatory and out of phase which is characteristic of harmonic oscillator. The initial increase in amplitude and a later decay is attributed to the forcing term $\overline{p' u_{1,1}'}$ and damping functions $(\bar{\rho}/2)\epsilon_d$, $1/(\gamma\bar{p})\epsilon_p$, respectively.

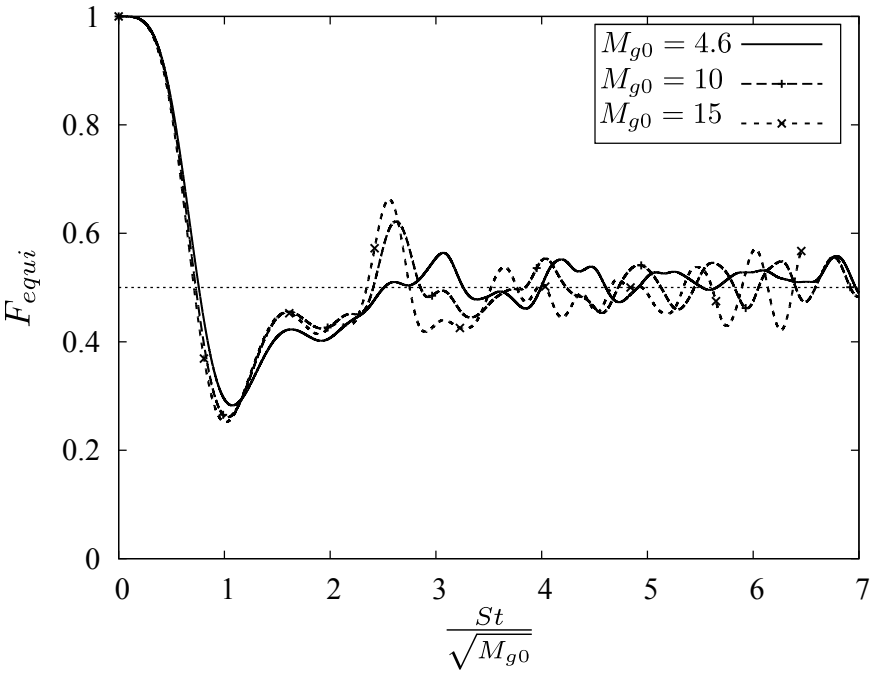

(a)

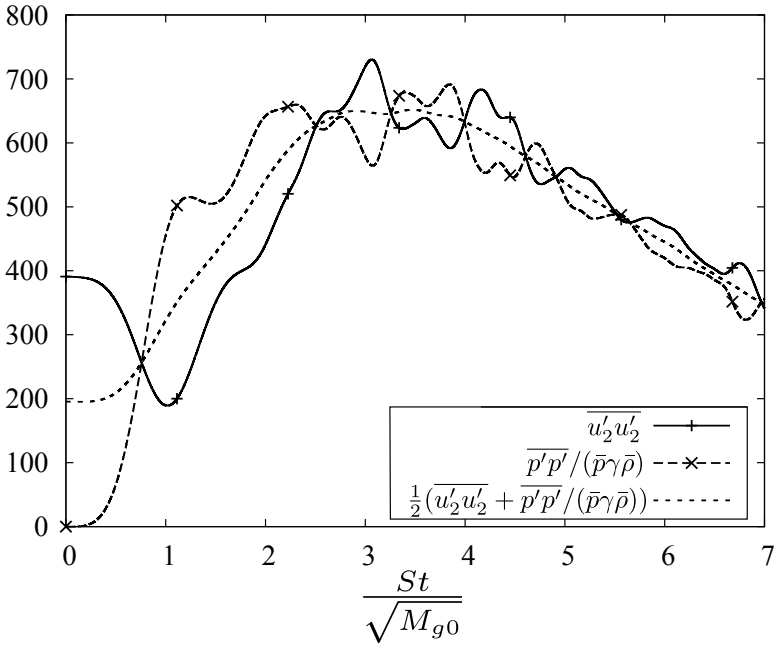

(b)

Fig. 5.5. DNS for collective behavior in homogeneous shear flow: (a) equi-partition function $F_{equi} = \overline{u_2'u_2'}/\left(\overline{u_2'u_2'} + \overline{p'p'}/(\bar{p}\gamma\bar{\rho})\right)$ for $M_{g0} = 4.6, 10, 15$ and $Re_{\lambda 0} = 15$, and (b) dilatational kinetic energy $(\overline{u_2'u_2'})$ and potential energy of turbulence $(\overline{p'p'}/(\bar{p}\gamma\bar{\rho}))$ for $M_{g0} = 5.0$ and $Re_{\lambda 0} = 15$.

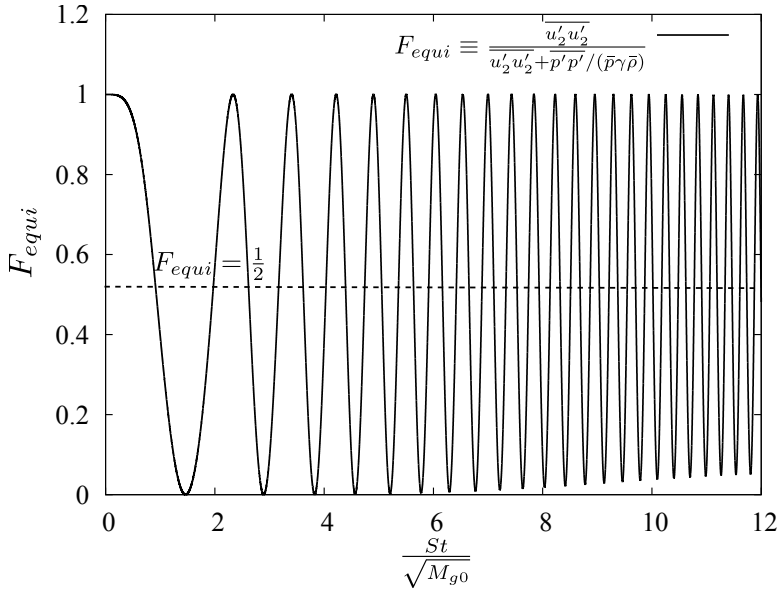

(a)

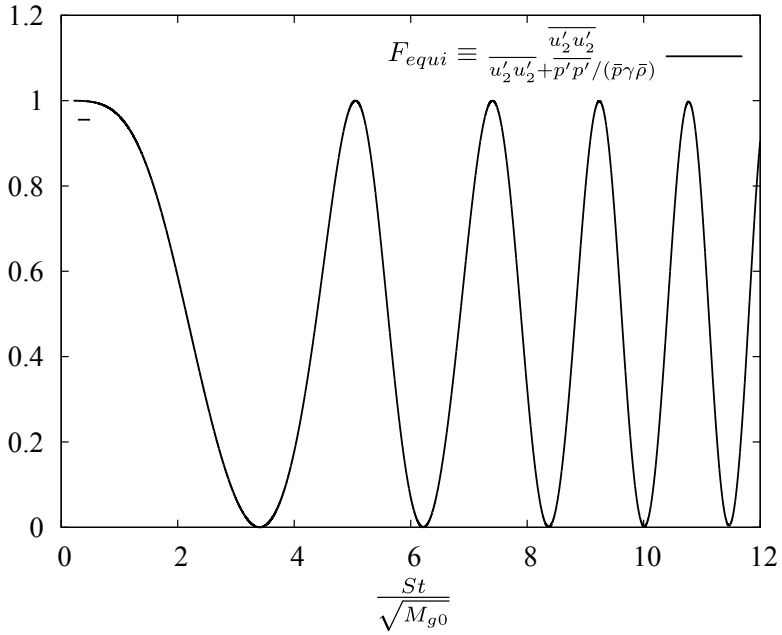

(b)

Fig. 5.6. Evolution of the equi-partition function $F_{equi} = \overline{u_2' u_2'} / \left(\overline{u_2' u_2'} + \overline{p' p'}/(\bar{p}\gamma\bar{\rho}) \right)$: (a) Dilatational mode (mode-1) for an initial modal Mach number $M_{g0} = 5$, (b) Oblique mode with $\vec{\kappa} = (1, 0, 5)$ or $\beta = \tan^{-1}(5)$ for an initial $M_{g0} = 5$.

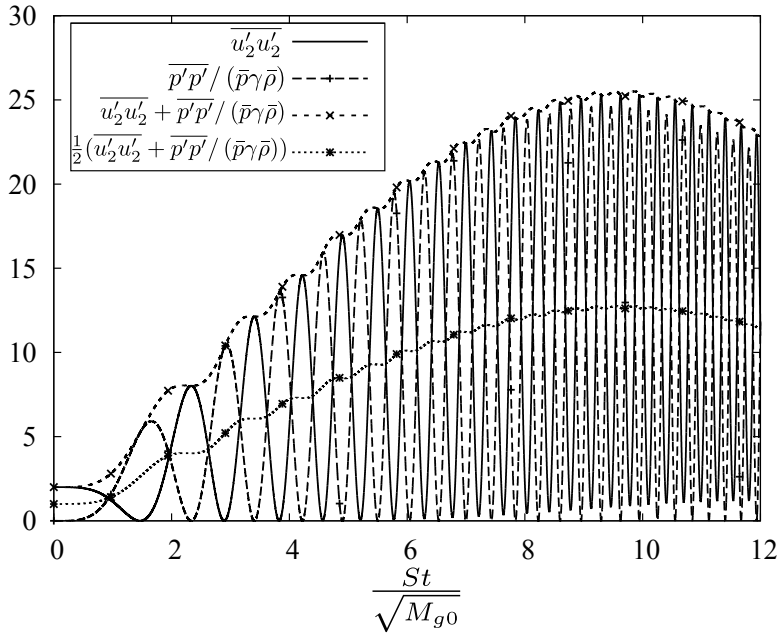

(a)

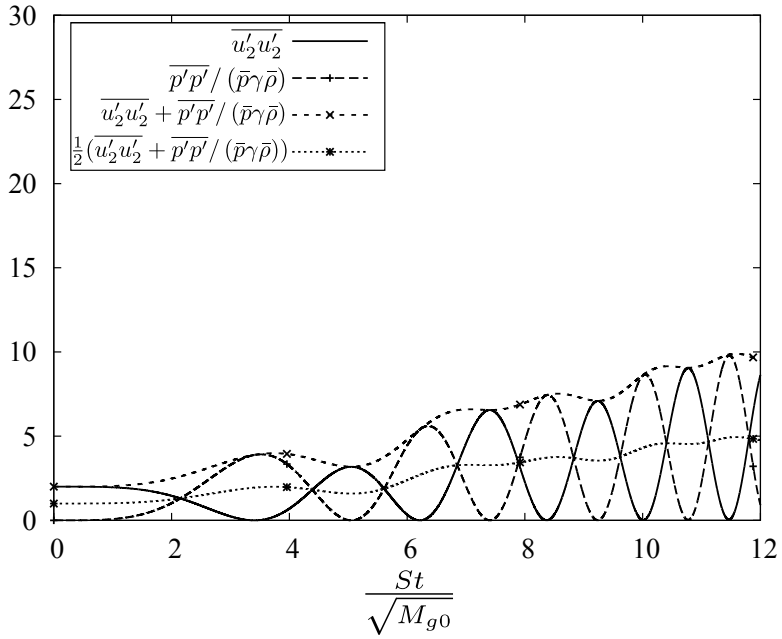

(b)

Fig. 5.7. Evolution of dilatational kinetic energy ($\overline{u_2'u_2'}$) and potential energy of turbulence ($\overline{p'p'}/(\bar{p}\gamma\bar{\rho})$) in DNS of: (a) Dilatational mode (mode-1) for an initial modal Mach number $M_{g0} = 5$, (b) Oblique mode with $\vec{\kappa} = (1, 0, 5)$ or $\beta = \tan^{-1}(5)$ for an initial $M_{g0} = 5$.

5.3.3 Control strategies

In this section we will discuss the effect of change of Prandtl number on collective and modal behavior. Prandtl number (P_r) is defined as

$$P_r = \frac{\mu c_p}{\kappa_t}, \tag{5.-1}$$

where c_p is the specific heat at constant pressure and κ_t is the thermal conductivity. Prandtl number is the ratio of viscous diffusion rate to thermal diffusion rate. A decrease in Prandtl number enhances the transport of internal energy. Transport of internal energy in real flows can be enhanced by processes like endothermic chemical reactions and thermal non-equilibrium. A reduced Prandtl number in a direct numerical simulation mimics the effect of enhanced transport of internal energy and vice versa. An enhanced transport leads to a reduction in mean and fluctuating internal energy. In gases where temperature and pressure are related through a constitutive relation – *the equation of state* – a reduction in temperature fluctuations manifests in an overall reduction in fluctuating pressure. As discussed in section (5.3.2) on the equi-partition of energy, a reduction in $\overline{p'p'}$ is followed by a reduction in dilatational kinetic energy. Equation 5.3.2 shows that u_2' is a good approximation of dilatational component of velocity field in homogeneous shear flows at large shear times. Therefore a reduction in dilatational kinetic energy primarily reduces u_2'. Production of turbulent kinetic energy $P = -S\widetilde{u_1'u_2'}$ (see eq. 5.2.1) is directly dependent on the dilatational component u_2'. A reduction in production leads to a slow-down in the growth of kinetic energy and delays, or in other words controls, the onset of a fully turbulent flow. We will study the effect of change of Prandtl number on collective and modal behavior in the following section.

Collective behavior

We study the effect of Prandtl number on the growth of kinetic energy in homogeneous shear flows. The initial velocity field is random, incompressible, isotropic and satisfies a specified energy spectra $E(\kappa) = A\kappa^4 e^{-B\kappa^2}$. Evolution of kinetic energy in DNS with different Prandtl numbers $P_r = (0.05, 0.1, 0.7, 1.0)$ is shown in Fig. (5.8) for initial gradient Mach numbers $M_{g0} = 10, 15$ and $Re_{\lambda 0} = 15$. As the Prandtl number is reduced from 0.7 to 0.1, the evolution of kinetic energy undergoes the following changes:

1. The growth of kinetic energy in the case with lower Prandtl number shows an early departure from the 'Burgers growth'. The growth of kinetic energy in Burgers turbulence, which is the 'pressure-released limit', is given by $(k/k_0 = 1 + (St)^2/3)$.

2. Growth of kinetic energy in stage-2, which is dominated by acoustic waves, stabilizes at a lower kinetic energy in lower Prandtl number cases.

3. The onset of stage-3 in all Prandtl number cases happens at almost same shear time. Although, a closer look shows that stage-3 begins at slightly later shear time when the Prandtl number is smaller.

4. The growth rate of kinetic energy in stage-3 reduces with a reduction in Prandtl number.

We see that in lower Prandtl number cases a reduction in the level of kinetic energy in stage-2 and a slower growth rate in stage-3 leads to a significantly lower kinetic energy at late shear times. In Fig. (5.9), the evolution of equipartition function F_{equi} is shown for different Prandtl numbers. In all cases, the equipartition function quickly stabilizes at a constant value.

As discussed earlier, a reduction in Prandtl number leads to a reduction in $\overline{p'p'}$ due to an increased transport of fluctuating internal energy which is shown in Fig.

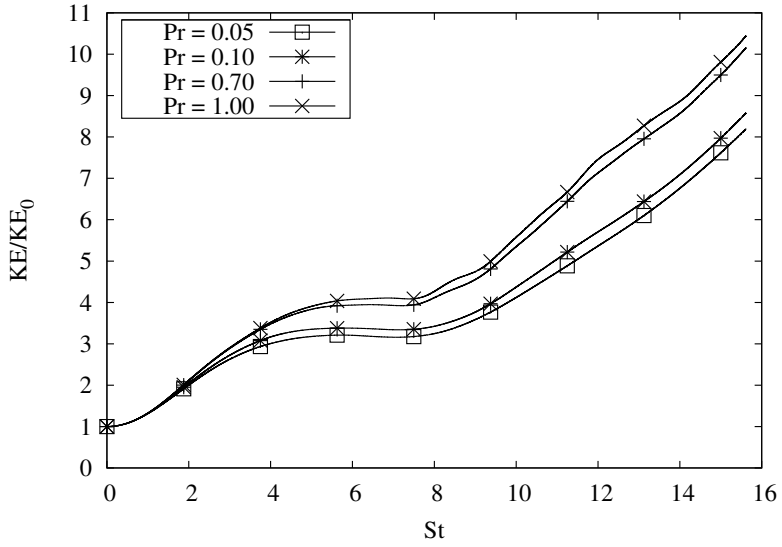

(a)

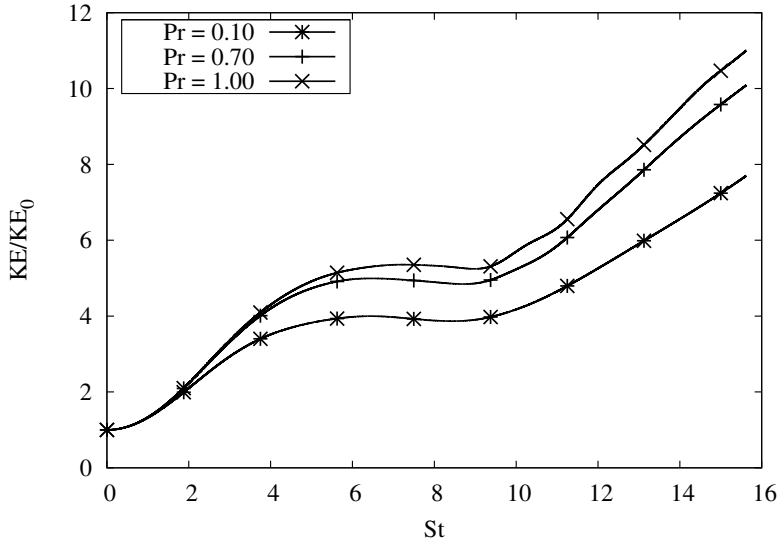

(b)

Fig. 5.8. Effect of Prandtl number $P_r = (0.05, 0.1, 0.7, 1.0)$ on the evolution of kinetic energy in homogeneous shear flows: (a) $M_{g0} = 10, Re_{\lambda 0} = 15$, (b) $M_{g0} = 15, Re_{\lambda 0} = 15$.

5.10(b). In stage-1 ($St < 4$) $\overline{p'p'}$ is higher in lower Prandtl numbers which is attributed to the timescale of the energy equation. At initial times (stage-1) the flow-timescale is much higher compared to the acoustic-timescale which forces the energy equation to be driven by inertia. This leads to a large increase in temperature fluctuations in cases where conductivity (κ_t) is larger or equivalently P_r is smaller. As the acoustic time-scale becomes comparable to the flow timescale in stage-2 the the transport terms in energy equation become increasingly important and destroy (diffuse) the fluctuations in temperature. This leads to a faster decay of $\overline{p'p'}$ in stage-2 and 3 in cases with lower Prandtl number. The reduction in $\overline{p'p'}$ is followed by a simultaneous reduction in $\overline{u_2'u_2'}$ as shown in Fig. 5.10(a). A simultaneous reduction in $\overline{u_2'u_2'}$ and $\overline{p'p'}$ is due to the action of pressure-dilatation which exchanges energy between the internal and kinetic modes. The exchange of energy begins only when the timescale of acoustics becomes comparable to that of flow.

Modal behavior

In this section we study the effect of Prandtl number on the growth of individual modes. We aim to provide a modal based explanation for the observed effect of Prandtl number on the collective behavior. We investigate modes with direction of propagation in the plane normal to the direction of shear. In the previous chapter we have shown that kinetic energy grows for only those modes whose wave-vectors are oriented close to the shear-normal plane. These modes are majority contributors towards the overall growth of kinetic energy.

We investigate kinetic energy, $\overline{u_2'u_2'}$ and $\overline{p'p'}$ of modes with different β. Streamwise modes which have the largest dilatational content show the largest effect of Prandtl number as shown in Figs. 5.11 and 5.12. These modes show an early departure from the Burgers growth and large reduction in kinetic energy in stage-2 and stage-3. A large reduction in $\overline{p'p'}$ for the dilatational modes leads to a large decay in growth of dilatational kinetic energy $\overline{u_2'u_2'}$.

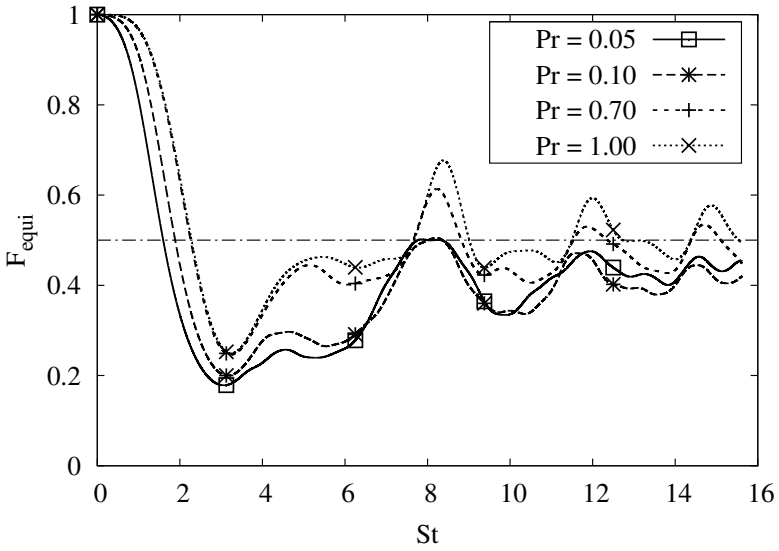

(a)

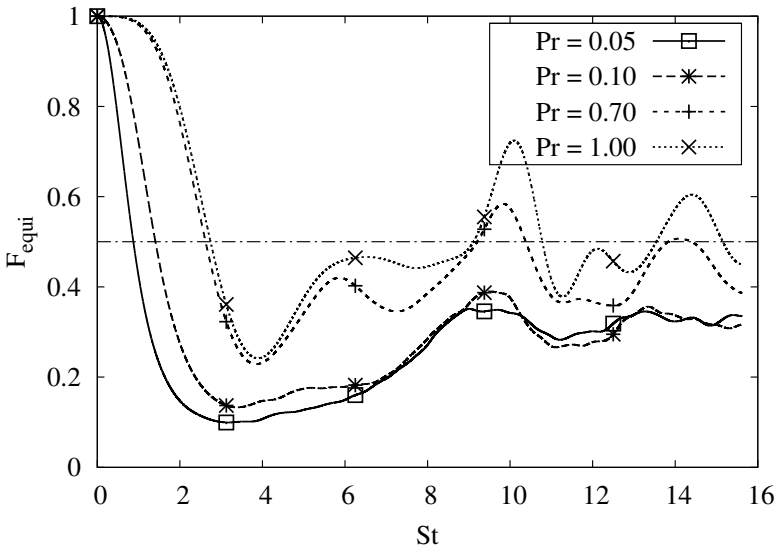

(b)

Fig. 5.9. Evolution of equipartition function F_{equi} for different Prandtl number cases ($P_r = 0.05, 0.1, 0.7, 1.0$): (a) $M_{g0} = 10, Re_{\lambda 0} = 15$, (b) $M_{g0} = 15, Re_{\lambda 0} = 15$.

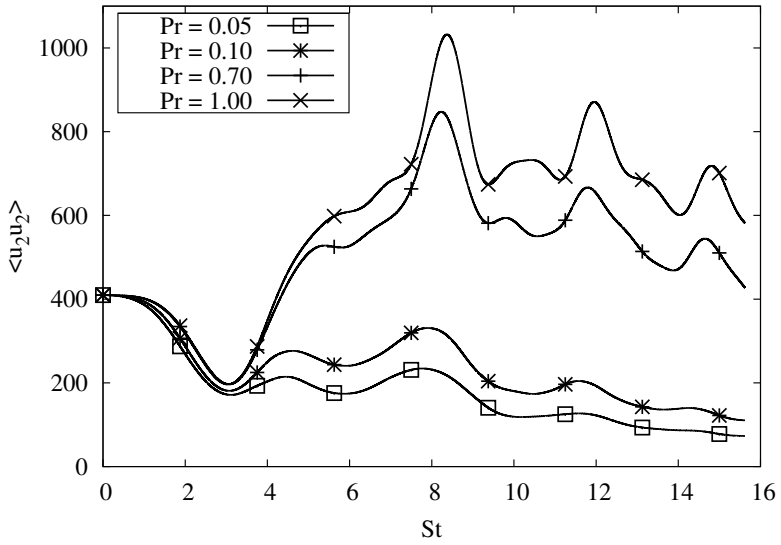

(a)

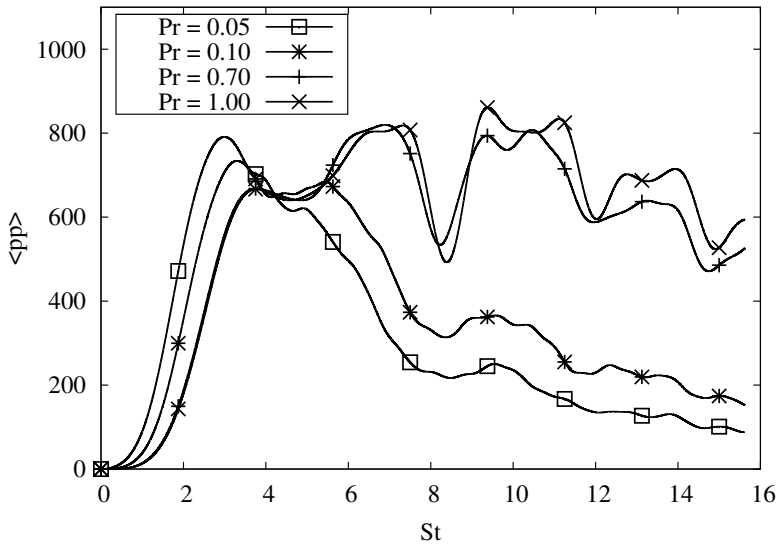

(b)

Fig. 5.10. Evolution in homogeneous shear flow with $M_{g0} = 10, Re_{\lambda 0} = 15$ for different Prandtl numbers ($P_r = 0.05, 0.1, 0.7, 1.0$): (a) $\overline{u_2' u_2'}$, (b) $\overline{p'p'}$.

As the angle β is increased for oblique modes, the beginning of reduction in kinetic energy (compared to a higher Pr case) is observed at increasingly higher shear times. For modes with $\beta > \pi/4$ the decrease in kinetic energy happens only in stage-3 as seen in Fig. 5.14 and 5.15. For purely solenoidal wave, no reduction in kinetic energy is observed. A similar behavior is observed for $\overline{p'p'}$ and $\overline{u_2'u_2'}$ in Figs. 5.13, 5.14 and 5.15 wherein increasing β reduces the effect of Prandtl number or the effect of enhanced transport of internal energy.

Here, we will revisit the definition of effective gradient Mach number M_{g0}^* as defined in Eq. 4.3.1.

$$M_{g0}^* = M_{g0}\cos\beta \propto \frac{1}{\beta}, \frac{1}{\kappa}. \tag{5.-1}$$

For a fixed β direction, the effective gradient Mach number M_{g0}^* seen by an oblique wave decreases with increasing wave-number κ. For a fixed κ, M_{g0}^* decreases with increasing β. The growth of modes with large M_{g0}^* (small β, κ) show a larger and earlier effect of Pr. Compared to a corresponding growth in higher Pr case, higher M_{g0}^* undergo a larger decrease in kinetic energy, $\overline{u_2'u_2'}$ and $\overline{p'p'}$ while those with smaller M_{g0}^* show an effect of changed Pr only at late times. Therefore, M_{g0}^* is the correct parameter to characterize the effect of increased transport on different modes.

5.4 Conclusions

We perform DNS for studying the modal and collective behavior of growth of fluctuations in homogeneous shear flows subject to different Prandtl numbers. We aim to demonstrate a proof-of-concept of thermodynamics-acoustics based strategies for controlling the growth of turbulence in high speed compressible shear flows. We show that the equipartition of energy between the potential energy of turbulence and dilatational kinetic energy can be exploited for design of novel acoustic based flow control strategies.

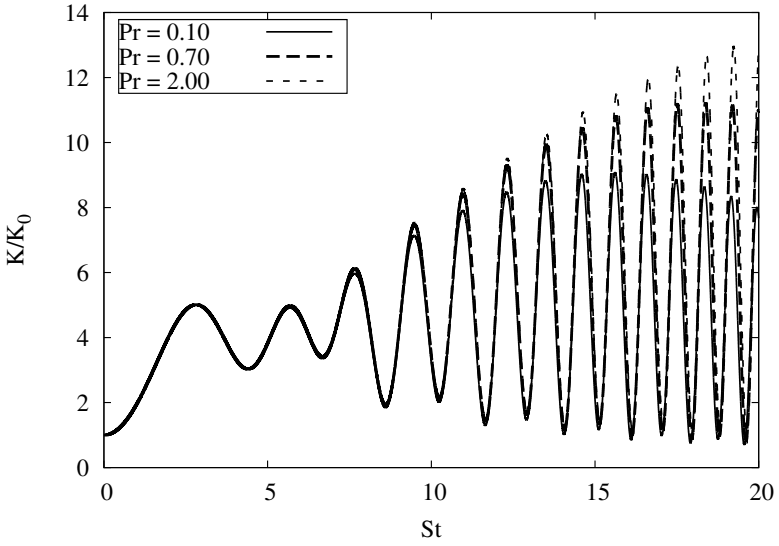

Fig. 5.11. Evolution of kinetic energy for purely dilatational mode ($\vec{\kappa} = (1, 0, 0)$) in homogeneous shear flow with $M_{g0} = 5.0$ and $Re_{\lambda 0} = 15$ for different Prandtl numbers $P_r = (0.1, 0.7, 2.0)$.

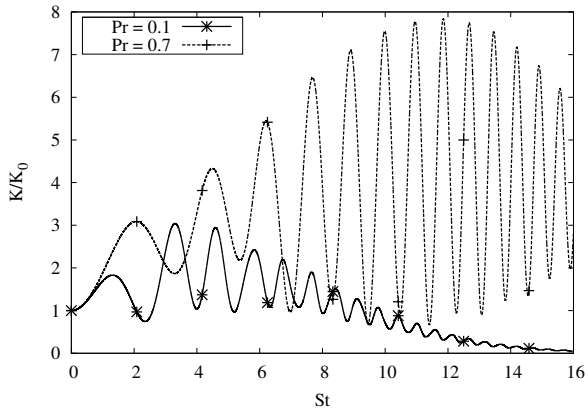

(a)

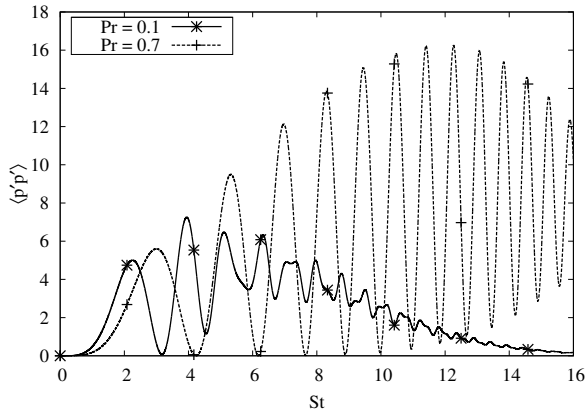

(b)

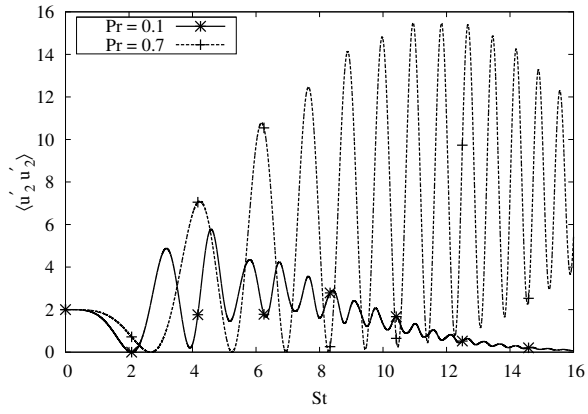

(c)

Fig. 5.12. Evolution of purely dilatational mode ($\vec{\kappa} = (3, 0, 0)$) in homogeneous shear flow with $M_{g0} = 10.0$ and $Re_{\lambda 0} = 15$ for different Prandtl numbers $P_r = (0.1, 0.7)$: (a) kinetic energy, (b) $\overline{p'p'}$, and (c) $\overline{u_2' u_2'}$.

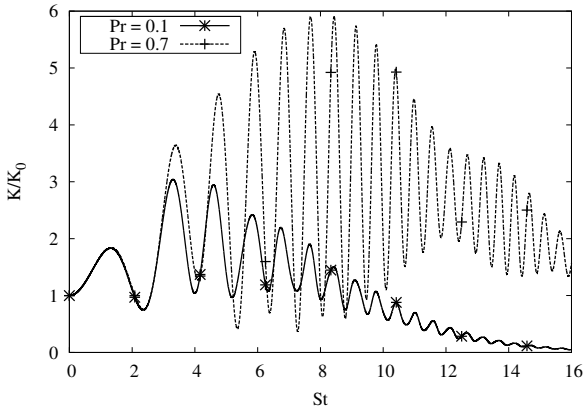

(a)

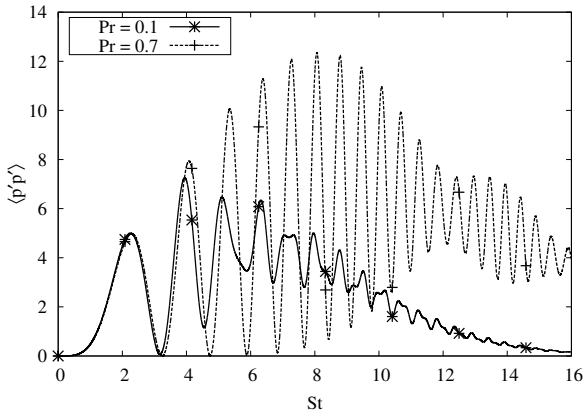

(b)

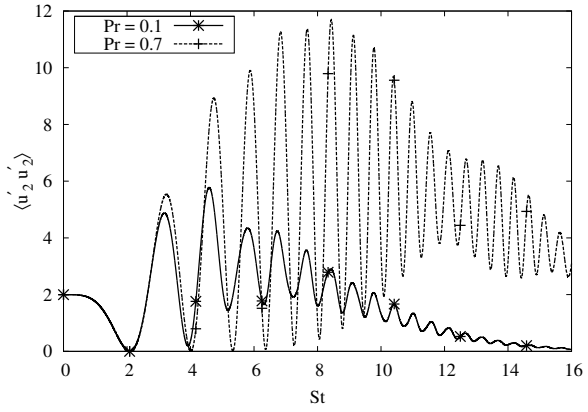

(c)

Fig. 5.13. Evolution of dilatation dominated mode ($\vec{\kappa} = (5, 0, 1)$) in homogeneous shear flow with $M_{g0} = 10.0$ and $Re_{\lambda 0} = 15$ for different Prandtl numbers $P_r = (0.1, 0.7)$: (a) kinetic energy, (b) $\overline{p'p'}$, and (c) $\overline{u_2' u_2'}$.

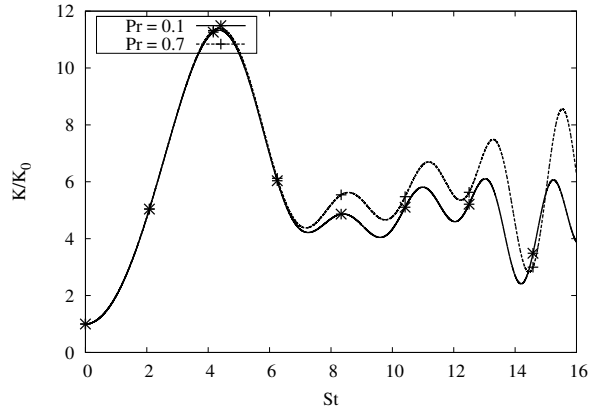

(a)

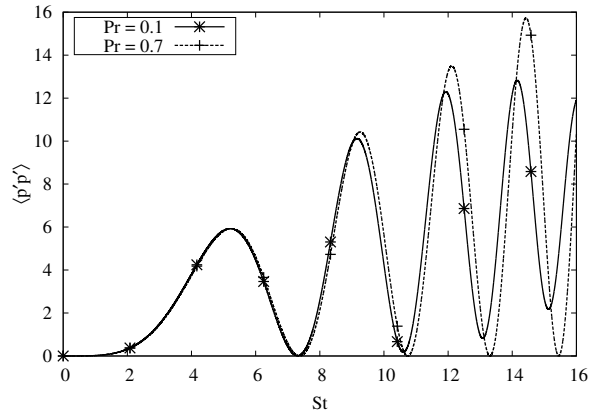

(b)

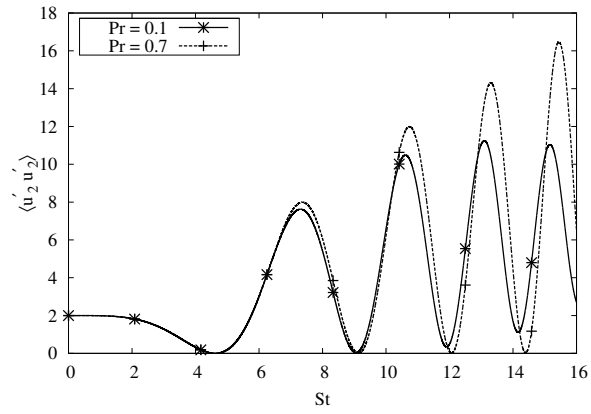

(c)

Fig. 5.14. Evolution of mode with equal solenoidal and dilatational content ($\vec{\kappa} = (1, 0, 1)$) in homogeneous shear flow with $M_{g0} = 10.0$ and $Re_{\lambda 0} = 15$ for different Prandtl numbers $P_r = (0.1, 0.7)$: (a) kinetic energy, (b) $\overline{p'p'}$, and (c) $\overline{u_2'u_2'}$.

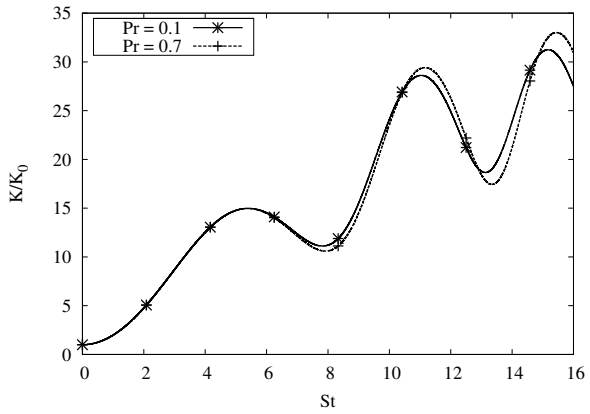

(a)

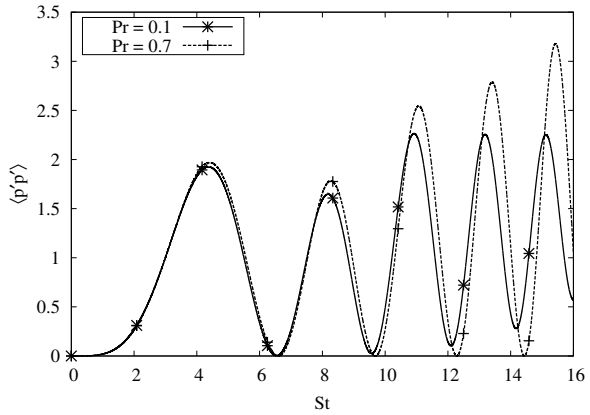

(b)

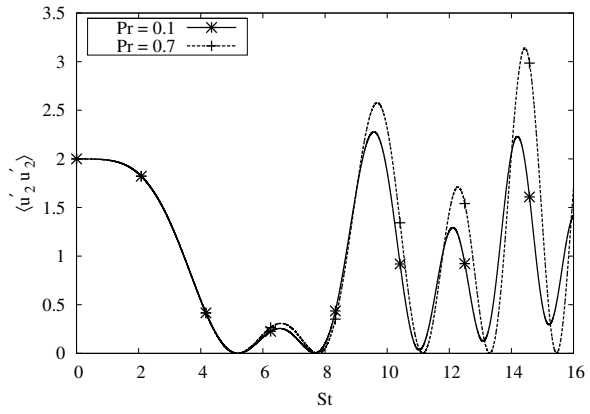

(c)

Fig. 5.15. Evolution of solenoidal dominated mode ($\vec{\kappa} = (1, 0, 5)$) in homogeneous shear flow with $M_{g0} = 10.0$ and $Re_{\lambda 0} = 15$ for different Prandtl numbers $P_r = (0.1, 0.7)$: (a) kinetic energy, (b) $\overline{p'p'}$, and (c) $\overline{u_2' u_2'}$.

In homogeneous shear flows kinetic energy shows a three staged growth characterized by the timescale of acoustics and flow field. We find that in DNS with reduced Prandtl number, kinetic energy: (i) is lower in acoustics dominated stage-2, and (ii) has reduced growth rate in stage-3. From modal analysis we find that the reduction of kinetic energy in stage-2 is primarily due to the dilatational modes. The oblique modes which have a larger dilatational content (smaller β) show a larger decay when the Prandtl number is reduced. The difference between growth of kinetic energy of small and large Prandtl number cases is significant at increasingly early shear times as the dilatational content of the wave increases or, when the effective gradient Mach number M^*_{g0} becomes larger. Since the growth in stage-2 is largely dominated by dilatational/acoustic waves, a reduction in Pr reduces kinetic energy in stage-2 of collective behavior.

Purely solenoidal modes show an insignificant effect of Prandtl number. As the solenoidal content of modes increases (increasing β) reduction in kinetic energy, compared to dilatational modes, is significantly lower. For individual modes having large β (large solenoidal content), the difference between kinetic energy of low and high Pr cases is significant only late shear times. Since growth in stage-3 is dominated by modes with large solenoidal content a slight reduction in growth rate is observed.

5.4.1 Suggestions for future work

In this work we have used a reduction in Prandtl number to mimic the effects of reduction in internal energy due to endothermic chemical reactions, vibrational non-equilibrium etc. A gas with lower vibrational temperature can be injected in the flow field in order to reduce the fluctuating internal energy. For a flow-solver with a single species, a simple scalar equation can be used to model the above physics.

The evolution equation for vibrational energy for a gas in vibrational non-equilibrium [120] is

$$\frac{de_{vib}}{dt} = \frac{1}{\tau}\left(e_{vib}^{eq} - e_{vib}\right). \tag{5.-1}$$

The vibrational relaxation time τ is given by

$$\tau \equiv \frac{1}{k_{1,0}(1 - e^{-h\nu/kT})}, \tag{5.-1}$$

where $k_{1,0}$ is the rate constant for transition from vibrational level 1 to 0 (note: $k_{i,i-1} = ik_{1,0}$), $h = 6.626 \times 10^{-34}$ is the Planck's constant, $k = 1.38 \times 10^{-23}$ is the Boltzmann constant and ν is the vibrational frequency. The equilibrium value for vibrational energy, e_{vib}^{eq}, calculated from the vibrational rate equation (5.4.1) is

$$e_{vib} = e_{vib}^{eq} = \frac{h\nu/kT}{e^{h\nu/kT}} RT. \tag{5.-1}$$

When excited vibrational mode interacts with rotational and translational kinetic energy by exchanging energy such that vibrational and rotational temperatures equilibrate. When the vibrational temperature is less than translational, energy is drained from internal mode which indirectly leads to a reduction in pressure fluctuations. The above physics can be used to exploit the 'equipartition of energy' for late-stage turbulence in homogeneous shear flows and control the onset on turbulence.

6. CONCLUSIONS

In this doctoral dissertation, an enhanced GKM numerical code is first developed and validated. Then the code is used for three important studies. The contributions from different studies are summarized as:

6.1 Contributions from Study 1

A high order accurate and robust numerical tool employing the gas kinetic method and high order interpolation schemes has been developed and evaluated for performing DNS in highly compressible flows.

1. We perform detailed validation studies to determine accuracy and robustness of interpolation schemes in capturing solenoidal statistics, dilatational statistics, linear physics and non-linear physics.

   (a) We observe a key difference between the VL and WENO-based interpolation schemes in capturing solenoidal and dilatational statistics. VL performs as well as WENO-based schemes in capturing the solenoidal statistics. The difference between VL and WENO arises while computing dilatational statistics. The dissipative nature of VL manifests as decreased peaks of statistics strongly related to the dilatational behavior. With increase in M_t the dissipative nature becomes larger and inaccurate. In homogeneous shear case with the 'dilatational' wave, dissipative nature of VL gives rise to under-prediction of turbulent kinetic energy at late 'shear time'.

   (b) We use 512^3 grid as the 'gold standard' simulation for DIT. Capturing shocklets and steep gradients accurately, is key in capturing non-linear physics in DIT. By comparing against the 'gold standard' simulation, we conclude that WENO-based schemes can adequately capture turbulence

statistics in DIT ($M_t = 1.2, Re_\lambda = 46$) with a reasonably coarser 128^3 grid.

2. Though GKM with WENO-based reconstruction is $20 - 30\%$ more computationally expensive than VL, improvement in terms of accuracy and numerical dissipation outweighs the difference in computational time. Amongst the WENO-based schemes, the class of WENO-SYM [65,66] are more accurate and robust than WENO-JS [64]. The symmetric stencil and improved non-linear weights in WENO-SYM are desirable for accuracy in DNS and their robustness is at par with WENO-JS. Typically, dissipative nature increases the robustness of interpolation schemes. For DNS with GKM, we find WENO-based schemes to be more robust than VL despite being significantly less dissipative

3. Despite using highly robust WENO-based schemes, we frequently encounter negative temperature in DIT simulations. We propose interpolating temperature T instead of total-energy E for avoiding negative temperatures. A consistent interpolation of temperature is critical beacuse temperature is used explicitly in the GKM formulation. We also show that the accuracy of the solution is not degraded due to temperature interpolation and is minimal if higher order interpolation is used.

6.2 Contributions from Study 2

In this study we fully characterize the behaviour of pressure in homogeneous shear flows, isolate the unstable modes, explain the linear and non-linear effects and explicate the three-stage growth of kinetic energy using the modal behavior. Investigations in DNS for different modes lead to the following contributions towards understanding the growth of fluctuations in high speed homogeneous shear flow

1. As in incompressible flows, not all Fourier modes grow in the compressible regime. Of the 9 basic modes, only 3 modes grow: Mode 1, 6 and 9. Mode 1

and 6 are initially incompressible and most significant and are referred as the dilatational and solenoidal modes, respectively. Besides basic Fourier modes, oblique modes with varying component of solenoidal and dilatational content grow with growth dependent on the ratio of the solenoidal to dilatational content.

2. Growth of mode-1 increases with an increase in initial gradient Mach number. While fluctuation Mach number has no effect on growth of mode-1 at initial times, it decreases the growth rate at late times due to the larger viscous effect. Mode-1 has large dilatation field and compressible dissipation and negligible solenoidal dissipation and enstrophy.

3. Mode-6 has no effect of initial modal gradient Mach number and fluctuation Mach number. Mode-6 has negligible dilatation and compressible dissipation but large solenoidal dissipation and vorticity.

4. Oblique modes with larger solenoidal content show decrease in kinetic energy with increasing modal gradient Mach number at late shear time. oblique modes with larger dilatational content show an increased growth of kinetic energy with increasing M_{g0}.

5. Kinetic energy of oblique waves with $\beta > \beta_{crit}$ grows and those with $\beta < \beta_{crit}$ decays in time.

6. We see an scaling in kinetic energy and pressure in mixed time $t^* = S^* t/\sqrt{M^*_{g0}}$ or equivalently the local acoustic time.

7. Pressure plays a significant role in evolution of mode-1 while in mode-6 role of pressure is absent. We discuss scaling of frequency of pressure in mode-1 at early and late shear times.

6.3 Contributions from Study 3

In this study we show how the *equi-partition of energy* between the potential energy of turbulence and dilatational kinetic energy can be used for designing flow control strategies in homogeneous shear flows. We show that an enhanced transport of internal energy, simulated through a reduction in Prandtl number, leads to a slow-down in the growth of modes which have a large dilatational content. When the Prandtl number is reduced in modal simulations we find that: (a) as the effective gradient Mach number M^*_{g0} for the individual modes increases, the decrease in kinetic energy is larger and the departure in growth rates begins at increasingly early shear times. As the Prandtl number is reduced, modes with large solenoidal content show much smaller reduction in kinetic energy compared to dilatational waves and the reduction in kinetic energy only becomes significant at late shear times. An effective acoustic based control-strategy in highly shear dominated flows should be aimed at stemming the growth of dilatational waves.

REFERENCES

[1] P. L. Bhatnagar, E. P. Gross, and M. Krook, "A model for collision processes in gases. I. small amplitude processes in charged and neutral one-component systems," *Physical Review*, vol. 94, pp. 511–525, 1954.

[2] K. Xu, "Gas kinetic schemes for unsteady compressible flow simulations," *VKI for Fluid Dynamics Lecture Series*, 1998.

[3] K. Xu and K. H. Prendergast, "Numerical Navier-Stokes Solutions from Gas Kinetic Theory," *Journal of Computational Physics*, vol. 114, no. 1, pp. 9–17, 1994.

[4] H. Risken, *The Fokker-Planck equation: Methods of solution and applications*. Springer Verlag, 1996.

[5] W. Liao, Y. Peng, and L.-S. Luo, "Gas-kinetic schemes for direct numerical simulations of compressible homogeneous turbulence," *Physical Review E*, vol. 80, no. 1, pp. 1–27, 2009.

[6] P. Bradshaw, "Compressible turbulent shear layers," *Annual Review of Fluid Mechanics*, vol. 9, no. 1, pp. 33–52, 1977.

[7] S. J. Kline, B. Cantwell, and Lilley, *Complex turbulent flows: Computation, experiment: The 1980-81 AFOSR-HTTM-Stanford conference on complex turbulent flows, comparison of computation and experiment*. Thermosciences Division, Mechanical Engineering Dept., Stanford University, 1982.

[8] D. Papamoschou and A. Roshko, "The compressible turbulent shear layer: an experimental study," *J. Fluid Mech*, vol. 197, no. 453, 1988.

[9] S. Sarkar, "The stabilizing effect of compressibility in turbulent shear flow," *Journal of Fluid Mechanics*, vol. 282, pp. 163–186, 1995.

[10] A. Simone, G. Coleman, and C. Cambon, "The effect of compressibility on turbulent shear flow: a rapid-distortion-theory and direct-numerical-simulation study," *Journal of Fluid Mechanics*, vol. 330, pp. 307–338, 1997.

[11] R. Bertsch and S. Girimaji, "Pressure effects in compressible flows at the rapid distortion limit," *Bulletin of the American Physical Society*, vol. 54, no. MB.00010, 2009.

[12] S. Suman, H. Yu, S. Girimaji, and T. Lavin, "Rapid distortion analysis of compressible turbulence in ideal gas: Part 2-Density averaged moments," *Bulletin of the American Physical Society*, no. AP.00005, 2006.

[13] T. Lavin, H. Yu, and S. Girimaji, "Rapid distortion analysis of compressible turbulence in ideal gas: Part 1–Reynolds averaged moments," *Bulletin of the American Physical Society*, no. AP.005, 2006.

[14] K. Xu, "A Gas kinetic BGK scheme for the Navier-Stokes equations and its connection with artificial dissipation and Godunov method," *Journal of Computational Physics*, vol. 171, pp. 289–335, 2001.

[15] K. Xu, M. Mao, and L. Tang, "A multidimensional gas-kinetic BGK scheme for hypersonic viscous flow," *Journal of Computational Physics*, vol. 203, no. 2, pp. 405–421, 2005.

[16] Q. Li, S. Fu, and K. Xu, "Application of gas-kinetic scheme with kinetic boundary conditions in hypersonic flow," *AIAA journal*, vol. 43, no. 10, p. 2170, 2005.

[17] T. Lou, D. C. Dahlby, and D. Baganoff, "A numerical study comparing kinetic flux-vector splitting for the Navier-Stokes equations with a particle method," *Journal of Computational Physics*, vol. 145, no. 2, pp. 489–510, 1998.

[18] K. Xu, L. Martinelli, and A. Jameson, "Gas-kinetic finite volume methods, flux-vector splitting, and artificial diffusion," *Journal of Computational Physics*, vol. 120, pp. 48–65, 1995.

[19] K. Xu, "Gas-kinetic theory based flux splitting method for ideal magnetohydrodynamics," *ICASE, Report No. 98-53*, 1998.

[20] K. Xu, "A gas-kinetic bgk scheme for the compressible Navier-Stokes equations," *ICASE, Report No. 2000-38*, 2000.

[21] G. May, B. Srinivasan, and A. Jameson, "An improved gas-kinetic BGK finite-volume method for three-dimensional transonic flow," *Journal of Computational Physics*, vol. 220, pp. 856–878, 2007.

[22] H. Yu, S. S. Girimaji, and L.-S. Luo, "DNS and LES of decaying isotropic turbulence with and without frame rotation using lattice Boltzmann method," *Journal of Computational Physics*, vol. 209, no. 2, pp. 599–616, 2005.

[23] Y. Peng, W. Liao, L.-S. Luo, and L.-P. Wang, "Comparison of the lattice Boltzmann and pseudo-spectral methods for decaying turbulence: Low-order statistics," *Computers & Fluids*, vol. 39, no. 4, pp. 568–591, 2010.

[24] J. Quirk, "A contribution to the great Riemann solver debate," *Int. J. Num. Met. in Fluids*, vol. 18, no. 6, pp. 555–574, 1994.

[25] J. Gressier and J. M. Moschetta, "On the pathological behavior of upwind schemes," *American Institute of Aeronautics and Astronautics*, vol. AA 98-0110, 1998.

[26] D. Chae, C. Kim, and O.-H. Rho, "Development of an improved gas-kinetic bgk scheme for inviscid and viscous flows," *Journal of Computational Physics*, vol. 158, pp. 1–27, 2000.

[27] K. Xu, "Gas evolution dynamics in Godunov-type schemes," *Lecture notes*, pp. –.

[28] W. G. Vincenti and C. H. Kruger, *Introduction to physical gas dynamics*. Cambridge university press, Krieger Pub. Co., 1975.

[29] K. M. Peery and S. T. Imlay, "Blunt body flow simulations," *AIAA*, pp. 88–2924, 1988.

[30] J.-C. Robinet, J. Gressier, G. Casalis, and J.-M. Moschetta, "Shock wave instability and the carbuncle phenomenon: same intrinsic origin?," *Journal of Fluid Mechanics*, vol. 417, pp. 237–263, 2000.

[31] K. Xu and J. Hu, "Projection dynamics in godunov-typeschemes," *Journal of Computational Physics*, vol. 142, no. 2, pp. 412–427, 1998.

[32] S. N. Abdusslam, O. J. Chit, M. M. Hamdan, A. A. Omar, and W. Asrar, "Application of gas-kinetic bgk scheme for solving 2-d compressible inviscid flow around linear turbine cascade," *International Journal for Computational Methods in Engineering Science and Mechanics*, vol. 7, pp. 403–410, 2006.

[33] S. Jain, "Hypersonic non-equilibrium flow simulation over a blunt body using bgk method," *Texas A&M University*, 2007.

[34] R. Sanders, E. Morano, and M. Druguet, "Multidimensional dissipation for upwind schemes: stability and applications to gas dynamics," *Journal of Computational Physics*, vol. 145, no. 2, pp. 511–537, 1998.

[35] P. Dechaumphai and S. Phongthanapanich, "High-speed compressible flow solutions by adaptive cell-centered upwinding algorithm with modified H-correction entropy fix," *Advances in Engineering Software*, vol. 34, no. 9, pp. 533–538, 2003.

[36] K. Xu and E. Josyula, "Gas-kinetic scheme for rarefied flow simulation," *Mathematics and Computers in Simulation*, vol. 72, pp. 253–256, 2006.

[37] Q. Li, K. Xu, and S. Fu, "A high-order gas-kinetic Navier-Stokes flow solver," *Journal of Computational Physics*, vol. 229, pp. 6715–6731, 2010.

[38] K. Xu and J.-C. Huang, "A unified gas-kinetic scheme for continuum and rarefied flows," *Journal of Computational Physics*, vol. 229, pp. 7747–7764, 2010.

[39] J.-C. Huang, K. Xu, and P. Yu, "A unified gas-kinetic Scheme for continuum and rarefied flows II: Multi-dimensional cases," *Commun. Comput. Phys.*, vol. 12, no. 3, pp. 662–690, 2012.

[40] J.-C. Huang, K. Xu, and P. Yu, "A unified gas-kinetic scheme for continuum and rarefied flows III: Microflow simulations," *Journal of Computational Physics*, vol. Preprint, 2012.

[41] S. Chen, K. Xu, C. Li, and Q. Cai, "A unified gas-kinetic scheme with moving mesh and velocity space adaptation," *Journal of Computational Physics*, vol. Preprint, 2012.

[42] B. Enfield, C. D. Munz, P. L. Roe, and B. Sjogreen, "On godunov type methods near low density," *Journal of Computational Physics*, vol. 92, pp. 273–295, 1991.

[43] G. Totha and D. Odstrcil, "Comparison of some flux corrected transport and total variation diminishing numerical schemes for hydrodynamic and magnetohydrodynamic problems," *Journal of Computational Physics*, vol. 128, no. 1, pp. 82–100, 1996.

[44] Y. Ruan and A. Jameson, "Gas Kinetic BGK Method for three-dimensional compressible flows," *American Institute of Aeronautics and Astronautics*, pp. AIAA–2002–0550, 2002.

[45] J. L. Estivalezes and P. Villedieu, "High-order positivity preserving kinetic schemes for the compressible Euler equations," *SIAM J. Numer. Anal.*, vol. 33, 1996.

[46] D. I. Pullin, "Direct simulations methods for compressible inviscid ideal gas flows," *Journal of Computational Physics*, vol. 34, 1980.

[47] Z.-H. Li and H.-X. Zhang, "Study on gas kinetic unified algorithm for flows from rarefied transition to continuum," *Journal of Computational Physics*, vol. 193, pp. 708–738, 2004.

[48] M. Su, K. Xu, and M. S. Ghidaoui, "Low-speed flow simulation by the gas-kinetic scheme," *Journal of Computational Physics*, vol. 150, pp. 17–39, 1999.

[49] P. M. Gresho, "On the theory of semi-implicit projection methods for viscous incompressible flow and its implementation via finite element method that also introduces a nearly consistent mass matrix. Part 1: Theory; Part 2: Implementation," *Int. J. Num. Methods Fluids*, vol. 11, no. 5, pp. 621–659, 1990.

[50] N. M. Kogan, *Rarefied gas dynamics*. New York: Plenum Press, 1969.

[51] S. Harris, *An introduction to the theory of Boltzmann equations*. New York: Dover Publications, 2004.

[52] E. Oran, C. Oh, and B. Cybyk, "Direct simulation Monte Carlo: Recent advances and application," *Annual Review of Fluid Mechanics*, vol. 30, pp. 403–441, 1999.

[53] G. Bird, *Molecular gas dynamics and the direct simulation of gas flows*. Oxford University Press, Oxford University Press, 2nd ed., 1994.

[54] H. Chen, S. Chen, and W. H. Matthaeus, "Recovery of the Navier-Stokes equations using a lattice-gas Boltzmann method," *Phys. Rev. A*, vol. 45, pp. R5339–R5342, Apr 1992.

[55] Z. Guo, H. Liu, L.-S. Luo, and K. Xu, "A comparative study of the LBE and GKS methods for 2D near incompressible laminar flows," *Journal of Computational Physics*, vol. 227, no. 10, pp. 4955–4976, 2008.

[56] J. Kerimo and S. S. Girimaji, "Boltzmann-BGK approach to simulating weakly compressible 3D turbulence: comparison between lattice Boltzmann and gas kinetic methods," *Journal of Turbulence*, vol. 8, no. 46, pp. 1–16, 2007.

[57] H. Yu, S. S. Girimaji, and L.-S. Luo, "Lattice Boltzmann simulations of decaying homogeneous isotropic turbulence," *Physical Review E*, vol. 71, no. 1, pp. 016708–016713, 2005.

[58] He, Xiaoyi, and L.-S. Luo, "Theory of the lattice Boltzmann method: From the Boltzmann equation to the lattice Boltzmann equation," *Phys. Rev. E*, vol. 56, pp. 6811–6817, Dec 1997.

[59] K. Xu, K. Martinelli, and A. L. Jameson, "Gas-kinetic finite volume methods, flux-vector splitting, and artificial diffusion," *Journal of computational physics*, vol. 120, no. 1, pp. 48–65, 1995.

[60] T. Ohwada and K. Xu, "The kinetic scheme for the full-burnett equations," *Journal of computational physics*, vol. 201, pp. 315–332, Nov 2004.

[61] R. Agarwal, K. Yun, and R. Balakrishnan, "Beyond the Navier–Stokes: Burnett equations for flows in the continuum-transition regime," *Physics of Fluids*, vol. 13, pp. 3061–3085, Oct 2001.

[62] K. Xu and Z. Li, "Microchannel flow in the slip regime: gas-kinetic BGK-Burnett solution," *Journal of Fluid Mechanics*, vol. 513, p. 87–110, 2004.

[63] S. Chen and G. D. Doolen, "Lattice boltzmann method for fluid flows," *Annual Review of Fluid Mechanics*, vol. 30, pp. 329–364, Jan 1999.

[64] G.-S. Jiang and C.-W. Shu, "Efficient implementation of weighted ENO schemes," *Journal of Computational Physics*, vol. 126, no. 1, pp. 202–228, 1996.

[65] M. Martín, E. Taylor, M. Wu, and V. Weirs, "A bandwidth-optimized WENO scheme for the effective direct numerical simulation of compressible turbulence," *Journal of Computational Physics*, vol. 220, no. 1, pp. 270–289, 2006.

[66] E. M. Taylor, M. Wu, and M. P. Martín, "Optimization of nonlinear error for weighted essentially non-oscillatory methods in direct numerical simulations of compressible turbulence," *Journal of Computational Physics*, vol. 223, no. 1, pp. 384–397, 2007.

[67] B. van Leer, "Towards the ultimate conservative difference scheme. II. Monotonicity and conservation combined in a second-order scheme," *Journal of Computational Physics*, vol. 14, pp. 361–370, 1974.

[68] B. van Leer, "Towards the ultimate conservative difference scheme III. Upstream-centered finite-difference schemes for ideal compressible flow," *Journal of Computational Physics*, vol. 23, pp. 263–275, 1977.

[69] B. van Leer, "Towards the ultimate conservative difference scheme. iv. a new approach to numerical convection," *Journal of Computational Physics*, vol. 23, pp. 276–299, 1977.

[70] B. van Leer, "Towards the ultimate conservative difference scheme. V. A second-order sequel to Godunov's method," *Journal of Computational Physics*, vol. 32, pp. 101–136, 1979.

[71] X.-D. Liu, S. Osher, and T. Chan, "Weighted essentially non-oscillatory schemes," *Journal of Computational Physics*, vol. 115, no. 1, pp. 200–212, 1994.

[72] A. Harten and S. Osher *SIAM J. Numer. Anal.*, vol. 24, p. 279, 1971. MRC Technical Summary Report No. 2823, May 1985 (unpublished).

[73] A. Harten, B. Engquist, S. Osher, and S. R. Chakravarthy, "Uniformly high order accurate essentially non-oscillatory schemes, III," *Journal of Computational Physics*, vol. 71, no. 2, pp. 231–303, 1987.

[74] A. Harten, B. Engquist, S. Osher, and S. R. Chakravarthy, "Uniformly high order accurate essentially non-oscillatory schemes, III," *Journal of Computational Physics*, vol. 131, no. 1, pp. 3–47, 1997.

[75] R. Samtaney, D. I. Pullin, and B. Kosovic, "Direct numerical simulation of decaying compressible turbulence and shocklet statistics," *Physics of Fluids*, vol. 13, pp. 1415–1430, May 2001.

[76] G. K. Batchelor and I. Proudman, "The effect of rapid distortion of a fluid in turbulent motion," *The Quarterly Journal of Mechanics and Applied Mathematics*, vol. 7, no. 1, p. 83, 1954.

[77] G. A. Blaisdell, G. N. Coleman, and N. Mansour, "Rapid distortion theory for compressible homogenous turbulence under isotropic mean strain," *Physics of Fluids*, vol. 8, no. 10, pp. 2692–2705, 1996.

[78] T. Lavin, *Reynolds and Favre-averaged rapid distortion theory for compressible, ideal-gas turbulence*. PhD thesis, Texas A&M University, 2007.

[79] A. Favre, "The equations of compressible turbulent gases," 1965.

[80] A. Favre, "Statistical equations of turbulent gases," *Problems of hydrodynamics and continuum mechanics: contributions in honor of the sixtieth birthday of Academician LI Sedov, 14th November 1967*, p. 231, 1969.

[81] T. A. Lavin, S. S. Girimaji, S. Suman, and H. Yu, "Flow-thermodynamics interactions in rapidly-sheared compressible turbulence," *Theoretical and Computational Fluid Dynamics*, pp. 1–22, 2011.

[82] F. Baron, *Macro-simulation tridimensionelle d'ecoulements turbulents cisailles*. PhD thesis, Universite Pierre at Marie Curie, Paris, 1982.

[83] U. Schumann, "Algorithms for direct numerical simulation of shear-periodic turbulence." Lecture notes in physics, 1985.

[84] T. Gerz, U. Schumann, and S. Elghobashi, "Direct numerical simulation of stratified homogenous turbulent shear flows," *Journal of Fluid Mechanics*, vol. 200, pp. 563–594, 1989.

[85] J. Kreuzinger and R. Friedrich, "DNS of homogeneous shear flow and data analysis for the development of a four-equation turbulence model," *High performance computing in science and engineering*, pp. 59–69, 2002.

[86] S. B. Pope, *Turbulent Flows*. Cambridge university press, Cambridge University Press, 1st ed., 2006.

[87] S. Sarkar, G. Erlebacher, M. Hussaini, , and H. Kreiss, "The analysis and modeling of dilatational terms in compressible turbulence," *Journal of Fluid Mechanics*, vol. 227, pp. 473–493, 1991.

[88] K. Lee, *Heat release effects on decaying homogeneous compressible turbulence*. PhD thesis, Texas A&M University, College Station, TX, May 2008.

[89] D. Papamoschou and A. Roshko, "The compressible turbulent shear layer: An experimental study," *Journal of Fluid Mechanics*, vol. 197, pp. 453–477, 1988.

[90] N. T. Clemens and M. G. Mungal, "Large-scale structure and entrainment in the supersonic mixing layer," *Journal of Fluid Mechanics*, vol. 284, pp. 171–216, 1995.

[91] J. L. Hall, P. E. Dimotakis, and H. Rosemann, "Experiments in nonreacting compressible shear layers," *AIAA Journal*, vol. 31, no. 12, pp. 2247–2254, 1993.

[92] N. Chinzei, G. Masuya, T. Komuro, A. Murakami, and K. Kudou, "Spreading of two-stream supersonic turbulent mixing layers," *Physics of Fluids*, vol. 29, no. 5, pp. 1345–1347, 1986.

[93] M. Samimy and G. S. Elliot, "Effects of compressibility on the characteristics of free shear layers," *AIAA Journal*, vol. 28, no. 3, pp. 439–445, 1990.

[94] S. G. Goebel and J. C. Dutton, "Experimental study of compressible turbulent mixing layers," *AIAA Journal*, vol. 29, no. 4, pp. 538–546, 1991.

[95] T. Lavin, S. Girimaji, S. Suman, and H. Yu, "Flow-thermodynamics interactions in rapidly-sheared compressible turbulence," *Theoretical and Computational Fluid Dynamics*, pp. 1–22, 2011.

[96] J. Sivasubramanian and H. F. Fasel, "Numerical investigation of laminar-turbulent transition in a cone boundary layer at Mach 6," *41st AIAA Fluid Dynamics Conference and Exhibit*, pp. 1–24, 2011.

[97] C. Hader and H. F. Fasel, "Numerical investigation of porous walls for a Mach 6.0 boundary layer using an immersed boundary method," *41st AIAA Fluid Dynamics Conference and Exhibit*, pp. 1–24, 2011.

[98] J. Sivasubramanian and H. F. Fasel, "Transition initiated by a localized disturbance in a hypersonic flat-plate boundary layer," *49th AIAA Aerospace Sciences Meeting*, pp. 1–24, 2011.

[99] J. Sivasubramanian and H. F. Fasel, "Direct numerical simulation of a turbulent spot in a cone boundary layer at Mach 6," *40th Fluid Dynamics Conference and Exhibit*, pp. 1–26, 2010.

[100] R. L. Bertsch, "Rapidly sheared compressible turbulence: characterization of different pressure regimes and effect of thermodynamic fluctuations," Master's thesis, Texas A&M University, College Station, TX, 2010.

[101] R. L. Bertsch, S. Suman, and S. S. Girimaji, "Rapid distortion analysis of high Mach number homogeneous shear flows: characterization of flow-thermodynamic interaction regimes.".

[102] A. Mishra and S. Girimaji, "Pressure–strain correlation modeling: Towards achieving consistency with rapid distortion theory," *Flow, turbulence and combustion*, pp. 1–27, 2010.

[103] A. Mishra and S. Girimaji, "A pressure-strain correlation closure model with improved consistency with the rapid distortion theory of turbulence," *Bulletin of the American Physical Society*, vol. 55, no. CC.00002, 2010.

[104] S. Pope, *Turbulent flows*. Cambridge Univ Pr, 2000.

[105] G. Kumar, S. S. Girimaji, and J. Kerimo, "WENO-enhanced gas-kinetic scheme for direct simulations of compressible transition and turbulence," *Journal of Computational Physics*, vol. to be published, 2012.

[106] R. Rogallo, *Numerical experiments in homogeneous turbulence*, vol. 81315. National Aeronautics and Space Administration, 1981.

[107] R. Rogallo, "Numerical experiments in homogeneous turbulence," Tech. Rep. 81315, 1981.

[108] L. Kovasznay, "Turbulence in supersonic flow," *J. Aero. Sci.*, vol. 20, pp. 657–682, 1953.

[109] D. Livescu and C. Madnia, "Small scale structure of homogeneous turbulent shear flow," *Physics of Fluids*, vol. 16, p. 2864, 2004.

[110] A. Clark, *Elements of abstract algebra*. Dover Pubns, 1984.

[111] D. M. Bushnell and M. C. B., "Turbulence control in wall flows," *Annual Review of Fluid Mechanics*, vol. 21, pp. 1–20, 1989.

[112] D. M. Bushnell and K. J. Moore, "Drag reduction in nature," *Annual Review of Fluid Mechanics*, vol. 23, pp. 65–79, 1991.

[113] P. R. Bandyopadhyay, "Review–Mean flow in turbulent boundary layers disturbed to alter skin friction," *Journal of Fluids Engineering*, vol. 108, pp. 127–140, 1986.

[114] H. Fiedler and H. Fernholz, "On management and control of turbulent shear flows," *Prog Aerospace Sci*, vol. 27, pp. 305–387, 1990.

[115] H. Choi, P. Moin, and J. Kim, "Direct numerical simulation of turbulent flow over riblets," *Journal of Fluid Mechanics*, vol. 255, pp. 503–539, 1993.

[116] J. J. Riley, M. Gad-el Hak, and R. W. Metcalfe, "Compliant coatings," *Annual Review of Fluid Mechanics*, vol. 20, pp. 393–420, 1988.

[117] G. Blaisdell, G. Coleman, and N. Mansour, "Rapid distortion theory for compressible homogenous turbulence under isotropic mean strain," *Physics of Fluids*, vol. 8, no. 10, pp. 2692–2705, 1996.

[118] S. Sarkar, G. Erlebacher, and M. Hussaini, "Direct simulation of compressible turbulence in a shear flow," *Theoretical and Computational Fluid Dynamics*, vol. 2, no. 5, pp. 291–305, 1991.

[119] S. Sarkar, G. Erlebacher, M. Hussaini, and H. Kreiss, "The analysis and modelling of dilatational terms in compressible turbulence," *Journal of Fluid Mechanics*, vol. 227, no. 1, pp. 473–493, 1991.

[120] J. D. Anderson, *Hypersonic and High Temperature Gas Dynamics*. American Institute of Aeronautics and Astronautics, 2000.